

2006

Fracture surface analysis of Ni-20wt%Cr using high resolution microscopy

Srivalli Bose Abburi
University of Dayton

Follow this and additional works at: https://ecommons.udayton.edu/graduate_theses

Recommended Citation

Abburi, Srivalli Bose, "Fracture surface analysis of Ni-20wt%Cr using high resolution microscopy" (2006).
Graduate Theses and Dissertations. 6.
https://ecommons.udayton.edu/graduate_theses/6

This Thesis is brought to you for free and open access by the Theses and Dissertations at eCommons. It has been accepted for inclusion in Graduate Theses and Dissertations by an authorized administrator of eCommons. For more information, please contact mschlange1@udayton.edu, ecommons@udayton.edu.

**FRACTURE SURFACE ANALYSIS OF Ni-20wt. %Cr USING HIGH
RESOLUTION MICROSCOPY**

Thesis

Submitted to

The School of Engineering

UNIVERSITY OF DAYTON

In Partial Fulfillment of the Requirements for

The Degree

Master of Science in Materials Engineering

by

Srivalli Bose Abburi

THE UNIVERSITY OF DAYTON

DAYTON, OHIO

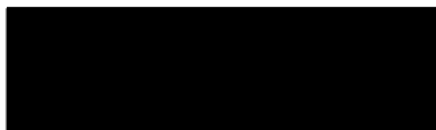
MAY 2006

Fracture Surface Analysis of Ni-20wt%Cr using High Resolution Microscopy

APPROVED BY:



Shamachary Sathish, Ph. D.
Advisory Committee Chairman
Professor, Graduate Materials Engineering



Daniel Eylon, D.Sc
Committee Member
Director, Graduate Materials Engineering



Michael Gigliotti, Ph.D.
Committee Member
Metallurgist
GE Global Research



Donald L. Moon, Ph.D.
Associate Dean
Graduate Engineering Programs &
Research
School of Engineering



Joseph Saliba, Ph.D., P.E.
Dean, School of Engineering

ABSTRACT

FRACTURE SURFACE ANALYSIS OF Ni-20wt.%Cr USING HIGH RESOLUTION MICROSCOPY

Abhuri, Srivalli Bose
University of Dayton 2006

Advisor: Dr.Shamachary Sathish

This thesis presents the results of surface analysis of fatigue fractured samples of Ni-20wt.%Cr. The average grain sizes in the samples vary from nano-meters to several hundred microns depending on the processing technique. Tiny compact tension samples fractured under fatigue loading were examined using White Light Interferences Microscope (WLIM), Scanning Electron Microscope (SEM), Atomic Force Microscope (AFM) and Ultrasonic Force Microscope (UFM). The surface topography measurements along the direction of loading and crack growth direction are compared with macroscopic (da/dn) curve measurements. Grain size measurements performed using SEM and AFM/UFM are compared. Very high magnification AFM and UFM images are analyzed to obtain information about possible mechanisms of deformation and crack growth.

ACKNOWLEDGEMENTS

I would like to thank Dr. Shamachary Sathish for his tremendous patience, guidance and encouragement through out my masters program at University of Dayton. His suggestions helped in successful completing this research.

I am grateful to Dr. Michael Gigliotti for providing with a sufficient date and helping in analyzing it, also for critical review of manuscript of my thesis.

I express my gratitude to Dr. Daniel Eylon for being part of my thesis and also for encouraging in completing of thesis.

I would also like to thank P.R.Subramanian for providing the samples required for this study and also for financial support.

I would like to acknowledge Global Research (G.E), Department of Materials Engineering and Graduate school for financial support.

I also thank Vijay Nalladega for training me on AFM-UFM instrument, Eric Burke for training me on White light interference microscope, Andy Phelps for training me on Scanning electron microscope and Harikrishna Ambalam for the help on this research project. My special thanks to my finance Sujith Kumar Racha for being supportive and helping me in my thesis documentation.

I sincerely thank University of Dayton for giving this opportunity to conduct this research.

TABLE OF CONTENTS

	Page
ABSTRACT.....	ii
ACKNOWLEDGEMENTS.....	iii
LIST OF TABLES.....	vii
LIST OF FIGURES.....	viii
CHAPTER 1.	
INTRODUCTION.....	1
1.1 Microscopic Fracture Surface Analysis.....	4
1.12 Hall-Petch Relation.....	7
1.2 Outline of Thesis.....	9
CHAPTER 2.	
EXPERIMENTAL METHODS.....	11
2.1 Introduction.....	11
2.2 White Light Interference Microscope.....	12
2.2.1 Principle and Working.....	13
2.2.2 Applicability and Limitations.....	17
2.3 Experiment.....	18

2.4 Atomic Force Microscope.....	19
2.41 Principle and Working of AFM	19
2.5 Contact Mode.....	23
2.6 Ultrasonic Force Microscope.....	24
2.7 Experiment.....	25
CHAPTER 3	
MATERIAL.....	27
3.1 Introduction.....	27
3.2 Cryogenically-milled Ni-20wt. %Cr, crack oriented in r-z plane of extrusion.....	29
3.3 Cryogenically- milled Ni-20wt. %Cr, with crack plane normal to extrusion direction.....	31
3.4 Cryogenically-milled Ni-20wt. %Cr+Al ₂ O ₃ , with crack plane normal to the extrusion direction.....	32
3.5 Multi-axis forged Ni-20wt. % Cr.....	33
3.6 MA754HT.....	36
CHAPTER 4	
FATIGUE FRACTURE SURFACE ANALYSIS USING WHITE LIGHT	
INTERFERENCE MICRSCOPE.....	38
4.1 Introduction.....	38
4.2 Results.....	41
4.3 Comparison between Surface Roughness and Crack Growth Rate	43
CHAPTER 5.	
Microstructural Analysis.....	64

5.1	Importance of Fractography.....	64
5.2	Advantage of AFM-UFM in Fractography.....	65
5.3	Results.....	66
5.4	Comparison of AFM-UFM images with SEM.....	81
5.5	Discussion.....	85
CHAPTER 6		
	Conclusions.....	88
LIST OF REFERENCES.....		90

LIST OF TABLES

Table	Page
4.1 Surface and 3D images of sample # 1 taken from white light interference microscope.....	42
4.2 Surface roughness measurements of sample #1 with respect to crack length.....	45
4.3 Surface and 3D images of sample # 2 taken from white light interference microscope.....	47
4.4 Surface roughness measurements of sample #2 with respect to crack length.....	48
4.5 Surface and 3D images of sample # 3 taken from white light interference microscope.....	50
4.6 Surface roughness measurements of sample #3 with respect to crack length.....	53
4.7 Surface and 3D images of sample #4 taken from white light interference microscope.....	53
4.8 Surface roughness measurements of sample #4 with respect to crack length.....	55
4.9 Surface and 3D images of sample #5 taken from white light interference microscope.....	57
4.10 Surface roughness measurements of sample #5 with respect to crack length.....	60

LIST OF FIGURES

Figure	Page
1.1 Plot between the number of cycles and crack size.....	2
1.2 Plot between stress intensity factor and crack growth rate.....	3
2.1 Principle of white light interference microscope.....	13
2.2 Schematic of magnification head.....	16
2.3 Schematic of contact mode AFM.....	20
2.4 Schematic of Ultrasonic force microscope.....	24
3.1 Compact tension sample.....	28
3.2 Fatigue fracture surface image of Ni-20wt.%Cr.....	30
3.3 Plot between crack growth rate and stress intensity factor.....	30
3.4 Fatigue fracture surface image of cryogenically milled Ni-20wt.%Cr	31
3.5 Plot between crack growth rate and stress intensity factor	32
3.6 Fatigue fracture surface image of Ni-20wt.%Cr+Al ₂ O ₃	33
3.7 Plot between crack growth rate and stress intensity factor.....	33
3.8 Fatigue fracture surface image of C1 Forged Ni-20wt.%Cr.....	35
3.9 Plot between crack growth rate and stress intensity factor.....	36
3.10 Fatigue fracture surface image of MA754HT.....	37
3.11 Plot between crack growth rate and stress intensity factor	37

Figure		Page
4.1	Optical image of Ni-20wt.%Cr.....	41
4.2	Graph plotted between crack length, crack growth rate and surface roughness.....	45
4.3	Optical image of cryomilled Ni-20wt.%Cr.....	46
4.4	Graph plotted between crack length, crack growth rate and surface roughness.....	49
4.5	Optical image of Ni-20wt.%Cr+Al ₂ O ₃	50
4.6	Graph plotted between crack length, crack growth rate and surface roughness.....	53
4.7	Optical image of C1-Forged Ni-20wt.%Cr	53
4.8	Graph plotted between crack length, crack growth rate and surface roughness.....	55
4.9	Optical image of MA754HT.....	56
4.10	Graph plotted between crack length, crack growth rate and surface roughness.....	60
4.11	Plot between stress intensity factor and crack growth rate.....	61
4.12	Graph between crack growth rate and surface roughness.....	62
4.13	Graph between stress intensity factor and surface roughness.....	63
5.1	Schematic of macroscopic fracture surface.....	65
5.2	Optical image of Ni-20 wt.%Cr.....	67
5.3	AFM-UFM image of Ni-20wt.%Cr sample at position 2-4.....	67
5.4	AFM-UFM image of Ni-20wt.%Cr sample at position 5-6.....	68
5.5	AFM-UFM image of Ni-20wt.%Cr sample at position 7-9.....	69
5.6	Optical image of cryogenically milled Ni-20 wt.%Cr	69

5.7	AFM-UFM image of cryogenically milled Ni-20wt.%Cr sample at position 1-2.....	70
5.8	AFM-UFM image of cryogenically milled Ni-20wt.%Cr sample at position 4-5.....	71
5.10	Optical image of Ni-20 wt.%Cr +Al ₂ O ₃	72
5.11	AFM-UFM image of Ni-20wt.%Cr+ Al ₂ O ₃ sample at position 2-4.....	73
5.12	AFM-UFM image of Ni-20wt.%Cr+ Al ₂ O ₃ sample at position 5-7.....	74
5.13	AFM-UFM image of Ni-20wt.%Cr+ Al ₂ O ₃ sample at position 7-8.....	75
5.14	Optical image of C1 Forged Ni-20wt.%Cr.....	75
5.15	AFM-UFM image of C1 forged sample at position 1-2.....	76
5.16	AFM-UFM image of C1 forged sample at position 3-4.....	77
5.17	AFM-UFM image of C1 forged sample at position 6.....	77
5.18	Optical image of MA754HT	78
5.19	AFM-UFM image of MA754HT sample at position 3-4.....	79
5.20	AFM-UFM image of MA754HT sample at position 5-6.....	79
5.21	AFM-UFM image of MA754HT sample at position 6-7.....	80
5.22	AFM-UFM image of MA754HT sample at position 8-9.....	81
5.23	SEM and AFM-UFM images of Ni-20wt.%Cr.....	82
5.24	SEM and AFM-UFM images of cryogenically milled Ni-20wt.%Cr ...	82
5.25	SEM and AFM-UFM images of Ni-20wt.%Cr+Al ₂ O ₃	83
5.26	SEM and AFM-UFM images of C1 forged Ni-20wt.%Cr.....	84
5.27	SEM and AFM-UFM images of MA754HT.....	85

CHAPTER 1

INTRODUCTION

Fatigue fracture mechanics is an important study for the understanding and prevention of many structural failures. The failure may originate from existing cracks, flaws, defects *etc.*, or those which may nucleate and grow under cyclic loading. Extensive research has been performed over several years to identify the nature of structural failures. An early quantitative analysis of fatigue failure was provided by Inglis in 1913, which deals with stress analysis. Later, Griffith in 1921 provided energy concepts for failure and crack growth. However, practical implementation of the ideas to failure and deformation of components came from studies by Paris *et al.* In 1961, Paris, Gomez, and Anderson proposed that the fatigue crack growth per stress cycles da/dN , increases with stress intensity factor ΔK during constant amplitude cyclic loading. This “Paris Law” description of fatigue crack growth is used today.

The rate of fatigue crack growth can be determined by using a compact tension specimens fractured under fatigue loadings. The increase in the crack length growth Δa , is measured with respect to the number of cycles ΔN . A graph is plotted between these parameters in *Figure 1.1* which represents the crack growth data. The slope of the curve in *Figure 1.1* at a point is called as fatigue crack growth rate.

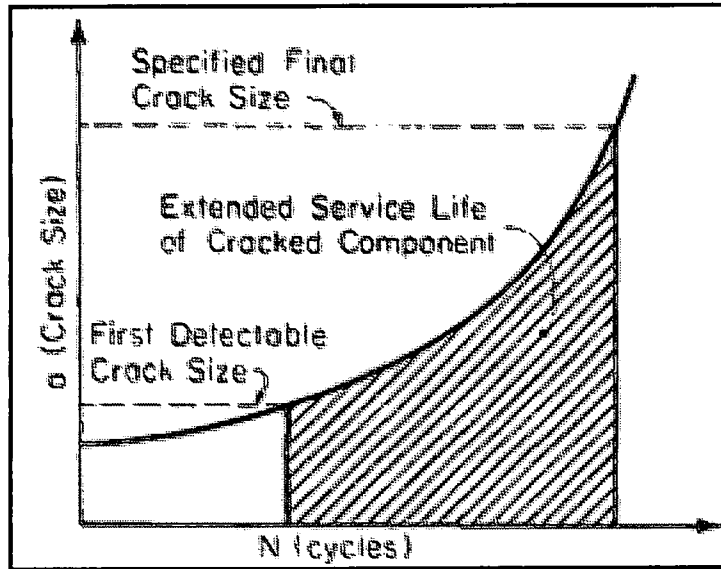


Figure 1.1: Plot between the number of cycles and crack size[8]

Thus, the calculated slope da/dn and stress intensity factors ΔK are plotted in a *Figure 1.2* which is a logarithmic plot, from which a smooth curve independent of load magnitude and crack geometry is obtained. These curves are computed by Paris, Gomez and Anderson in 1961 and a numerical relationship is cited as follows

$$da/dn = C (\Delta K)^m$$

Where C and m are material constants. Paris relation is applicable to the middle region of the curve, where the change of $\log (da/dn)$ with respect to $\log (\Delta K)$ is linear where that in region II. Region I represent small da/dn values with corresponding stress intensity factor which is a minimum value, termed a “threshold” value, below which a crack doesn’t grow. In region III, there is rapid crack growth, and it is accelerated until stress intensity factor reaches a critical value. Paris equation is limited to Region II, it is not applicable for Region I and Region III.

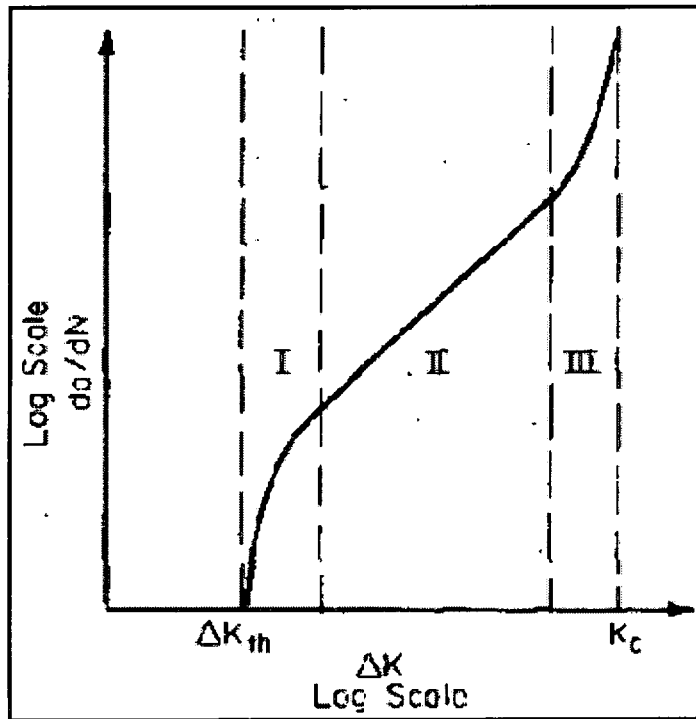


Figure 1.2: Plot between stress intensity factor and crack growth rate[8]

Surface roughness is one factor in resistance to fatigue crack growth. On a free surface, roughness can introduce stress raisers in a material which reduce the time to crack initiation and thus lower fatigue life. Surface roughness is important factor affecting fatigue life because it is directly related to the level and number of stress concentrations on the surface. If the stress concentration is high then crack nucleation will be very early, which affects the total life of material. Conversely, a rough fatigue crack path, may reduce the rate of fatigue crack growth, and increase fatigue life. Thus, affect of surface roughness on fatigue fracture surface plays an important role. Hence the analysis of surface roughness was performed in this study.

Fractography, as it is known, provides information about, why and how a failure occurred. Analysis of surface features, including surface roughness of fractured surfaces provides insights into failure analysis and reconstruction of failure modes. The surface

roughness created during fatigue fracture depends on several factors the microstructure of the material, presence of second phases, voids, inclusions, crystallographic texture, *etc.* Several investigators have attempted to relate the surface roughness to evaluate fracture parameters. In a recent study, Y.Murakami [1] has attempted to obtain fracture parameters, by measuring surface roughness on the fractured surfaces of material using AFM. This thesis examines surface roughness measured using white light interference microscope, on fractured surface of Ni-20 wt. % Cr compact tension tested specimens, with varying grain sizes. The surface roughness along the crack growth direction is compared with crack growth rate measurement performed using electrical potential method.

In order to perform this study, white light interference microscopy is used. It comprises non-contact optical profilers, which use a vertical scanning interferometry technique to measure roughness of a material. The white light interference microscope has a vertical resolution of 3nm, a lateral surface resolution of 0.2 μ m and a scan length of 250 μ m. It can produce real time high resolution 3-D evaluation of surfaces with roughnesses as high as 500 μ m and accuracy of 3nm RMS. The profilometer contains an image analysis package that enables automated topographical calculations. Thus, surface parameters such as roughness values are obtained on the fracture surface of the fatigued material and related to the crack growth rate.

1.1) Microscopic Fracture Surface Analysis

The microscopic characterization of cyclic deformation and crack growth has been the topic of considerable research in past decades. The fatigue fracture surface micrographs reveal the nature of fracture mechanism taking place in the material. Thus the

fractography can play an important role for analyzing the failure mechanism. In this study, the AFM-UFM techniques are used to analyze the behavior of the fatigue fracture surfaces. Previously, optical and scanning electron microscopes were used to describe the microscopic features of fatigue fracture deformation. In 1903, Erwin and Humfrey published optical micrographs of Swedish iron, which is a polycrystalline material where slip bands were observed in most of the grains. Thompson, Wadsworth and Louat in 1956 demonstrated the persistent slip bands, and Zappfe and Worden in 1951 observed the markings in a type of ripples on the fatigue fracture surfaces and thus addressed them as fatigue striations. Forsyth and Ryder in 1960 related the spacing between adjacent striations with that of rate of fatigue crack growth.

Microstructure of a fatigue fractured surface exhibits the mechanics of crack growth by the variation of surface topography. In order to observe and interpret the nature of fracture from the microstructure, a good image is necessary. The quality of an image is a major factor in determining the effectiveness of interpretation. In early work, fracture surfaces were observed by the naked eye with natural binoculars, but the illumination of the surface at shallow angles produced shadows because of the axis of the camera was normal to the average plane of fracture. Shadows were also caused by the rough, irregular bands, ridges and valleys of the fracture surface.

Later, optical microscopy was used with simple microscopes. The images produced by this microscopy are as direct as that of the naked eyes with the only difference is features can be observed at magnifications up to about 100X. But, as the fracture surfaces are very rough at some scale, the useful magnification in optical microscopy is often much less, and the illumination is an important aspect in order to reveal surface contours and also

the details of shadows formed in fractured surfaces. But in optical microscopy, good vertical illumination is relatively difficult.

The scanning electron microscopes are important for characterizing the fatigue crack growth from the fatigue fracture surfaces. The range of magnification is very high, up to around 1nm, and depth of field in the image is 300 times more than the depth of field of the optical microscope. Thus, images produced by this instrument are more magnified images of the sample, with details not visible by optical techniques. Though it is easy to obtain attractive and informative images by scanning electron microscopy, it is difficult to obtain quantitative topographical information. Thus, until now scanning electron microscope has been used for qualitative microstructural analysis of fracture surfaces.

With the advent scanning probe microscopes like AFM, an extension of this research is done. In this thesis higher magnification images are obtained. The AFM has opened an avenue to study fractured surfaces with unprecedented nano resolution. Investigation of fracture surfaces of Ni-20wt. %Cr by these instruments reveal the minute details at nanoscale and detect nanoscopic deformation. Previously, quantitative analysis of fatigue crack growth is limited by the lack of available techniques, as it is difficult to obtain and observe the quantitative measurement of the slip bands evolved in the fatigue fracture material. Studies on crack growth techniques [2-5] lack the necessary resolution for the measurement of slip band characteristics. In the polycrystalline materials, the height and spacing of slip bands will be in the range of submicron to nanometers. But the typical resolution of SEM is $> 100 \text{ \AA}$ which may not be suited for the surface topographic image. Thus SEM cannot provide the vertical depth information of the surface features which are an important aspect for the measurement of slip bands. AFM is capable of

imaging the fatigue fracture samples with the lateral resolution of 2\AA and vertical resolution of 0.1\AA [6-7]. In AFM, the contrast of the image is the digital difference of vertical depths of surface features. Surface heights and roughness of the material can be obtained. As long as slip bands on the surface of the material are larger than the surface roughness, AFM can perform the quantitative measurement of surface topography. The magnification of AFM is in three dimensions, that is in horizontal X- Y plane and in vertical Z dimension. The study of failure mechanisms due to fatigue loading is limited to low resolution optical microscope though SEM has increased resolution but it is limited to the two dimensions. Until now, the quantitative analysis of failure mechanism on three dimensions is difficult to obtain. By using AFM techniques, precise quantitative information on the three dimensions can be obtained.

When the sample surface is very flat, the contrast of the image produced by AFM is not good enough so to enhance the contrast of nanoscale features an ultrasonic force microscope is used. The surface elastic properties of material enhance the contrast in UFM images. In this research, AFM-UFM techniques are explored to obtain good quality of images and to analyze the possible mechanism of deformation and the crack growth, the grain size measurements are performed using SEM and AFM-UFM techniques.

1.12) Hall-Petch Relation

The Hall-Petch relation describes the scaling of yield strength with grain size of polycrystalline solids. That is, the larger the grain size of a crystallite material, the smaller is its yield strength. An explanation of the Hall-Petch relation comes from dislocation pileup theory. Hall demonstrates the relation between the grain size and the lower yield point. In his paper he explains about dislocation motion, when a dislocation

occurs in a material the stress raisers makes the deformation process to propagate but the grain boundaries acts as obstacles. Thus dislocation pile up takes place behind the grain boundaries and the stress concentration at the tip of the slip plane increases and will eventually cause grain boundary to yield. Hence the deformation is transferred to next grain. Then he related the crack length or the length of slip band with mean grain size.

Hall equation:

$$\sigma_{LYP} = \sigma' + \frac{k_H}{\sqrt{d}} \quad (1)$$

Where “d” is the diameter of the grain and “ σ_{LYP} ” is the yield strength of a polycrystalline material.

Petch in his paper explains about the brittle failure of the steels. A steel specimen is tensile tested at liquid nitrogen to obtain brittle fracture which is free of surface flaws. Cleavage strength and fracture stress were measured. Petch results obeyed the following equation

Petch equation:

$$\sigma_c = \sigma_0 + \frac{k_P}{\sqrt{l}} \quad (2)$$

Where “l” is the mean intercept length and some amount of plastic deformation is observed has been neglected. He analyzed the tip of the dislocation pile up as Griffith flaws and stated that the tensile stresses at the end of a pile-up was quite high and these dislocations would pile –up at the opposite ends of a grain and the maximum value of n would be obtained when the Frank-Reed source is at center of a grain. An array of n dislocations could pile-up over half the grain diameter at given stress. Thus by measuring

variation in cleavage strength with respect to ferritic grain size, he found relationship exactly similar to that of Hall. So this equation is named after both Hall and Petch.

Hall-Petch equation

$$\sigma_y = \sigma_0 + \frac{K}{\sqrt{d}} \quad (3)$$

Where “d” is the diameter of a grain, K is a material constant, “ σ_0 ” is material constant for starting stress for dislocation movement, and “y” is the yield stress.

In a material undergoing fatigue, grain size influences both crack initiation and propagation. The quantitative description of this relation is explained in above equation 3.

When a material posses fine grains then the strength of the material will be high. Priddle previously established the influence of grain size on the yield strength with the following Hall -Petch equation for 316L stainless steel. Thus the equation 3 can be used to estimate the change in yield strength with the grain size. Thus, the Hall Petch equation 3 is used to relate the grain size with other properties, such as fatigue limit, toughness, creep rate, hardness and fracture strength in stress corrosion cracking. In this study, Ni-20 wt. %Cr sample with varied grain sizes are calculate from the AFM-UFM images and SEM images, then the change in the yield strength with the grain size of Ni-20wt. %Cr respectively.

1.2) Outline of the thesis

Chapter II discusses about the instrument that is used to study the surface roughness of the material and also about the microscopes that used to study the mechanism of the crack growth in the material. It discusses how the experiment has been carried out.

Chapter III discusses about the material that has been used in the study and a little emphasis was made on its process techniques, then Paris curves for each sample are plotted in this section

Chapter IV discusses how fatigue fracture analysis was carried out using white light interference microscope. The surface profile of each sample at different positions is determined and the relation between surface roughness and the crack growth rate was discussed.

Chapter V discusses about the microstructure of the fatigue fracture Ni-20wt. %Cr sample using atomic force microscope and ultrasonic force microscope. In this section grain size measurements are performed and are compared using SEM and AFM-UFM techniques.

CHAPTER 2

EXPERIMENTAL METHODS

2.1) Introduction

Characterization of fracture surfaces can be performed by general techniques such as optical microscopy, and scanning electron microscopy (SEM). Though the conventional optical microscope and SEM are used for fracture surface analysis, it is difficult to obtain quantitative analysis of images using these techniques. The work described herein performs quantitative analysis of fracture surfaces by using newly-developed instruments, such as the white light interference microscope (WLIM), the atomic force microscope (AFM), and the ultrasonic force microscope (UFM). WKYO NT 8000 a white light interference microscope is used to analyze the surface profile of fatigue-fractured Ni-20wt.%Cr samples. WLIM is more advantageous over the conventional optical techniques, because height profile can be measured in deep valleys and holes of fractured surfaces, since the illumination and observation are coaxial. Thus, the surface parameters can be analyzed easily using this technique.

The surface topography at larger resolution can be obtained by a conventional SEM technique, but the quality and resolution of the images are restricted to the large grain materials. The grain size of material used in this experiment varies from few microns to

down to nanometers. Even at higher magnifications, the images obtained from SEM are not convincing to analysis the fracture mechanism. In order to obtain high quality images at nanoscale, an atomic force microscope and ultrasonic force microscope were used. A Digital Instruments Dimension 3000 Nanoscope IIIa AFM instrument is used for this experiment. The images obtained from these techniques reveal many patterns of fracture at nanoscale, at higher magnification and resolution than SEM, and these AFM-UFM images are more informative than those from SEM technique. Thus, the fracture mechanism of the material at nanoscale can be determined by the quantitative analysis of surface topography using AFM-UFM. As the working of the conventional optical microscope and scanning electron microscope was studied in past few decades and is well-known to all, only a brief discussion of newer techniques is necessary.

2.2) White Light Interference Microscope

Material characterization can constitute the determination of all aspects of a material that are significant for a particular application, including: composition and structure, including defects; mechanical and physical properties, *etc.* A very wide variety of techniques have been used for characterization of materials. It has become increasingly important to be able to accurately characterize surface texture. Surface texture is a key factor affecting the functionality and reliability of certain components. It can also act as a diagnostic tool for monitoring the process that produces the product. For the study of surface texture analysis, white light interference microscope (WLIM) is used which is powerful tool for optical measurements. While this instrument is a recent development, it is a combination of interferometry and microscopy techniques. White light interference compute several surface parameters that provide information about roughness and the

surface profile and also the parameters such as peaks, valleys, profile symmetry *etc.* It is non-contact optical profiler that uses two techniques to measure surface heights. Phase shifting interferometry (PSI) mode allows measuring smooth surfaces, while vertical scanning interferometry (VSI) mode allows measuring rough surfaces and steps. This system is a suitable method for height profile measurement of an object as it is capable of generating full field view and three dimensional surface topography in vertical scanning interferometric mode.

2.21) Principle and Working

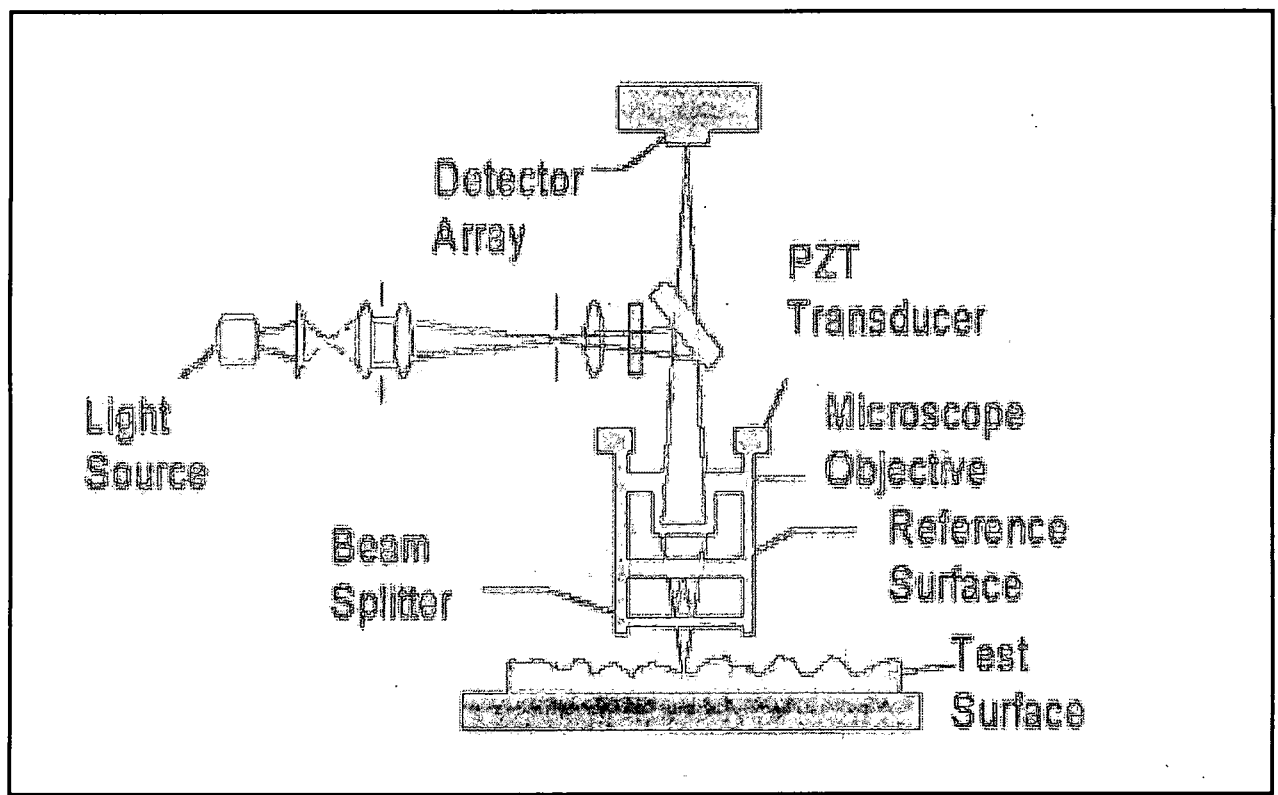


Figure 2.1: Principle of white light interference microscope [15]

A white light microscope is essentially a Michelson Interferometer. A parallel beam of white light from a source passes through an objective of a microscope and interferometer and focuses onto the surface of a sample. A beam splitter splits the beam of white light into two parts. One reflects off the surface of the sample and other reflects off a reference mirror. The two reflected beams recombine at beam splitter and form interference fringes. These fringes are detected by a CCD or video camera that consists of array of detectors. The intensity of each detector corresponds to a position on the surface of the object. An objective of interferometer is moved in a vertical direction to measure the surface height of a sample. Fringe contrast increases at minimum optical path difference as the microscope interferometer is scanned vertically in equally spaced steps. Since the white light has a short coherence length or fringe contrast, the interference fringes are present over a shallow depth. Amplitude of each element of the array of CCD is recorded by computer during vertical scanning. The intensity data of each element is converted into surface height by using a computer algorithm. Thus, the surface topography image is obtained by mapping the amplitude of each element from the entire array. This data is analysed by software available with the microscope. The image thus obtained is divided into x and y positions, hence it can be used to view the line by line variation across the imaged view of the sample. The resolution of microscope depends on the number of arrays on the CCD.

Microscopic unit

The main unit of the system is interferometric microscope and its related hardware. The interferometric microscope is the unit that allows focusing on the sample.

Z axis

The Z axis is the vertical post at the back of the unit that supports the camera housing, the illuminator, and the magnification objective. It may also support an auto tip-tilt head. As focus knobs are turned, the magnification objective moves up and down.

Field of view assembly

The field of view assembly allows selecting various lens tube positions for use in aligning the system or focusing on a sample. Up to four lens tubes are contained within the detector housing. When equipped with the optional 0.5X, 0.6X, 0.75X, 1.5X, 2.0X lens tubes, the field of view assembly allows changing the magnification factors of the magnification objective in use.

Auto-filter assembly

The auto filter assembly consists of light source and software controlled narrow band wavelength filters. This system quickly scans the test surface and detects any large step regions.

Magnification head

This system is equipped with one or more single magnification heads, or it may have a turret, which houses multiple objectives. Before making measurements, correct objective must be positioned properly or else the turret can be used to rotate the lens.

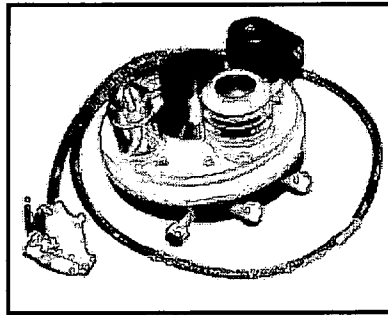


Figure 2.2: Schematic of magnification head[15]

Sample stage

The sample stage is located beneath the magnification objective. The stage may or may not have a special fixture for sample, depending on the way the sample is mounted.

Illumination system

Illuminator contains two levers for use in adjusting the aperture and field stops. The aperture stops controls the amount of light entering the interferometer. The field stop limits the field of view on the video monitor when closed.

Video camera system

The video camera sends a real-time image of a sample to video monitor.

Video monitor

The video monitor provides a real time image of the sample as seen through the magnification objective. During alignment and focusing, a video monitor screen is used to view the reflected images of the sample and internal reference mirror.

Interface control box

The interface control box contains the electronic components that link the measurement information to the computer.

Vertical scanning interference mode (VSI)

The surface heights of the sample are measured by the two techniques they are;

1. Phase shifting interferometry (PSI) mode.
2. Vertical scanning interferometry (VSI) mode.

In the present study, vertical scanning interferometry mode was used to collect the surface topography data on the Ni- 20wt.%Cr samples at 20X magnification.

Vertical scanning interference mode works on the basic principle of white light interference microscope as mentioned above. The sample is placed vertically, such that each point on the surface passes through focus. Maximum fringe contrast of the white light source is obtained at the point of best focus. In this technique the white light source is not filtered, the degree of fringe modulation is measured but not a phase interference fringes. In VSI mode white light source works best as this technique depends on the high modulation at a precise focus point as white light has short coherence length. It is most effective technique for rough surfaced samples. In VSI the focus precision is in nanometer range. VSI can measure rough surfaces and steps up to several millimeters. The vertical resolution of VSI mode is in a range of 3nm-1nm. The lateral resolution is a function of magnification objective and detector array size. Each magnification objective has its own resolution. So in order to determine the surface profile for fatigue fractured samples vertical scanning interference mode is used which also posses higher resolution.

2.22) Applicability and Limitations

White light interference microscope enables non-contact, real time high resolution, 3D evaluation of surfaces with the roughness as high as 500 μm and an accuracy of 3nm RMS. Scan length is 250 μm and its lateral resolution is 1 μm , vertical resolution is 3nm.

Although optical techniques offer many advantages, there has been reluctance in adopting these techniques because of their lower resolution in in-plane direction, complicated operation and analysis procedures. Lateral measurement range is limited by size of the beam splitter. In order to measure the height profile the sample needs to be moved which renders the measurement process slow.

2.3) Experiment

Objective

An objective of this experiment was to obtain the surface topography at lower magnification and to measure changes in the surface heights and to calculate the surface roughness of fatigue fractured Ni-20wt.%Cr samples. White light interference microscope used was a WKYO NT 8000 instrument.

Experimental procedure

In this experiment there was no need of sample preparation. Experimental procedure was similar to that of the optical microscope. A sample was placed on the sample stage under the magnifying lens (20X, 100X, 250X) and was focused by adjusting X,Y and Z axis. In this study all the images were taken at 20X magnification. White light source hits the surface of sample and was reflected off the reference mirror and produced the fringe patterns on the images. Thus, the fringes at this point represented the surface area of the sample that was in focus. Images of Ni- 20wt.%Cr samples were obtained at positions starting from the notch and precrack region, and sequentially towards the post-fatigue region, in which the crack growth rate was slow, to determine surface topographical differences and surface height changes across the sample surface. Thus the surface

roughness values of fatigue-fractured material were obtained from white light interference microscope.

2.4) Atomic Force Microscope

Atomic force microscope is the most widely used microscope among all the scanning probe microscopes, because of its applicability in a wide range of technologies such as electronics, biological, chemical, aerospace, energy industries etc. AFM is mainly used as surface profiler which not only images the surface at atomic scale but also measures the force at nano-newton scale. When compared to the tools like optical microscope, scanning electron microscope and transmission electron microscope, the main advantages of AFM over these tools are:

1. It can produce extremely high magnification upto 1,000,000X;
2. It can obtain three dimensional surface topography i.e., magnification in X-Y& Z axes enabling revealing the depth of surface features or cracks in fatigue fracture surfaces;
3. Sample preparation is not necessary for the measurements using AFM.

2.41) Principle and Working of AFM

AFM was introduced in 1985 by Gerd Binnig, Quate and Christoph Gerber. The principles of AFM represent the working of record player or stylus profilometer.

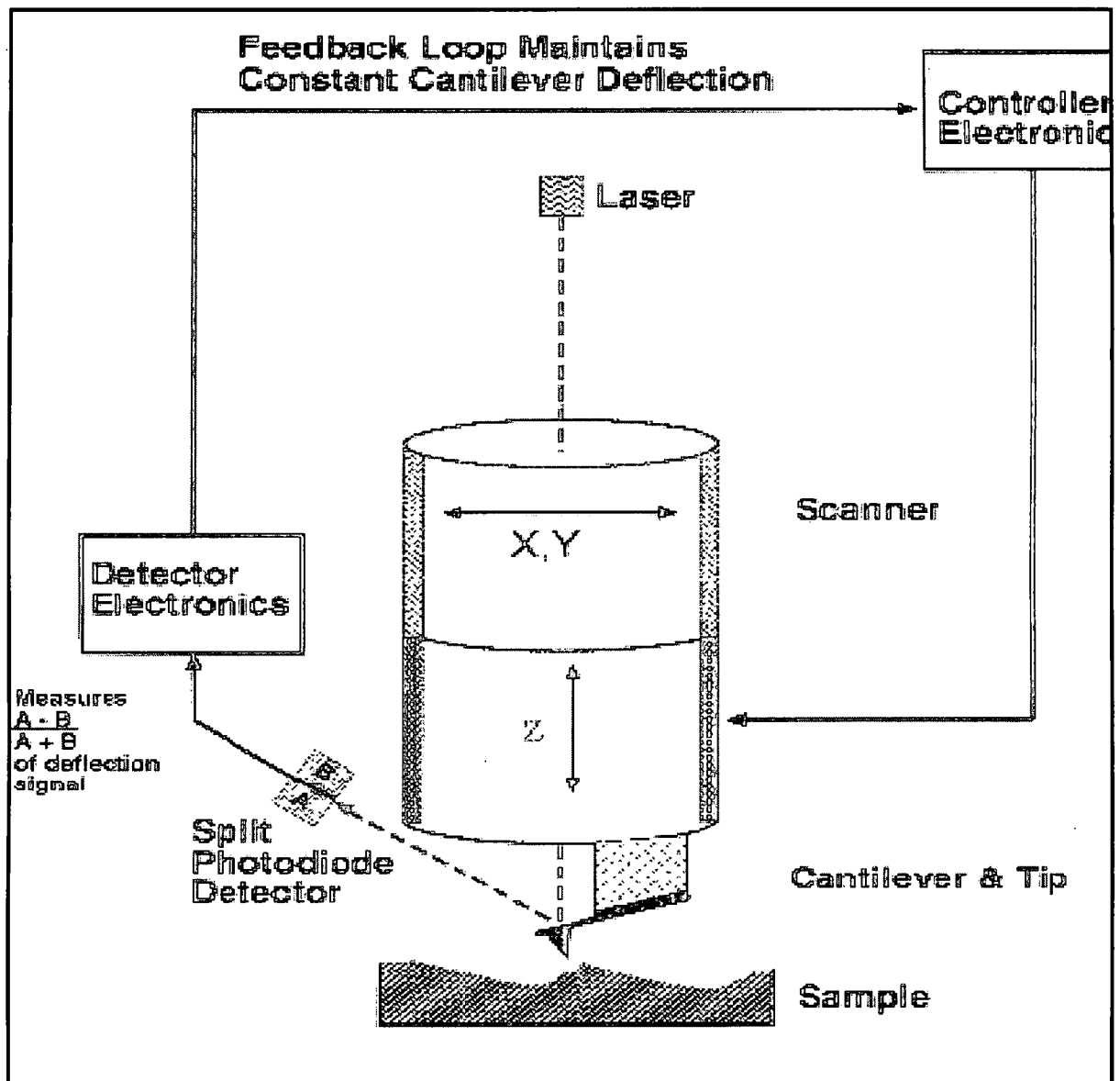


Figure 2.3: Schematic of contact mode AFM [10]

When a tip attached at the end of a cantilever is brought in a contact with the sample surface then an interatomic potential will develop between the atoms of the tip and the atoms of sample surface. As the tip is raster scanned across the surface using piezo electric scanner, which maintains tip-sample distance based on the setpoint determined by user, then these interatomic potentials will force the cantilever to bounce up and down

resulting in the deflection of the laser beam. This laser beam which is aimed at the back of the cantilever-tip assembly is reflected off the cantilever surface onto the split position sensitive photodiodes measuring cantilever deflections by the detection system. A feedback loop maintains a constant tip-sample separation by moving a piezo electric scanner in Z direction in order to continue the setpoint deflection. Thus, by maintaining a constant tip-sample separation and using Hooke's law, forces between tip and sample can be calculated. Topographic images are generated through a computer as a measure of distance traveled by the scanner in Z direction relative to the x-y plane [9].

“AFM consists of a piezo electric scanner, tip assemble, detection system and a feed back loop”

Piezoelectric scanner

In AFM, the scanner controls the movement of the tip or sample in X, Y & Z directions. The scanner is made up of independently-operated piezo electrodes for X, Y & Z in single tube which can manipulate samples and probes with extreme precision in three dimensions. Usually in AFM, scanners are made of piezoelectric materials which can expand and contract according to an applied voltage. These scanners posses AC voltage in a range of +220V to -220V [10]. Typically an AFM scanner can scan laterally from 10 angstrom to 100 microns and vertically from sub angstrom to 10 microns.

Tip assembly

Tip assembly mainly consists of a tip and cantilever i.e., a sharp tip is attached at the end of cantilever which comes in contact with the sample surfaces. AFM tips can act as sensors that respond to the force and also as a detector that measures the sensors response. The major factors that need to be considered for AFM tips are:

1. Aspect ratio, 2. Radius of curvature of a tip, and 3. Stiffness [11]. Tips used are usually short and thin. If they are short, they maintain high resonant frequency which can reduce noise vibrations and if they are thin, then small force constant is maintained so that large deflections with small force can be obtained. Pyramidal shaped tips are used in AFM with half angle of 35 degrees and radius of curvature between 20-60nm with a force constant approximately equal to 0.5N/m. Commonly used AFM tips are made of stiff material such as Si_3N_4 , silicon or silicon oxide.

Cantilever plays an important role in imaging AFM. The deflections of a cantilever determine the sensitivity and resolution of AFM. Cantilevers are not springs; they are manufactured either as long thin strips or V shaped frame style to increase the lateral rigidity. In contact mode, the cantilevers should be soft enough to deflect by very small forces and should possess high resonant frequency in order to avoid vibration instabilities. The thickness of cantilever can be measured by the resonance frequency and length of cantilever is approximately 100-200 μm .

Detection system

The most commonly used detection systems are optical detection or Beam Bounce method. Beam Bounce detection is done using a diode laser which is used in present instrument. Position sensitive detector system consists of two circular detectors divided into two quadrants which are closely spaced photo diodes [10]. The laser beam from the scanner, which is reflected off the upper surface of the cantilever, is imposed onto these photodiodes. If there is any angular change in the deflection of cantilever, these photodiodes will detect the orientation producing the difference in the signal which is

proportional to the deflection of cantilever which in turn is collected by a differential amplifier. This detector system can detect the deflections of the cantilever less than 1Å

Feed back loop

The feedback control unit takes in the signal from position sensitive photodiode and generates the images by controlling the positioning of cantilever leading to obtain changes in the force between the tip and sample. The amount of deflection can be calculated with a height as cantilever obeys Hooke's law. In order to maintain constant deflection set point, peizo should adjust accordingly as tip-separation. The Operation of AFM can be done with or without the feed back control. Since the tip is raster-scanned across the surface when the electronic feedback is switched on, the peizo will adjust the tip-sample separation maintaining a constant deflection or the force will remain same as it is topographically true. The microscope is said to be operating in constant height or deflection mode when the feedback is switched off. This particularly is useful for imaging very flat samples at high resolution.

2.5) Contact Mode

This is most commonly used mode wherein the tip at end of cantilever scans the sample in a close contact with the surface. In this method, repulsive forces are acting in between the tip and the sample surface, as the cantilever has a low spring constant. The cantilever moves along the topographic features of surface which leads to the deflections in different orientations which are detected by the photodiodes. In order to obtain topographic data AFM is operated by one of these two modes such as constant force or constant height mode.

In constant force mode the deflection of the cantilever is applied as an input to a feed back loop which moves the scanner up and down in the Z directions relative to the topography by keeping the cantilever deflection constant. In this way total force applied by cantilever is constant [9]. Other method is constant height mode in which the sample height is fixed during scanning. So the variations in cantilever deflection can be used directly to generate topographic data. In contact-mode, usually the constant-force mode is used. The main advantage of contact-mode is its high scan speed, and it is the only technique from which atomic resolution images can be produced. In contact-mode it is easy to scan rough samples with extreme variation in topography.

2.6) Ultrasonic Force Microscope (UFM)

Ultrasonic force microscope is one of the techniques based on AFM. It has been developed to improve the contrast of image compared to that of AFM images especially for flat surfaces and to obtain more surface details such as elastic properties at nanoscale.

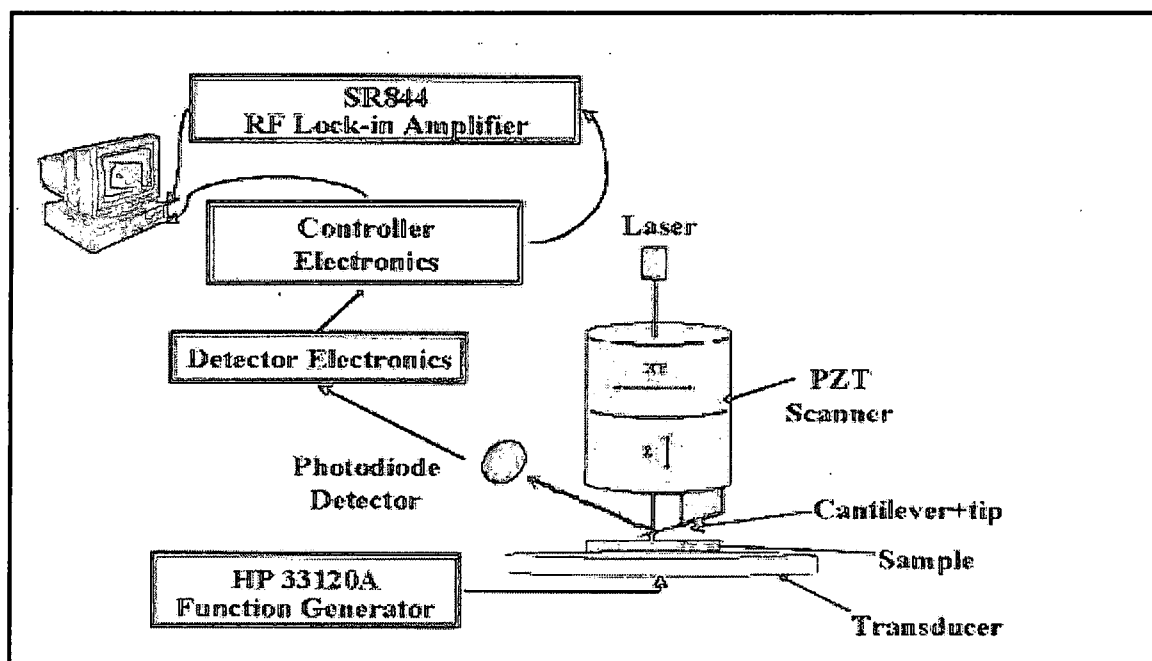


Figure 2.4: Schematic of Ultrasonic force Microscope [14]

Working

In UFM, a piezoelectric transducer is attached at one end of sample surface and other end of surface is in contact with a tip which is used in AFM. Ultrasonic frequency signals will excite the transducer which produces an acoustic wave in the sample. The elastic contact and the adhesion interaction between the tip and the surface forces the tip to vibrate but the frequency at which the sample is vibrated is much higher than the resonant frequency of the cantilever. Thus the propagation of acoustic waves through the sample generates surface displacements which are detected by the AFM tip. UFM images are displayed by the measurement of differential amplitude or differential phase by a photo detector [13].

2.7) Experiment

Objective

An objective of this experiment was to analyze the surface topography of fatigue-fractured Ni- 20wt.%Cr samples and to derive the crack growth from the AFM/UFM microstructure images.

Experimental procedure

A sample was attached to a piezoelectric transducer by means of a coupling medium such as honey, and the other side of the transducer was connected to an HP function generator which generated continuous sinusoidal wave. The signal from the function generator was fed into the Stanford Research Systems lock-in amplifier which measured the magnitude and phase of the detected signal. This change in the amplitude and phase was sent to the computer through a feed back loop which recorded the ultrasonic force

image. From this experiment we obtained both AFM and UFM images simultaneously. First, an AFM topographic image was obtained by engaging the tip with the sample, and then by switching on the thermal power and changing the frequency with constant amplitude of 1Vpp, UFM topographic images were obtained. Each sample was scanned starting initially from the notch and moving towards the region of interest where the crack growth had stopped, in order to determine the topographic changes across the sample surface.

CHAPTER 3

MATERIAL

3.1) Introduction

The material used for this study had a base-composition of Ni- 20wt. %Cr. This alloy base has commercial uses, with such trade-names as Chromel A, Nichrome V, and Tophet A. Ni- 20wt. %Cr is used in applications which can take advantage of its high electrical resistivity and heat-resistance, such as for furnaces and electrical heater wires. The features that lead to these applications are its high melting point, high electrical resistivity, reproducible temperature coefficient of resistance, good oxidation resistance and resistance to contamination. At elevated temperatures Ni- 20wt. %Cr exhibits good creep strength, high emissivity, low thermal expansion and low elastic modulus, good resistance to thermal shock, and ductility [16].

The samples for this study were miniature compact-tension samples that had been fractured under fatigue loading, as part of an investigation of crack growth as a function of grain size. Five different samples, with same base composition but with different grain sizes, were studied. The samples included:

- (1) Cryogenically milled and extruded Ni- 20wt. %Cr, where the fracture plane was the r-z plane of the extrusion, GE sample number 4-9-3;

- (2) Cryogenically milled and extruded Ni- 20wt. %Cr, where the fracture plane was the normal to the direction of the extrusion, GE sample number 4-9-12;
- (3) Cryogenically milled and extruded Ni- 20wt. %Cr + aluminum oxide, where the fracture plane was the plane of the extrusion, GE sample number 4-10-1;
- (4) Multiaxis forged Ni- 20wt. %Cr, GE sample number C-1
- (5) Commercial alloy MA754, a mechanically milled Ni- 20wt. %Cr + yttrium oxide, GE sample number 754-HT1.

These five samples were analyzed, and their surface topography was examined using different types of microscopes, such as white light interference microscope, scanning electron microscope, atomic force microscope, and ultrasonic force microscope. The instrumentation and experimental procedures were explained in the previous chapter. This chapter will discuss the general processes used to manufacture these sample-types.

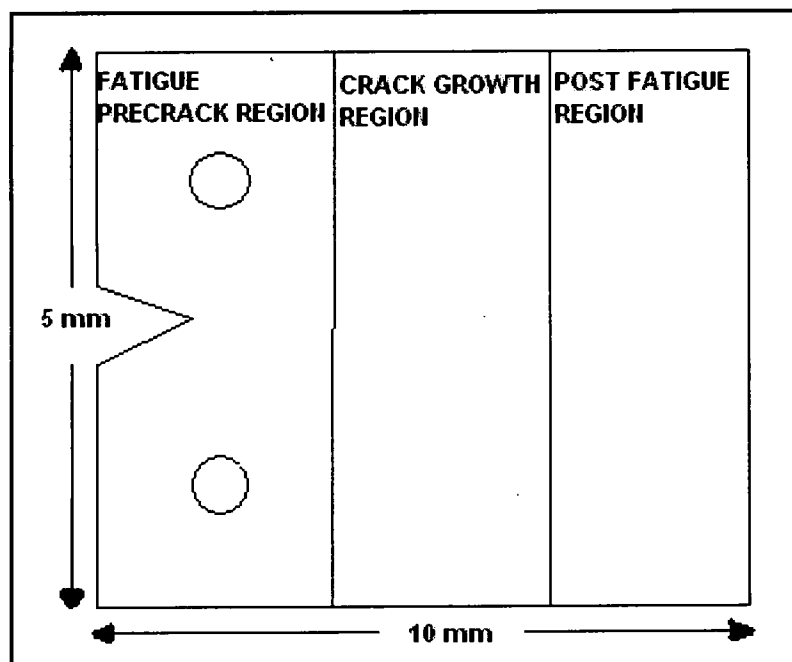


Figure3. 1: Compact tension sample

3.2) Cryogenically-milled Ni- 20wt. % Cr, crack oriented in r - z plane of extrusion

All the samples used in this study were of the same base-composition, but underwent different processing techniques, from cryogenic milling to conventional forging. The samples evaluated were tested miniature compact tension specimens of 10x5x5 mm dimension, *Figure 3.1*. The test procedure begins by creating a “pre-crack” at the notch in high-cycle fatigue. Then, the sample was cyclically deformed while crack length was measured. This propagation of crack is carried on gradually reduced stress-intensity, and the test is stopped when the crack-growth rate is quite small. After the test, the cracked surface is heated in air to “tint” it, in order to identify the crack grown region. Then the sample is pulled apart, to expose the crack surface. In this study was investigated the crack propagation and surface topography changes using different experimental techniques as discussed in the Chapter II.

The sample was basically divided into three different parts as shown in *Figure 3.2*, starting from notch as: 1- fatigue pre-crack region; 2- crack propagation region; 3- post-test fatigue. The area of study was region 2, where the crack propagated along the surface during the test.

All the samples were tested in a similar way. The fatigue fracture behavior of the Ni-20wt. % Cr samples is displayed as the change of crack growth rate with respect to stress intensity factor in a logarithmic plot which is shown in *Figure 3.3*.

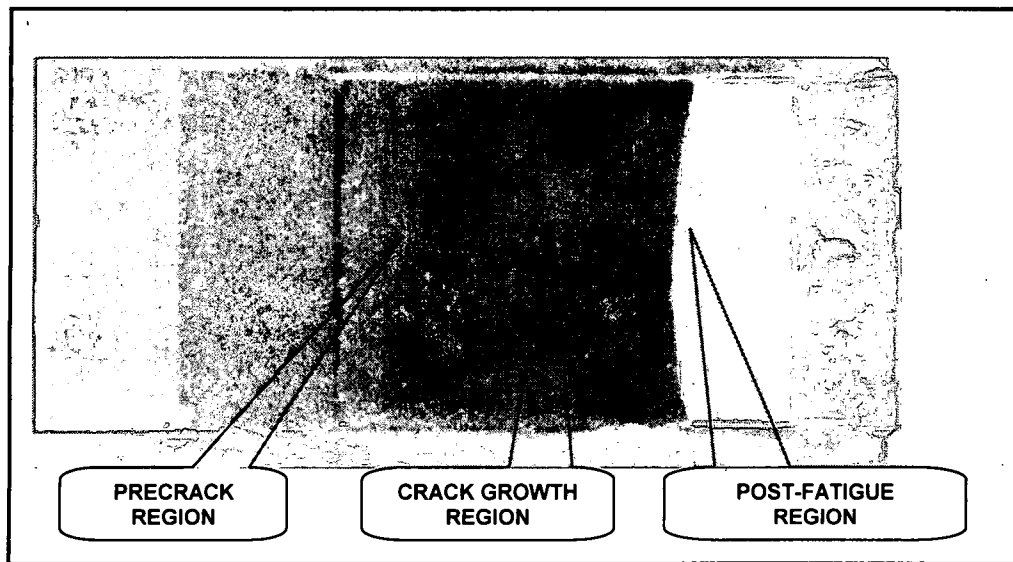


Figure 3.2: Fatigue fracture surface image of Ni-20wt.%Cr

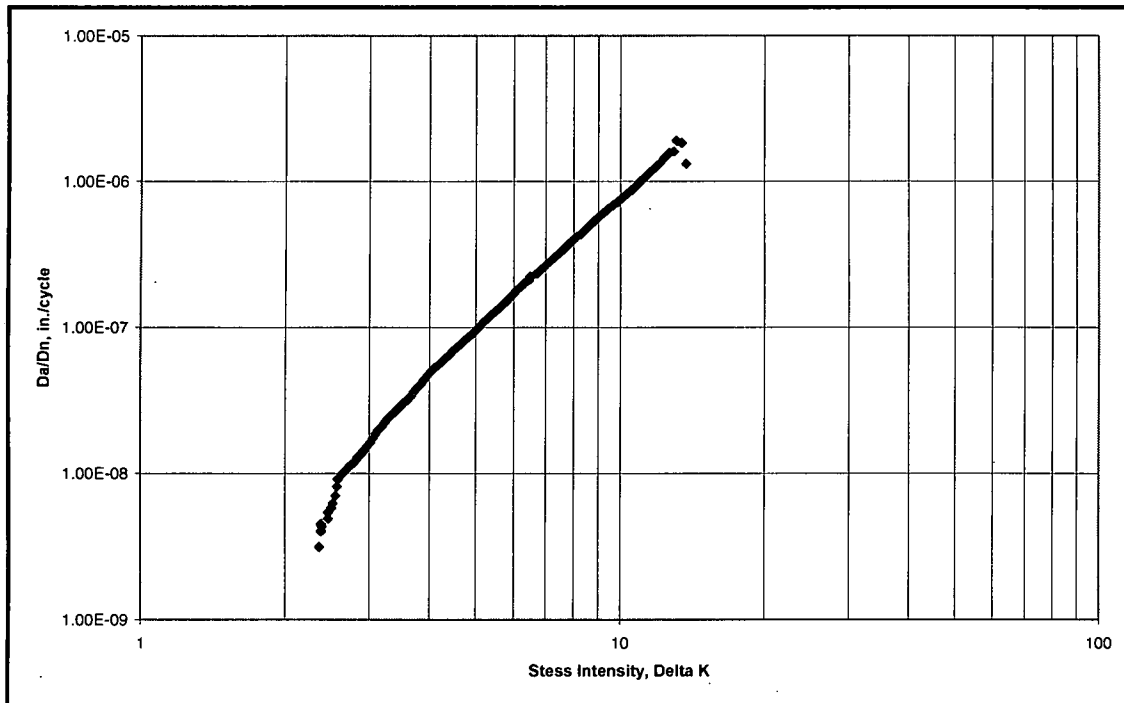


Figure 3.3: Plot between crack growth rate and stress intensity factor

3.3) Cryogenically milled Ni- 20wt. %Cr, with crack plane normal to the extrusion direction

Sample# 2 was cryogenically-milled Ni- 20wt. % Cr. It was milled under specified conditions. By performing the milling process, the strength of a material would be enhanced, and there would be decrease in the ductility. The grain size of the material which undergoes cryomilling could be very few nanometers. Cryomilling is basically a high energy mechanical milling process. Pre-alloyed and elemental powders are milled in cryogenic media, like liquid nitrogen. Ball milling is usually performed using hardened stainless steel balls at a ball powder ratio of about 20:1. As this ball milling is performed in the presence of liquid nitrogen at a temperature of -196°C , it is said to be cryomilling. Thus, the reaction between powders and nitrogen can lead to formation of ultrafine particles such as nitrides, oxides etc [18]. The fracture surface is shown in *Figure 3.4*. This sample consists of finest grains. A logarithmic plot of crack growth rate Vs stress intensity factor of cryomilled Ni- 20wt. %Cr is displayed in *Figure3.5*.

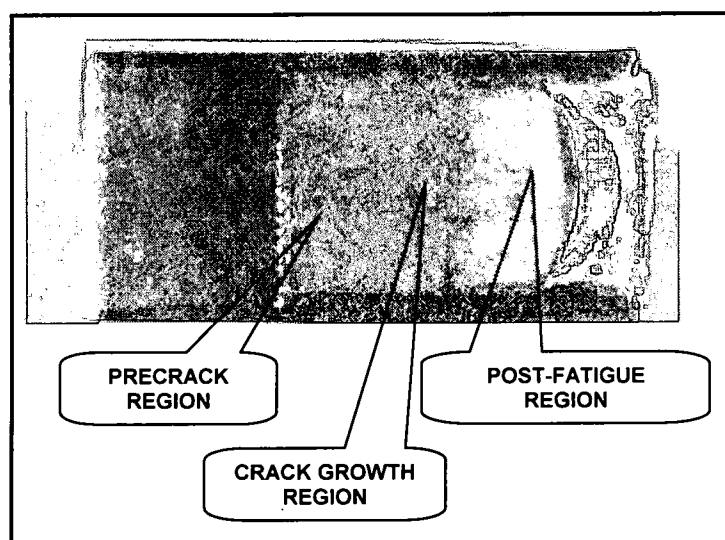


Figure3.4: Fatigue fracture surface image of cryogenically milled Ni-20wt.%Cr

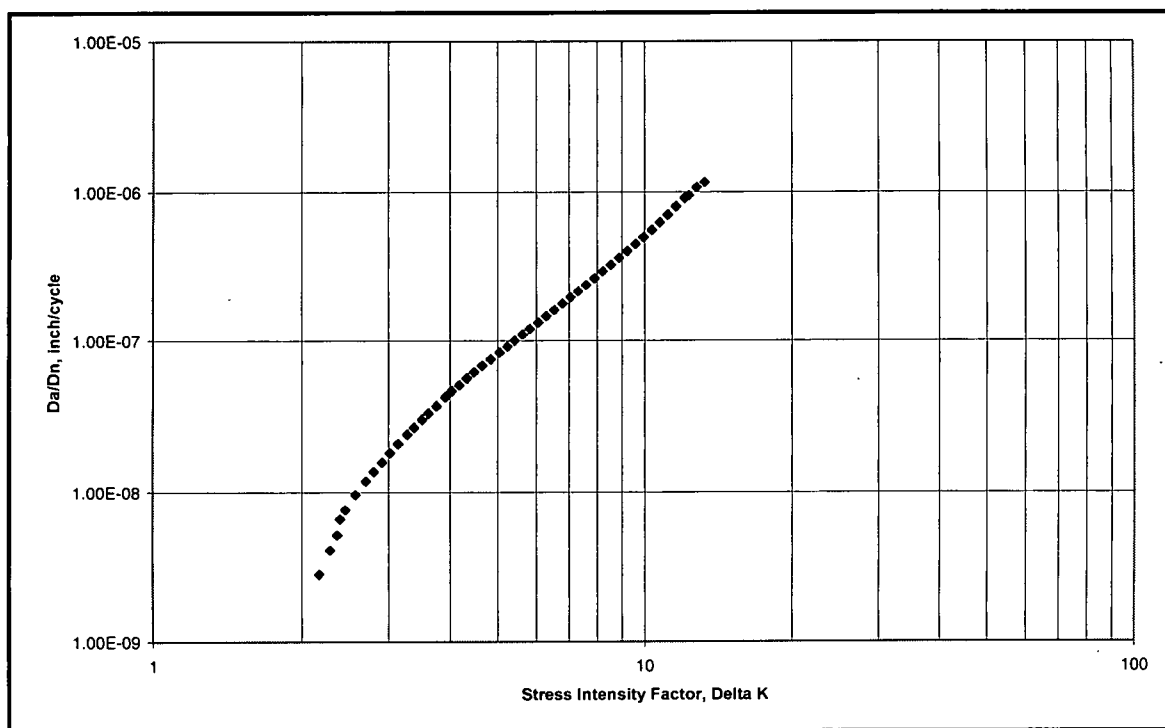


Figure 3.5: Plot between crack growth rate and stress intensity factor

3.4) Cryogenically milled Ni- 20wt. % Cr + Al₂O₃, with crack plane normal to the extrusion direction

Sample #3 is Ni- 20wt. % Cr + Al₂O₃. In this aluminum oxide particles were added during the milling of Ni- 20wt. % Cr sample and it was prepared in a similar way as discussed above. Al₂O₃ particles were clearly observed in SEM images. An optical image of the sample is shown in *Figure 3.6*. A logarithmic plot of crack growth rate vs. stress intensity factor of Ni- 20wt. % Cr + Al₂O₃ is shown in *Figure 3.7*.

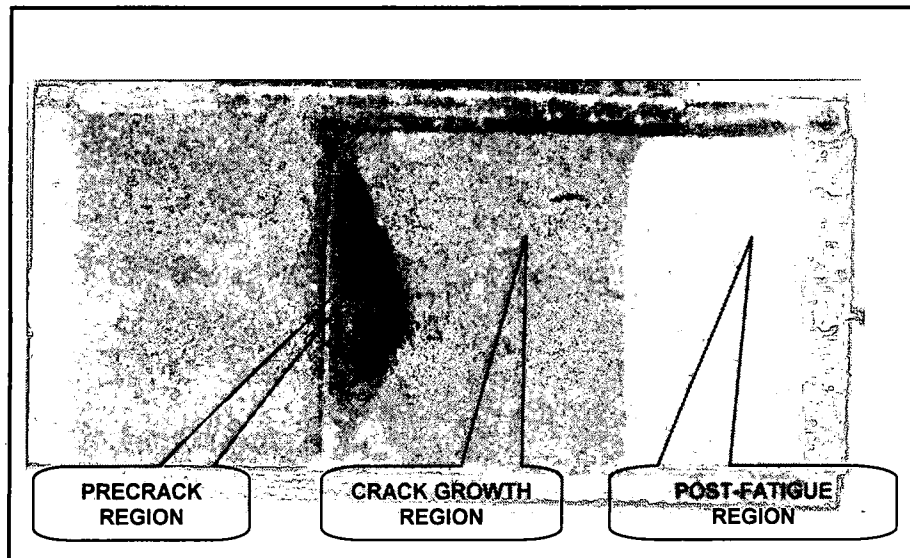


Figure 3.6: Fatigue fracture surface image of Ni-20wt.%Cr+Al₂O₃

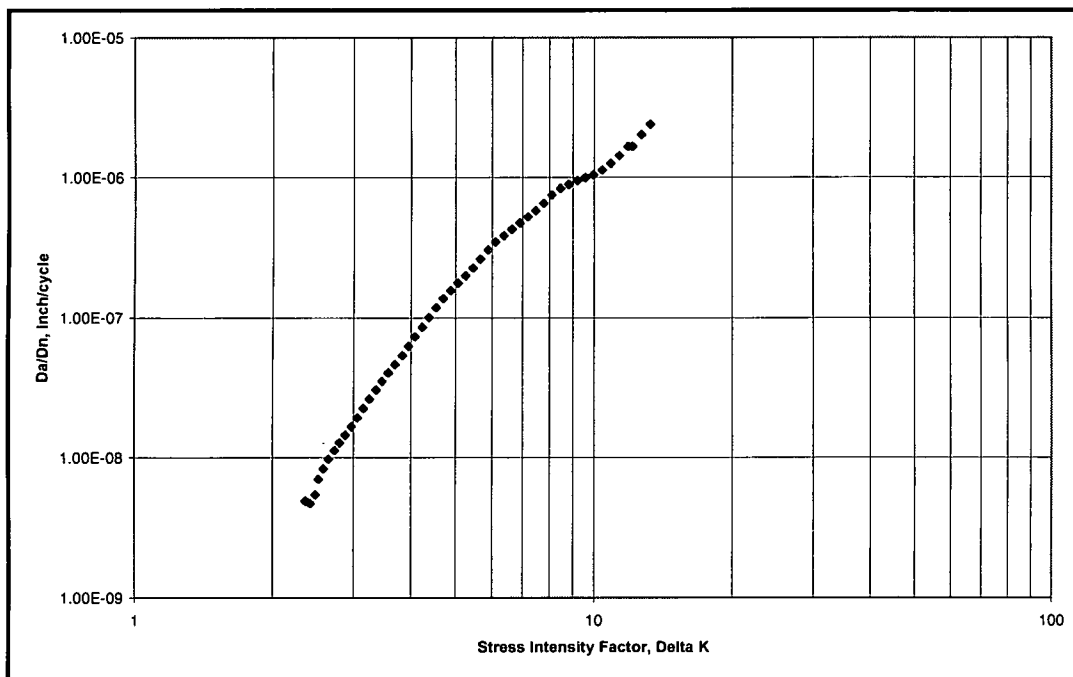


Figure 3.7: Plot between crack growth rate and stress intensity factor

3.5) Multi-axis forged Ni- 20wt. %Cr

Sample# 4 was “a-b-c” forged, that is, deformed in all three directions. Generally, forging is defined as shaping of metal by an impact or steady compression between dies. It is controlled plastic deformation of metals into useful shapes with desired mechanical properties.

There are three general types of forging processes; they are:

1. Impression die forging;
2. Cold forging and;
3. Open die forging.

Impression die forging

In this method, metal is pressed between two dies that contain a precut profile of the desired part shape. As the dies are brought closer together, the work piece undergoes plastic deformation until the enlarged sides touch the die's sidewall. During the forging process, flash is formed, as some of the deformed metal from the work piece flows outside the die impression. Parts from few ounces to 60,000 lbs can be made by closed-die forging.

Cold forging

This process is used when it is necessary to develop strength and hardness in the component, to have bright and clean finish and to eliminate forging scales and decarburization, *etc.* Components in this process are generally made from wrought bars or wire stocks by cold forging in closed dies.

Open die forging

In this process, metal is pressed between two flat dies with no precut profiles in the dies. Often, during open die forging, the work pieces are heated above the recrystallization temperature. Throughout the forging process, the work piece is moved so that all the aspects of the work piece may be forged. Thus, the movement of the work piece is the key to this method.

The a-b-c forged sample was produced by multiple open die forging at sequentially lower temperatures, resulting in a very fine recrystallized structure.

The forged sample fracture surface exhibited fine grains; all three different regions are indicated in *Figure 3.8*. Figure shows the logarithmic plot between crack growth rate and stress intensity factor *Figure 3.9*.

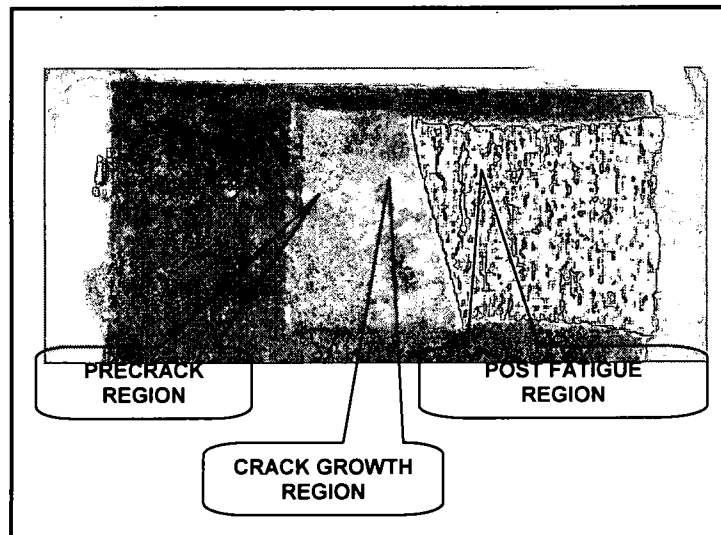


Figure 3.8: Fatigue fracture surface image of C1 Forged Ni-20wt.%Cr

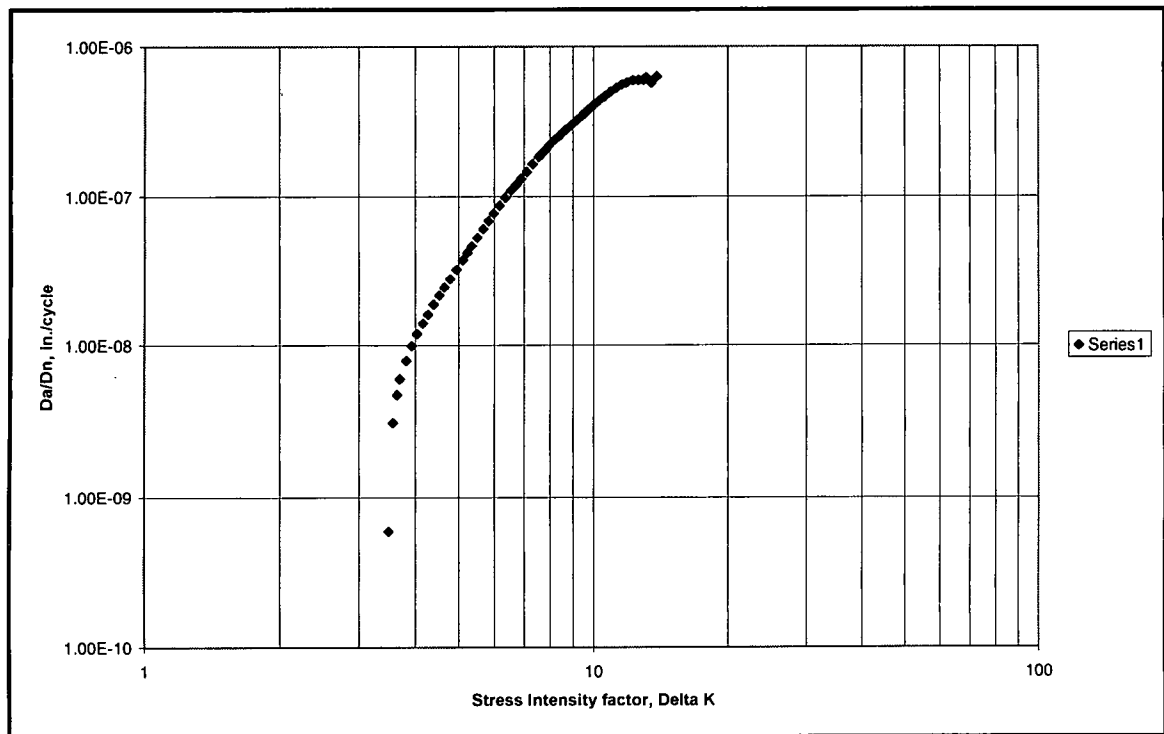


Figure 3.9: Plot between crack growth rate and stress intensity factor

3.6) MA754 HT

Sample #5 is MA754 which is an Inconel alloy. It is a Ni- 20wt. %Cr based, oxide dispersion strengthened alloy produced by powder metallurgy process. In this process, yttrium oxide dispersion (Y_2O_3) was introduced by mechanical alloying into the matrix. Due to the addition of Y_2O_3 in Ni- 20wt.%Cr matrix it exhibits excellent creep resistance at high temperature such as $1095^{\circ}C$ [21]. MA754 is mainly used in gas turbine engines because of its excellent mechanical properties obtained by thermo mechanical processing of the alloy. During this process, stable and recrystallized grain structure such as coarse and highly elongated grains is obtained. MA754 is a high strength alloy with micro structurally stable and it also consists of a high melting point. Main applications of MA754 are in fixtures, skid rails and fasteners etc.

The MA754 fatigue sample regions are indicated in *Figure 3.10*. The sample mostly consists of elongated grains. *Figure 3.11* shows the logarithmic plot between crack growth rate and stress intensity factor for MA754HT material.

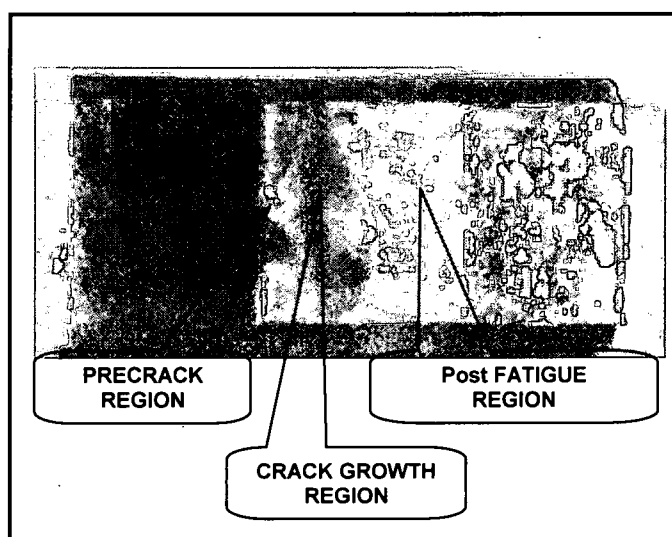


Figure 3.10: Fatigue fracture surface image of MA 754HT

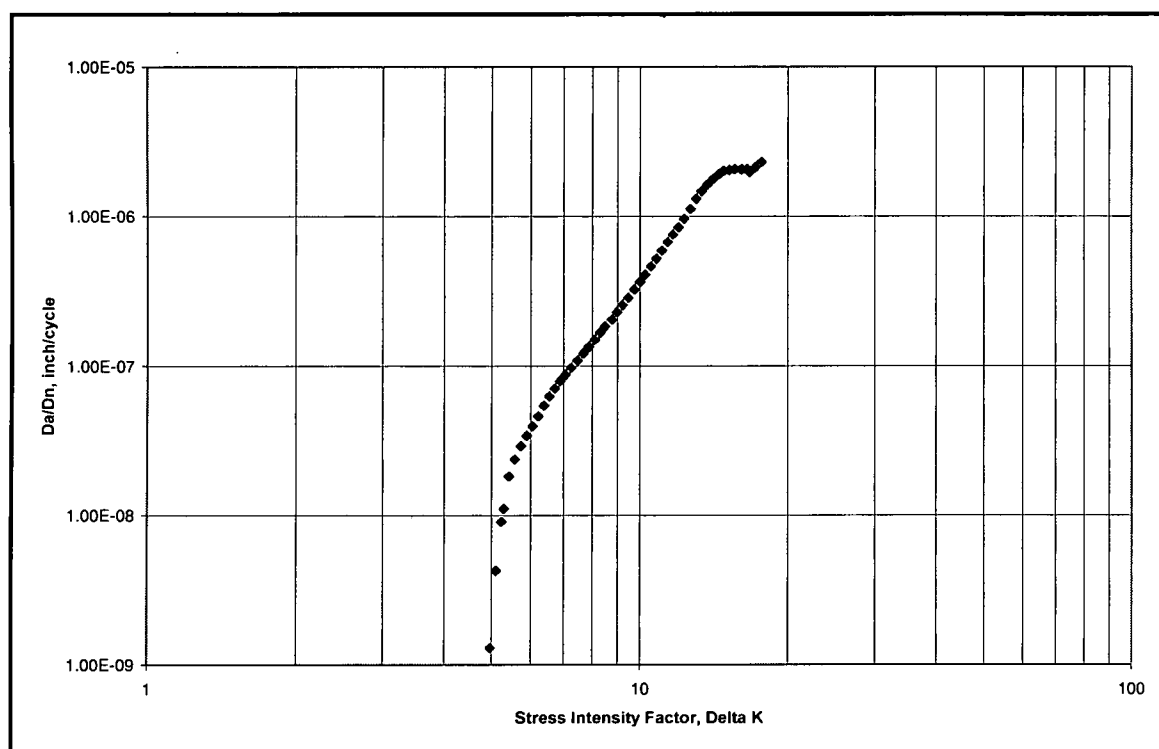


Figure 3.11: Plot between crack growth rate and stress intensity factor

CHAPTER 4

FATIGUE FRACTURE ANALYSIS USING WHITE LIGHT INTERFERENCE MICROSCOPE

4.1) Introduction

Fatigue of materials produces rough fracture surfaces. This roughness is a direct result of the crack propagation. The roughness mainly depends on the microstructural characteristics of a material, stress conditions, micro-mechanisms of deformation in the region around the crack tip. Basically, roughness originates from nucleation and growth of microcracks, produced by the high stress fields around the growing crack. These microcracks link up together and join the main crack. At high cyclic stresses and for conditions where there is microcracking ahead of the growing crack tip, there is a large damage zone ahead of the crack. Because the extent of out-of-plane crack nucleation has increased, the surface becomes rougher. In the case of plastic deformation, the repeated cyclic straining of materials produces net slip bands on different glide planes. The irreversibility of shear displacements along the slip bands results in roughening of surface. Thus the surface roughness can be defined as the measure of fine, closely spaced and random irregularities of the surface texture caused by propagation of the crack and it is represented by a parameter R_q .

Many different parameters play an important role in fracture analysis. Microscopically these rough surfaces appear as hills and valleys. These valleys act as micronotches and the stress concentration at these valleys promotes crack growth rate. Recently [1] crack growth rate in a fracture material has been inferred using surface roughness analysis. In these measurements, the fracture occurred naturally and the conditions were not clearly known. In the work reported herein, the relation between crack growth rate and the surface roughness used specimens fractured under controlled and known conditions.

Measurement of fracture surface topography can be performed by determining the height Z in a plane. Experimentally this can be achieved by measuring the surface roughness. Usually the surface roughness can be measured by wide range of commercial instruments such as contact profilometry, laser profilometry, AFM and STM. For fracture surfaces scanning probe instruments has there limitations as this instrument involves raster scanning, tip damage can be possible when the roughness is very high (such as hills) and the resolution in the y-direction depends on the shape and dimensions of the probe. The spacing of profile is limited in this instrument. In white light interference microscope the mechanical stylus is replaced by a fine white light source, so that a constant distance is maintained from the reference surface. Surface topography is determined from the changes in the path length of the light reflected from the surface. This system computes several surface parameters that provide information about roughness and surface profile. The surface profile is most useful tool for examining surface texture and also provides a visual sense of the surface. For the measurement of fatigue fracture surfaces, vertical scanning interferometry (VSI) is used as it is most effective for rough surfaces. As this a non contact profilometer, the fatigue fracture

materials can be easily measured without damaging the lens and it doesn't require any sample preparation. The surface roughness values are obtained with its 3D topographical images.

The fatigue fracture surfaces of five Ni-20Cr samples were examined using white light interference microscope for surface roughness values. The samples were fatigue fractured under a controlled crack growth rate where the crack growth rate gradually decreases from a fatigue precrack region to post-test fatigue region and the crack growth is completely terminated at a room temperature. The analysis of surface roughness is performed on 10x5x5 mm samples starting from the notch till the post fatigue region where the crack growth rate decreases.

All the images are taken, starting from the notch and moving towards the post fatigue region where the crack has terminated. Surface topographical changes are observed with respect to surface roughness value and crack growth rate using white light interferometer. The samples were:

- (1) Cryogenically milled and extruded Ni- 20wt. %Cr, with crack plane in the r-z plane of the extrusion, sample number 4-9-3.
- (2) Cryogenically milled and extruded Ni- 20wt. %Cr, with crack plane in the basal plane of the extrusion (that is, normal to the extrusion direction, sample number 4-9-12).
- (3) Cryogenically milled and extruded Ni- 20wt. %Cr + Al₂O₃, with crack plane in the r-z plane of the extrusion, sample number 4-10-1.
- (4) Multi-axis forged Ni- 20wt. %Cr, sample number C1.

(5) Commercial alloy MA754, a Ni- 20wt. %Cr + Y₂O₃ alloy, produced by mechanical alloying and extrusion. The crack plane was oriented in the basal plane of the extrusion (that is, normal to the extrusion direction).

4.2) Results:

Sample# 1 Cryogenically milled and extruded Ni- 20wt. %Cr, with crack plane in the r-z plane of the extrusion, sample number 4-9-3.

Images are taken from the position 1 through 9 on the sample as shown in *Figure 4.1*. All the images as shown in the figure are taken at 20X magnification across the sample. The distance between first position and the second position is 0.63mm. Surface topographical changes and 3D images for the positions 1 through 9 are clearly shown in *Table 4.1*. The images were analyzed using a software package specific to the white light interference microscope. The results for each image is shown in *Table 4.2*, and also plotted in the *Figure 4.3* as function of distance. The surface roughness values are decreasing from position 1 through position 9 with respect to crack growth rate.

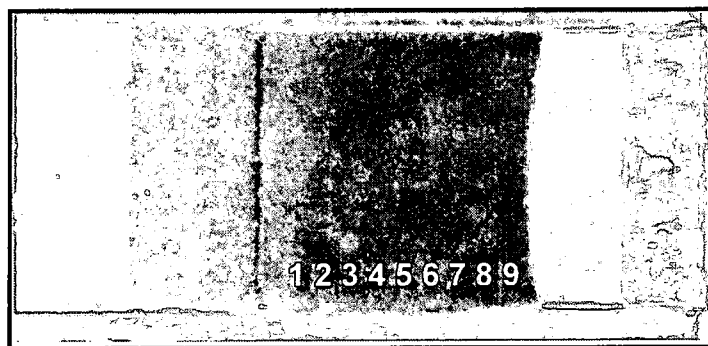
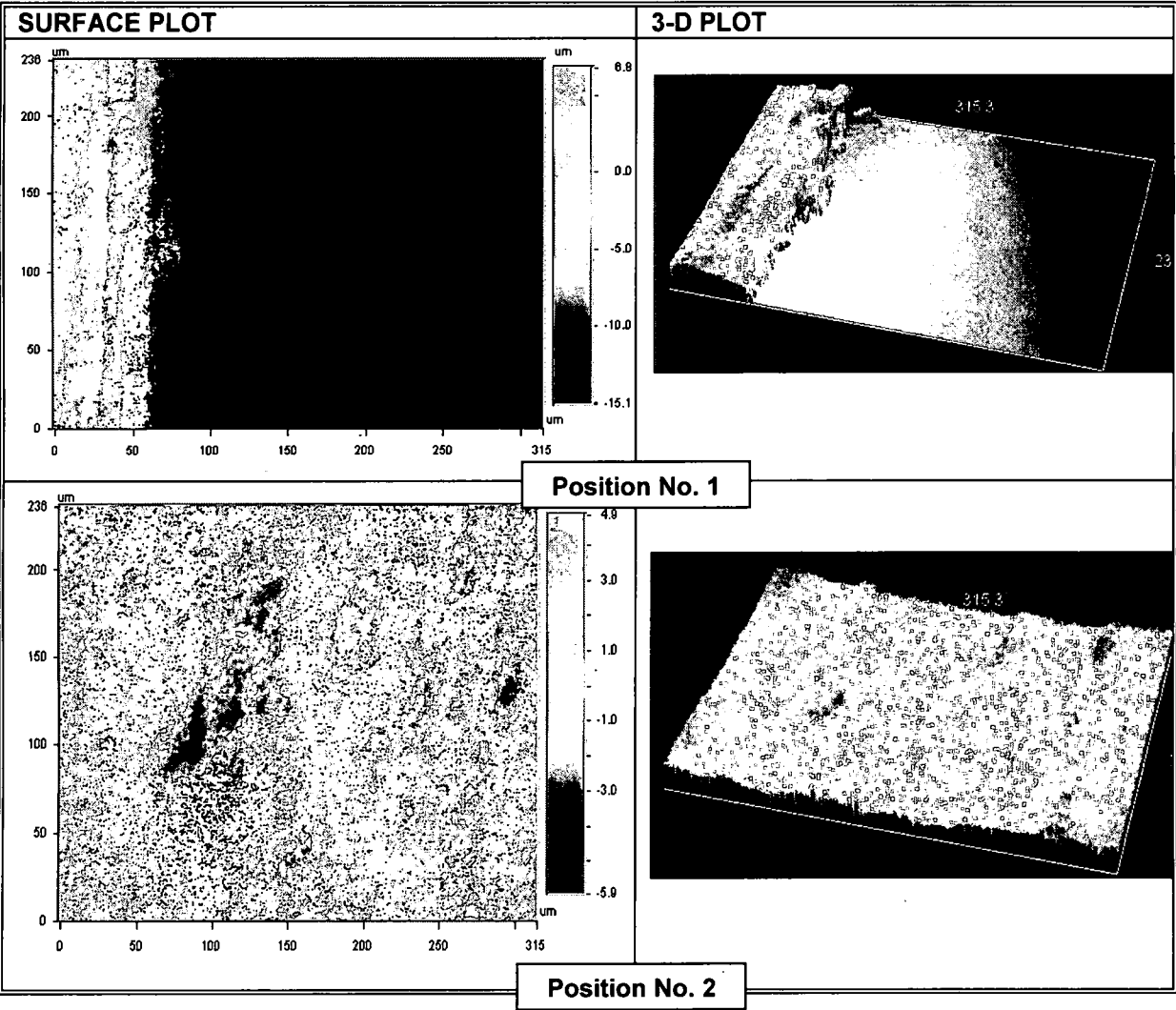
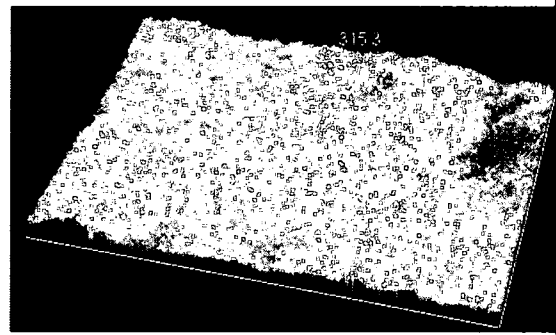
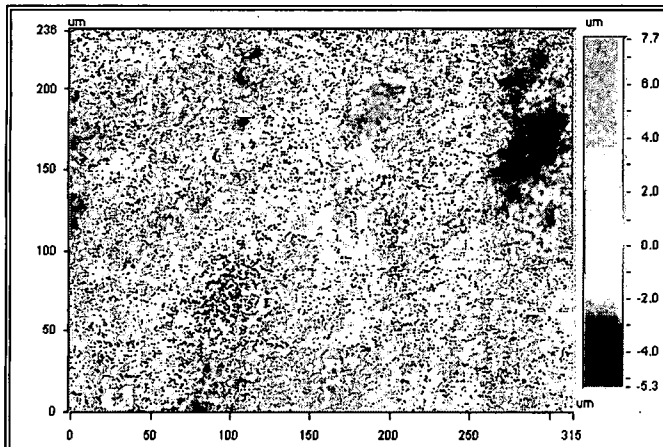


Figure 4.1: Optical image of Ni-20wt.%Cr

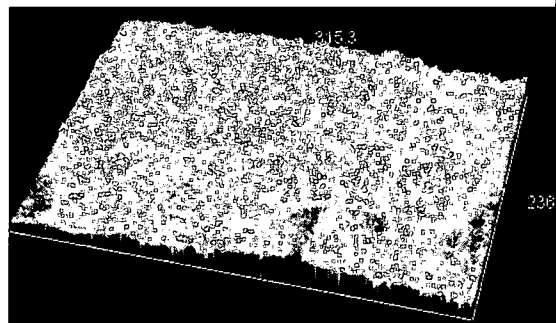
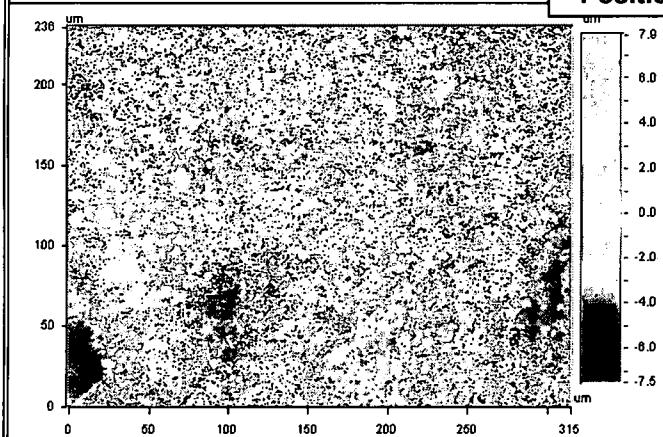
Table 4.1: Surface and 3D images of sample#1 are taken from White Light Interference

Microscope

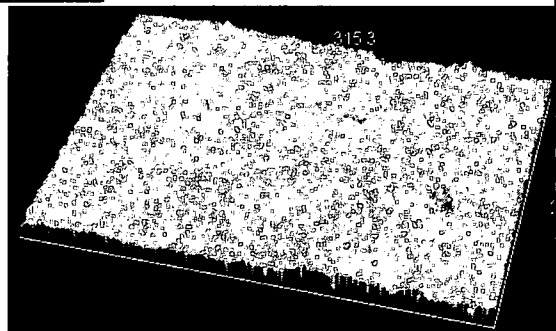
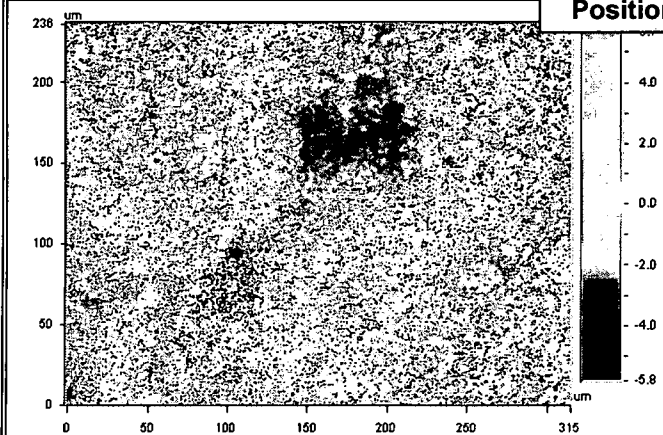




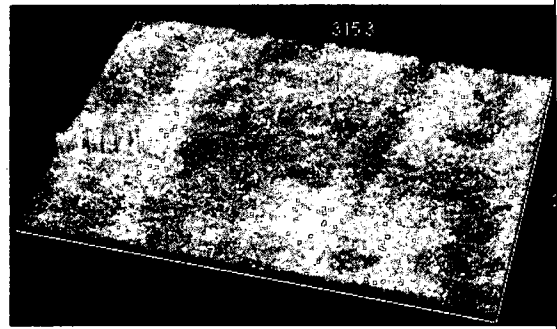
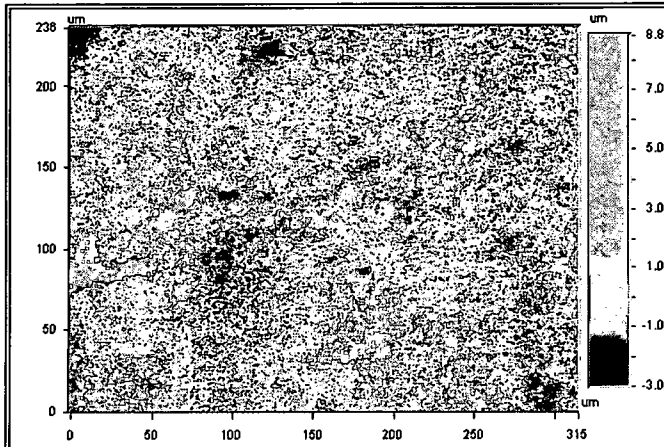
Position No. 3



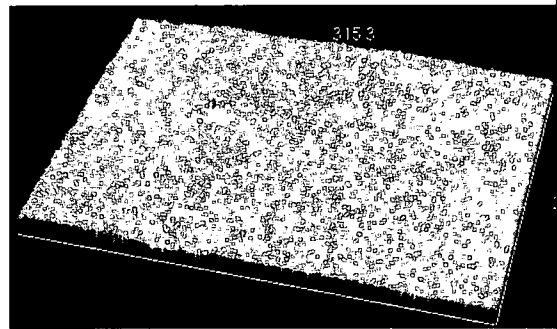
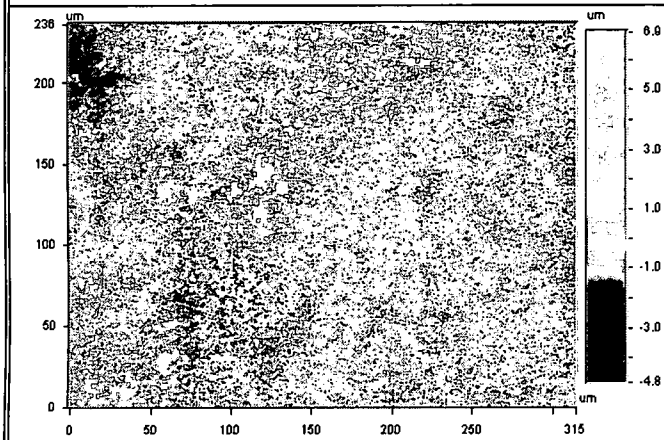
Position No. 4



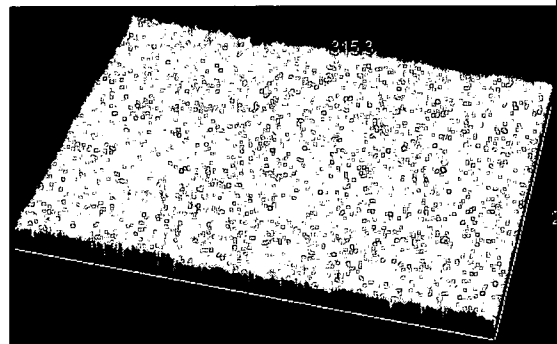
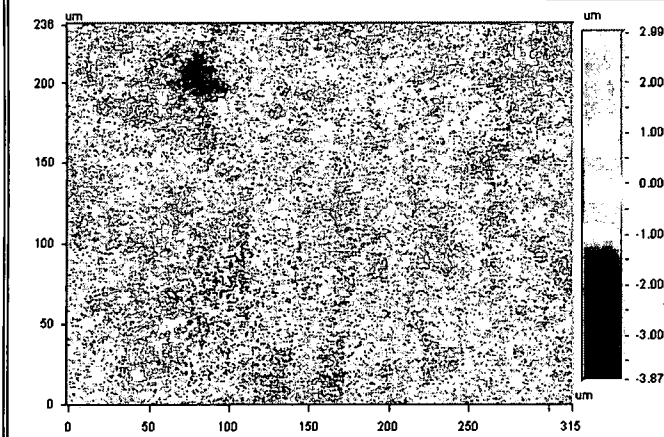
Position No. 5



Position No. 6



Position No. 7



Position No. 8

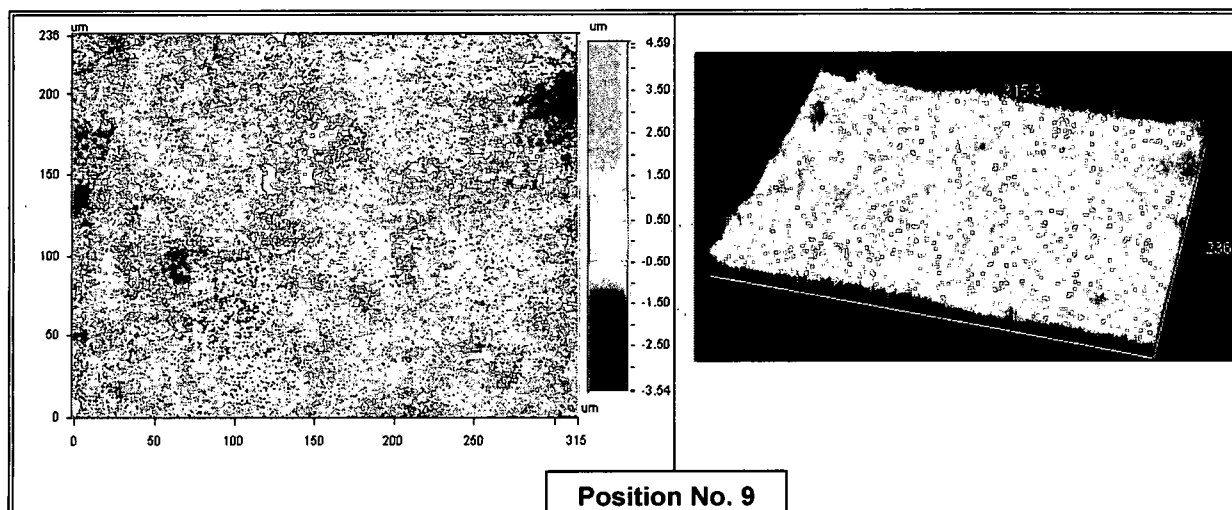


Table 4.2: Surface Roughness measurements of sample #1 with respect to crack length

Distance(mm)	0.63	1.26	1.89	2.52	3.15	3.78	4.41	5.04	5.67
R _q (μm)	2.60	1.25	1.42	1.80	1.21	0.782	0.649	0.497	0.688

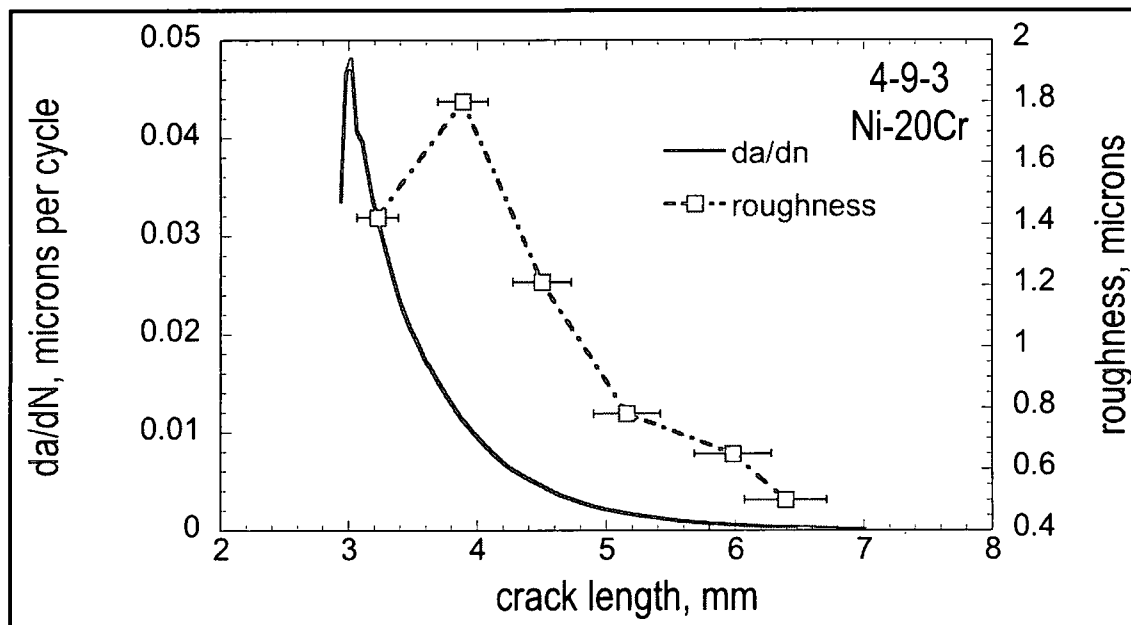


Figure 4.2: Graph plotted between crack length, crack growth rate and surface roughness

Sample#2 Cryogenically milled and extruded Ni- 20wt.%Cr, with crack plane in the basal plane of the extrusion (that is, normal to the extrusion direction, sample number 4-9-12.

In this sample images are taken from position 1 through 6 starting from notch through post fatigue region as shown in *Figure 4.3*. All the images are taken at 20X magnification approximately starting at the center of the sample. Surface topographical changes and there 3D images for positions 1 through 6 are clearly shown in *Table 4.3*. The surface roughness value of sample is very less compared with other samples. The results for each image is shown in *Table 4.4*, and also plotted in the *Figure4.4* as function of distance. The *Table4.4* shows that in fatigue pre crack region the R_q is high and gradually decreases as the low crack region is approached.

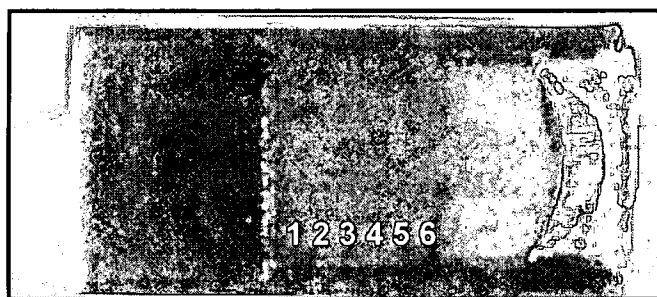
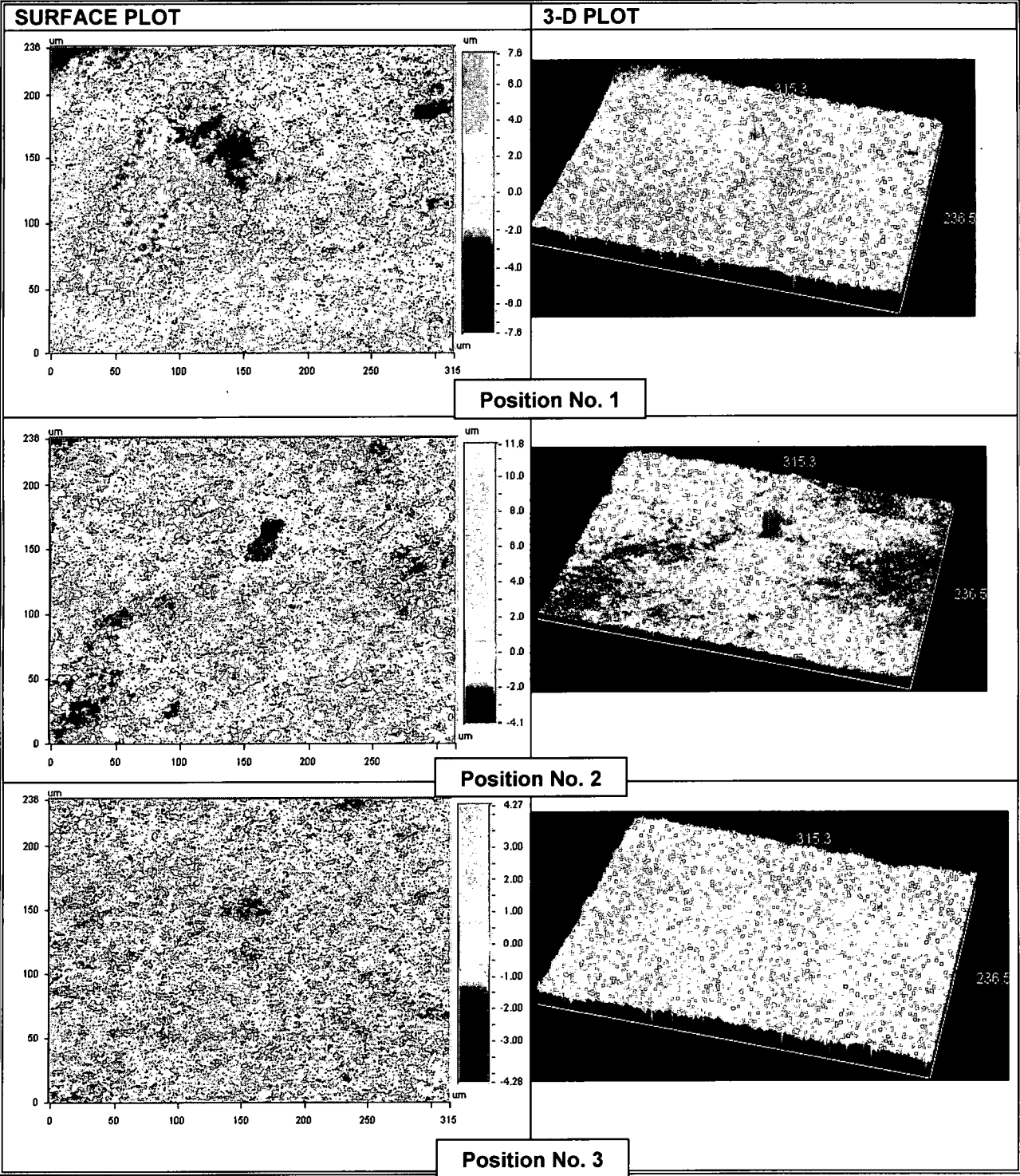


Figure4.3: Optical image of Cryomilled Ni-20wt.%Cr

Table 4.3: Surface and 3D images of sample# 2 taken from White Light Interference Microscope



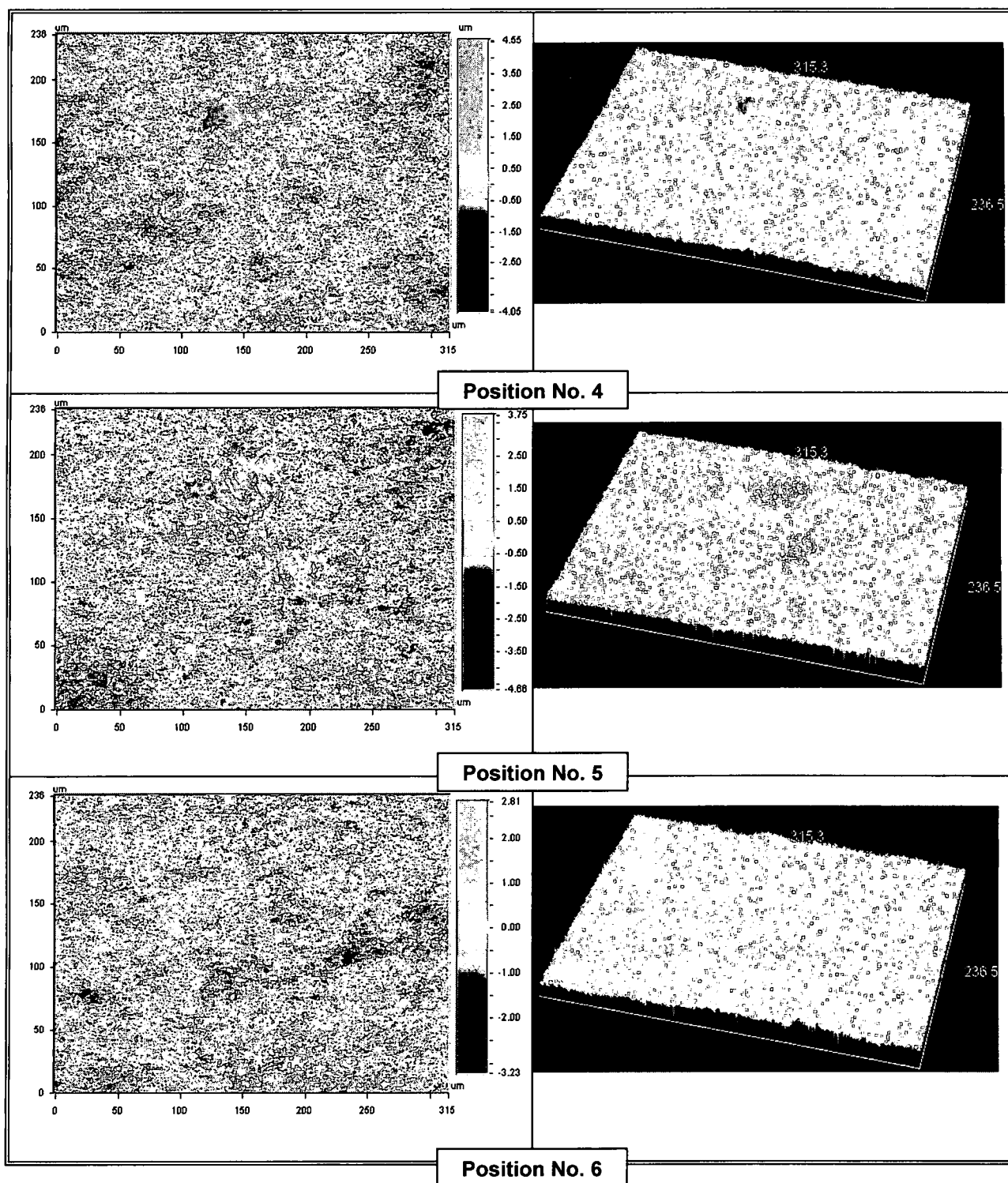


Table 4.4: Surface Roughness measurements of sample# 2 with respect to crack length

Distance(mm)	0.63	1.26	1.89	2.52	3.15	3.78
R _q (μm)	1.36	1.03	0.6196	0.473	0.457	0.430

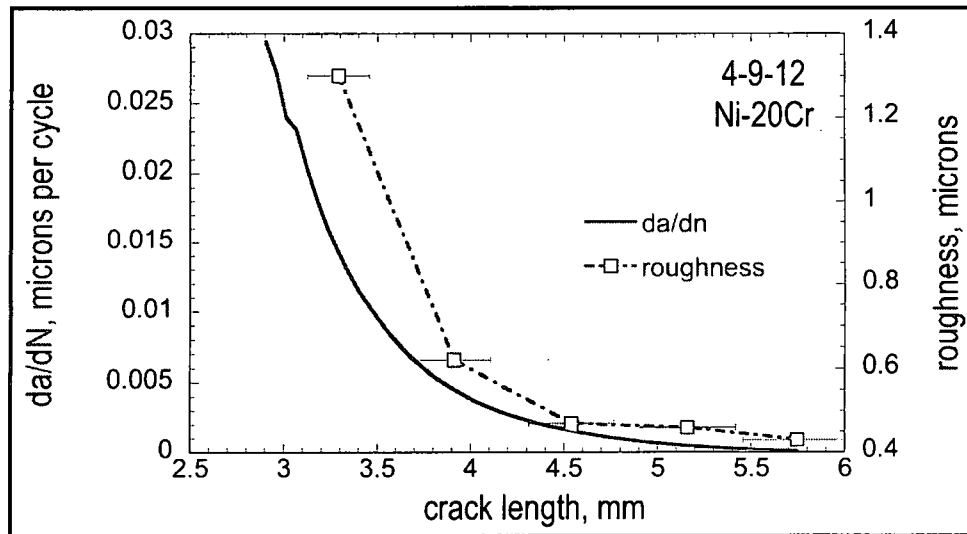


Figure 4.4: Graph plotted between crack length, crack growth rate and surface roughness

Sample # 3 Cryogenically milled and extruded Ni- 20wt. %Cr + Al₂O₃, with crack plane in the r-z plane of the extrusion, sample number 4-10-1.

Images are taken from position 1 through 8 starting from the notch at the center and moving towards the post fatigue region as shown in the *Figure 4.5*. All the images are taken at 20 X magnification. Surface topographical changes and their 3D images for positions 1 through 8 are clearly shown in *Table 4.5*. The results for each image is shown in *Table 4.6*, and also plotted in the *Figure 4.6* as function of distance. The surface roughness values are decreasing from position 1 through position 8 with respect to crack growth rate.

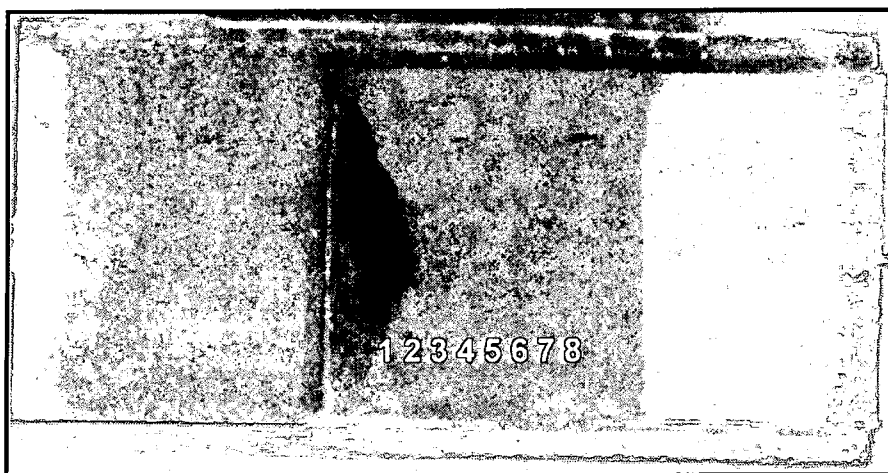
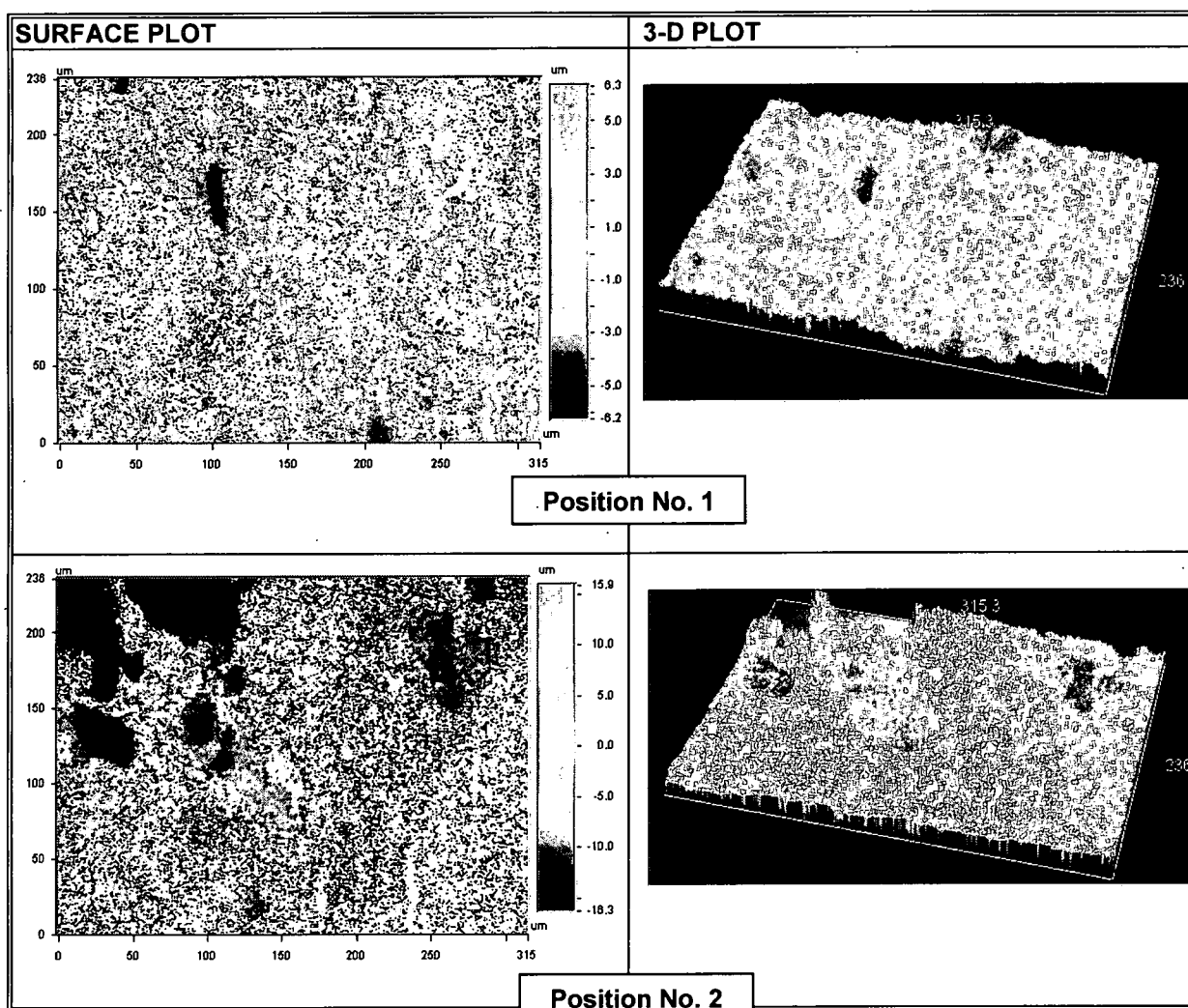
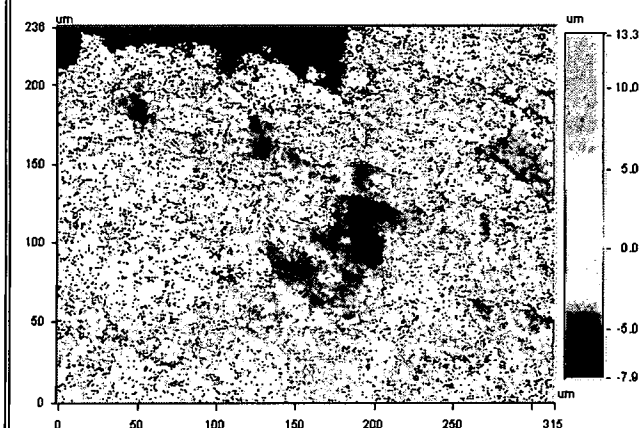


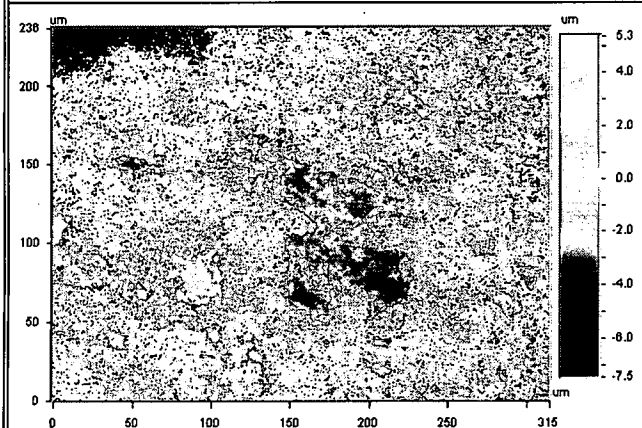
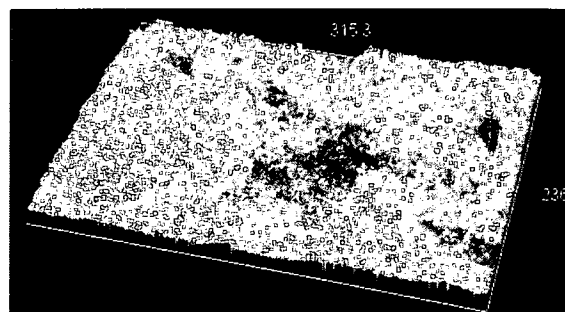
Figure 4.5: Optical image of Ni-20wt.%Cr+Al₂O₃

Table 5: Surface and 3D images of sample# 3 are taken from White Light Interference Microscope

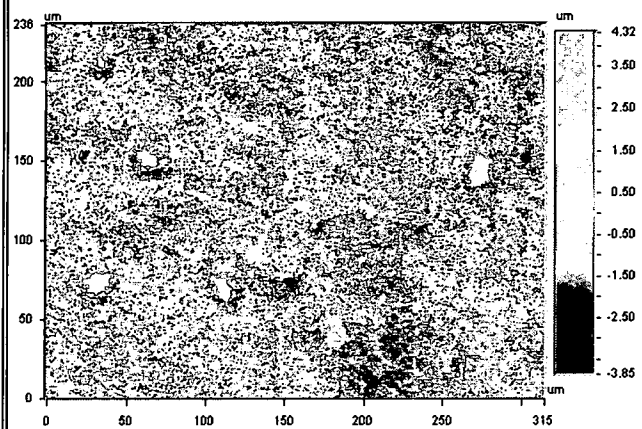
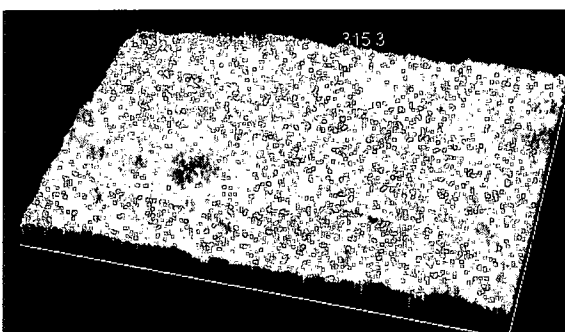




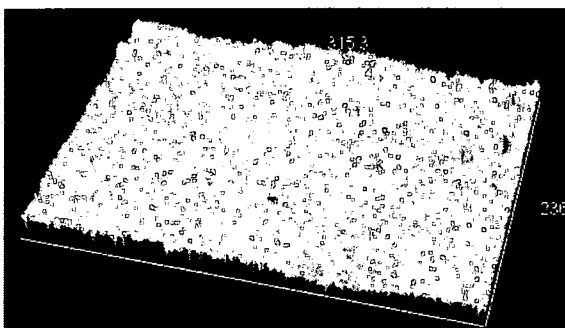
Position No. 3

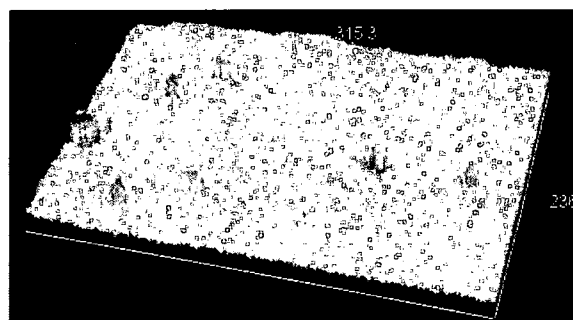
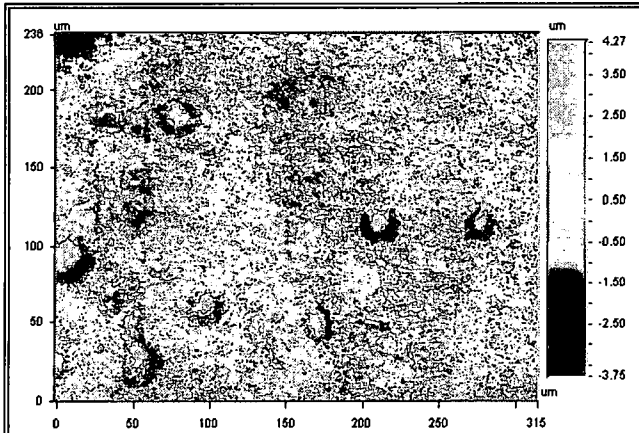


Position No. 4

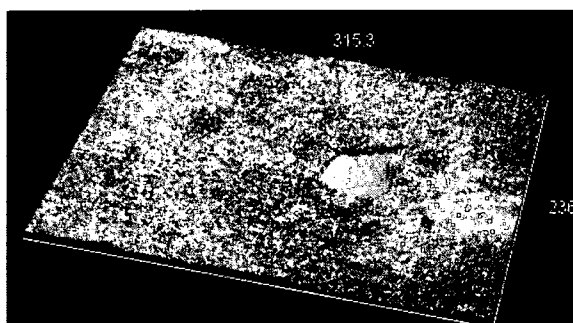
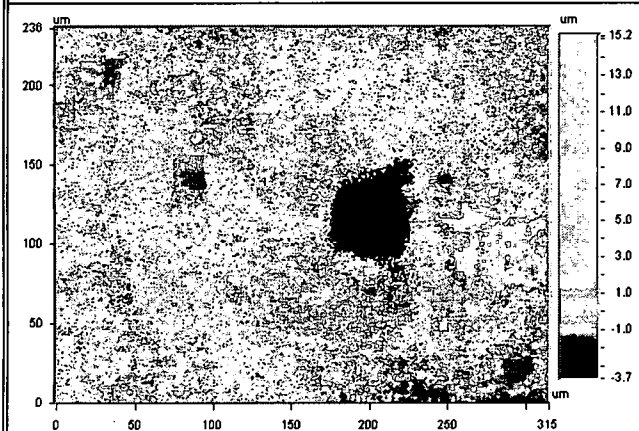


Position No. 5

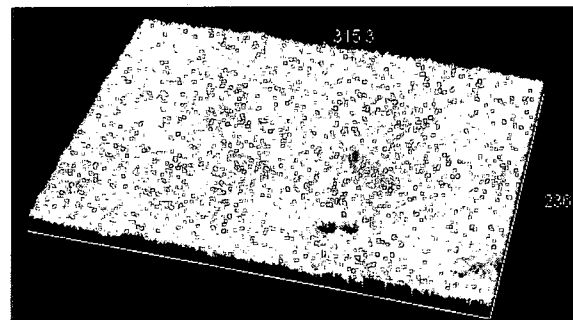
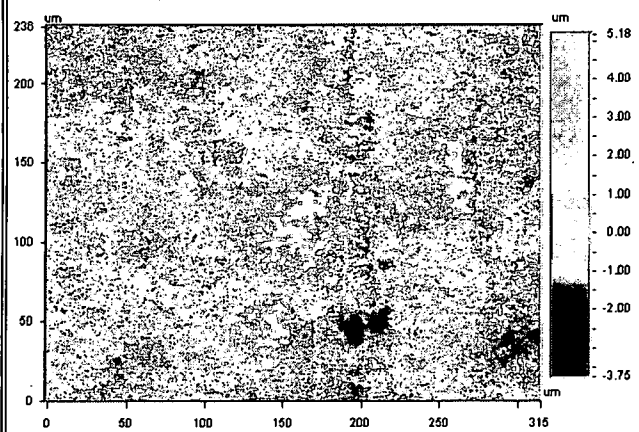




Position No. 6



Position No. 7



Position No. 8

Table 4.6: Surface Roughness measurements with respect to crack length

Distance(mm)	0.63	1.26	1.89	2.52	3.15	3.78	4.41	5.04
R _q (μm)	1.67	4.98	2.37	1.36	0.863	0.769	0.706	0.691

Sample # 4 Multi-axis forged Ni- 20wt. %Cr, sample number C1.

Images are taken from position 1 through 5 as shown in *Figure 4.7*. Surface topographical changes and there 3D images for positions 1 though 5 are clearly shown in *Table 4.7*.The results for each image is shown in *Table 8*, and also plotted in the *Figure 4.8* as function of distance. The surface roughness values are decreasing from position 1 through position 5 with respect to crack growth rate.

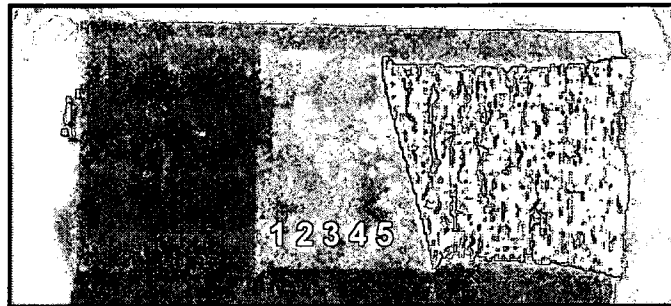
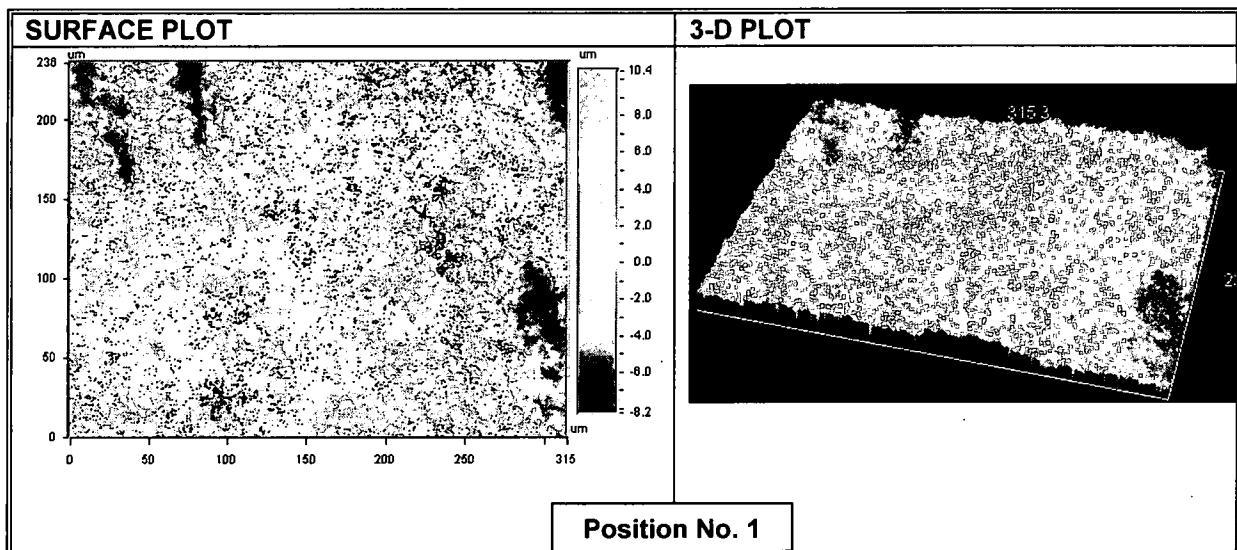
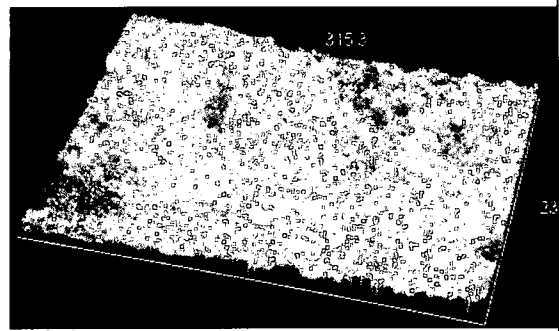
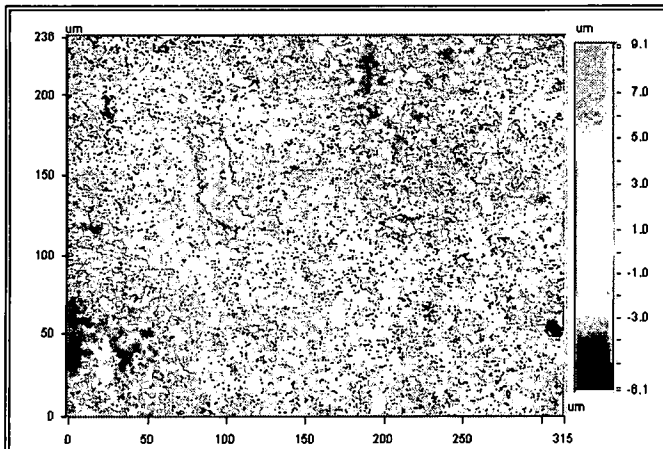


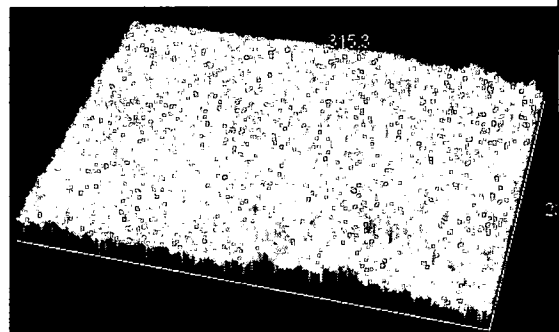
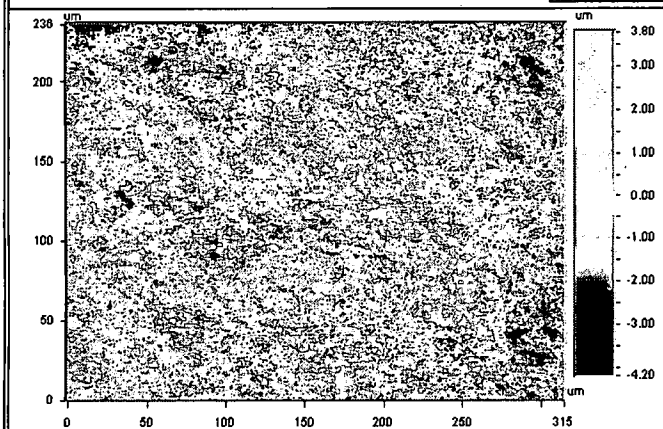
Figure 4.7: Optical image of C1-Forged Ni-20wt.%Cr

Table 4.7: Surface and 3D images of sample# 4 are taken from White Light Interference Microscope

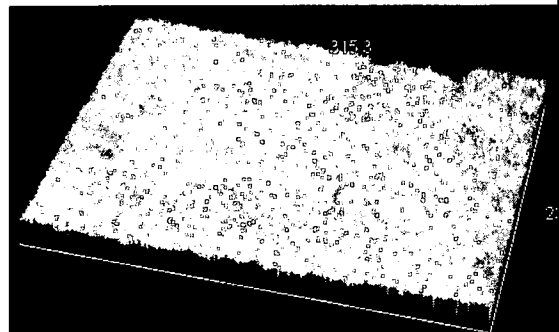
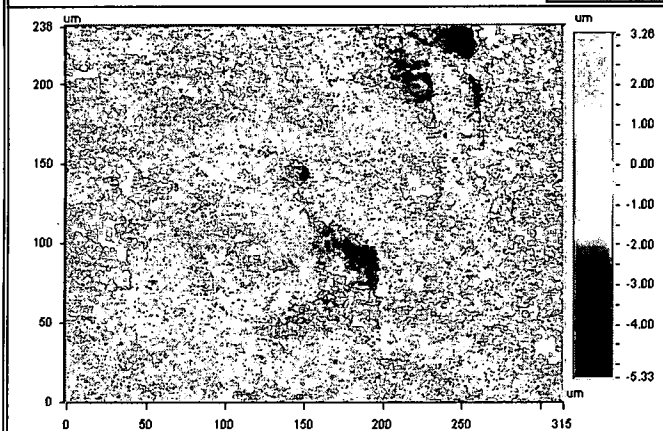




Position No. 2



Position No. 3



Position No. 4

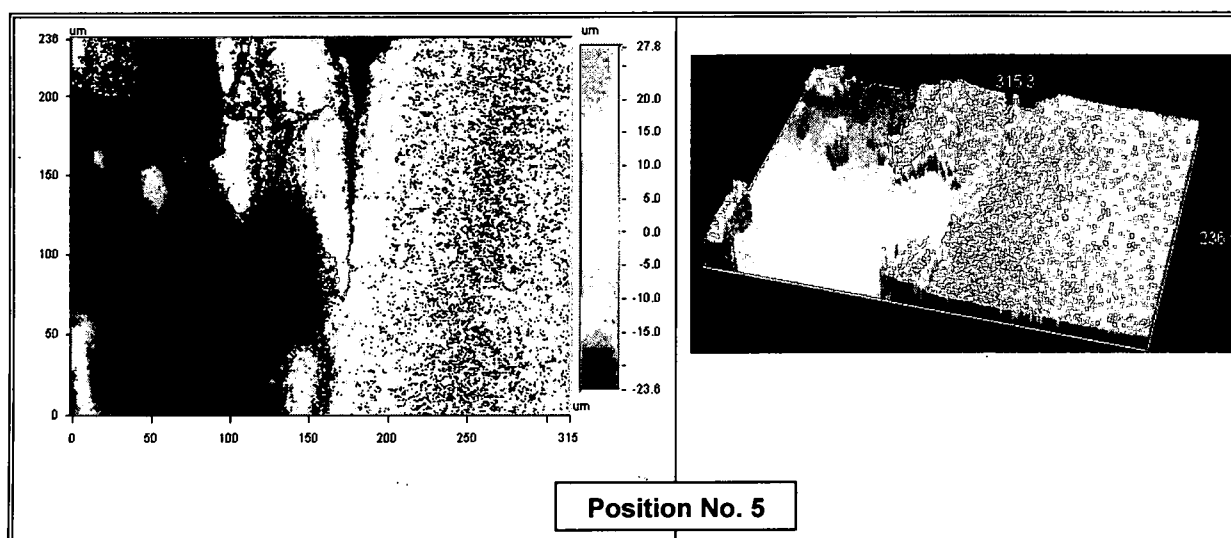


Table 4.8: Surface Roughness measurements with respect to crack length

Distance(mm)	0.63	1.26	1.89	2.52	3.15
$R_q(\mu\text{m})$	2.63	1.85	0.892	0.832	0.706

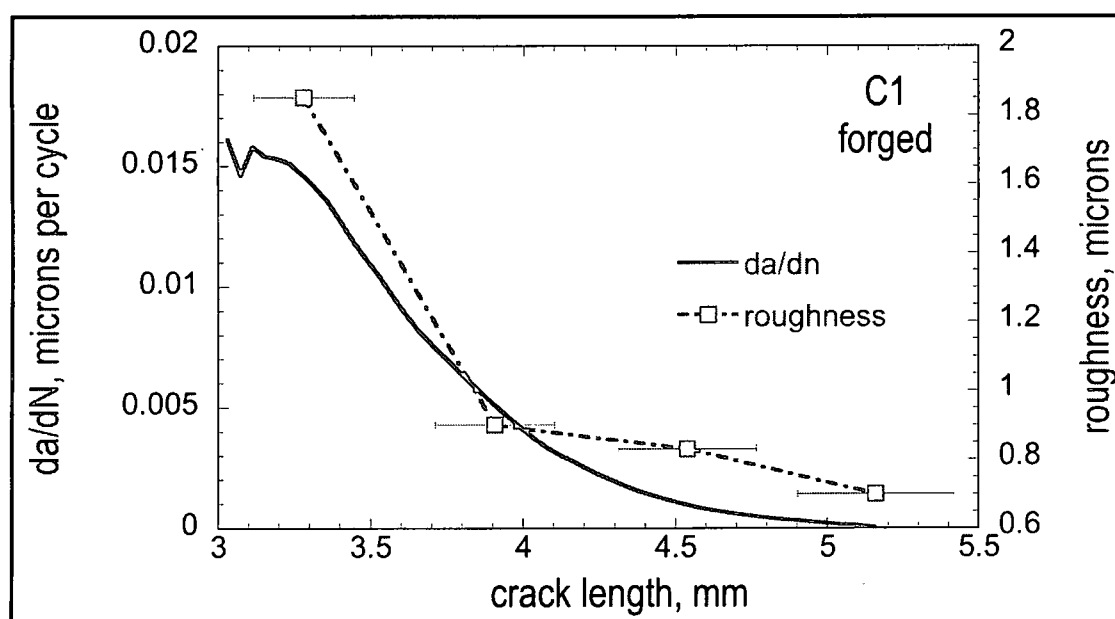


Figure 4.8: Graph plotted between crack length, crack growth rate and surface roughness

Sample # 5 Commercial alloy MA754, a Ni- 20wt.%Cr + Y₂O₃ alloy, produced by mechanical alloying and extrusion, with the crack plane oriented in the basal plane of the extrusion (that is, normal to the extrusion direction).

Images are taken from position 1 through 9 as shown *Figure 4.9*. All the images are taken starting from the notch towards the post fatigue region at 20X magnification as in *Table 4.9*. The surface of MA754 is very rough and we observe clearly the striation pattern on the images. The surface roughness values are not uniform in this material and posses high values of roughness. The results for each image is shown in *Table 4.10*, and also plotted in the *Figure 4.10* as function of distance. There no proportional relation between crack growth rate and surface roughness values in the MA754.

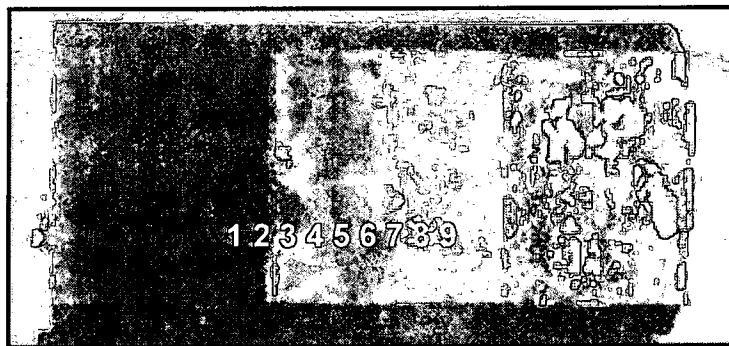
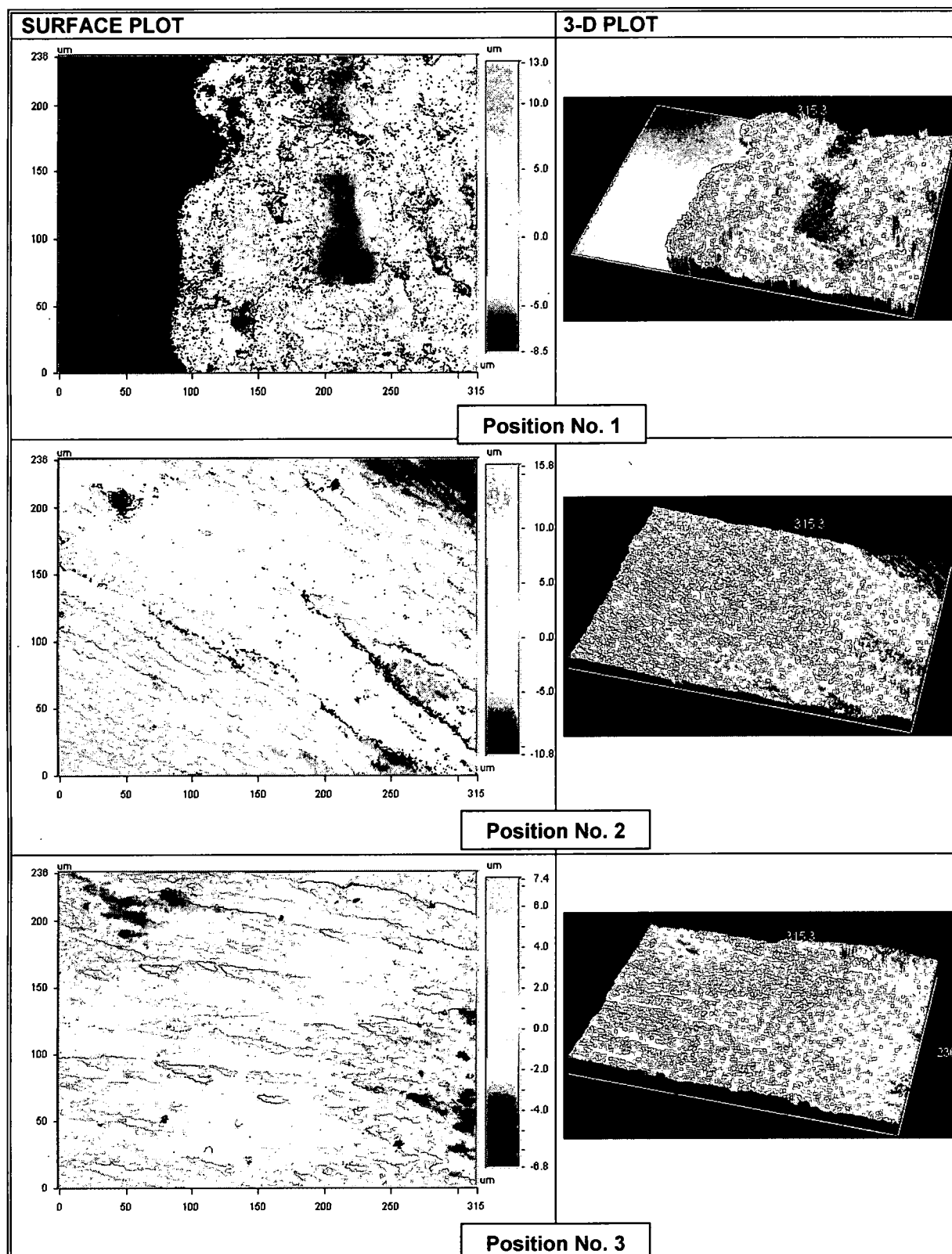
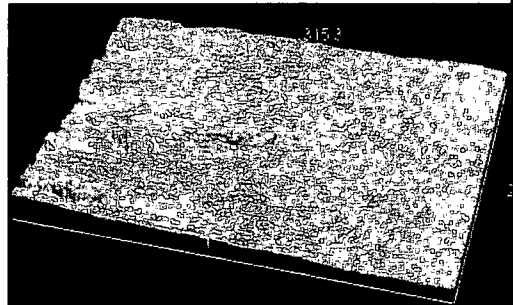
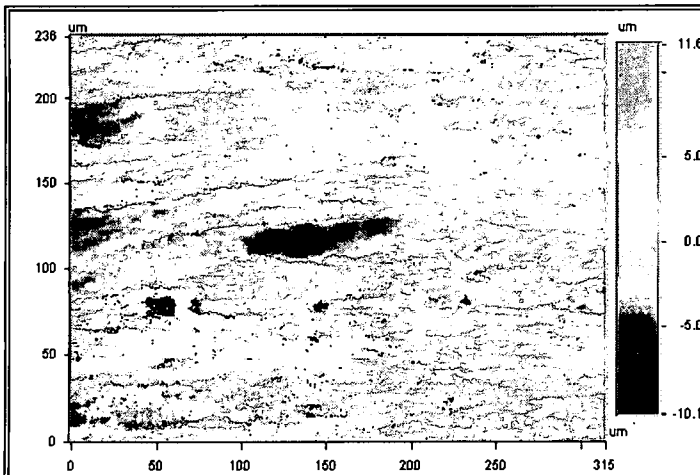


Figure 4.9: Optical image of MA754HT

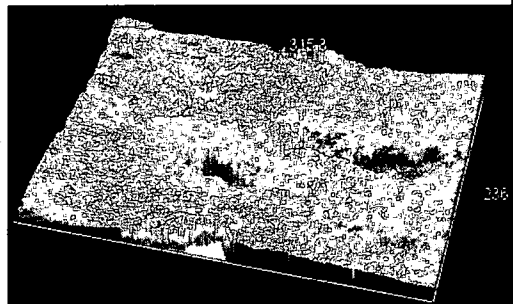
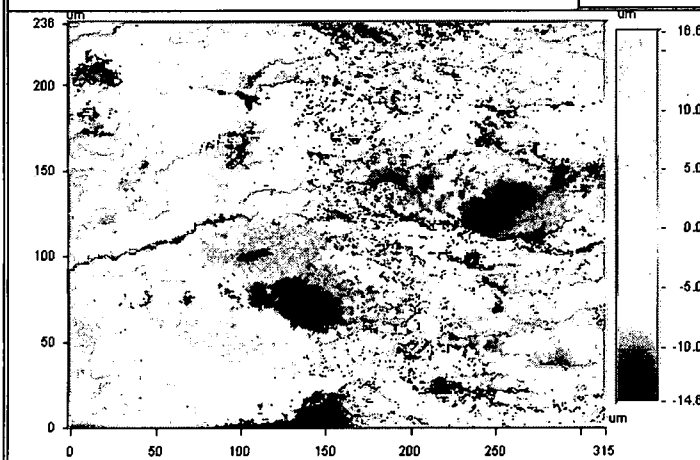
Table 4.9: Surface and 3D images of sample# 5 taken from White Light Interference

Microscope

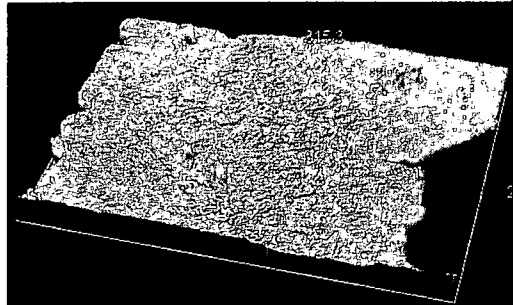
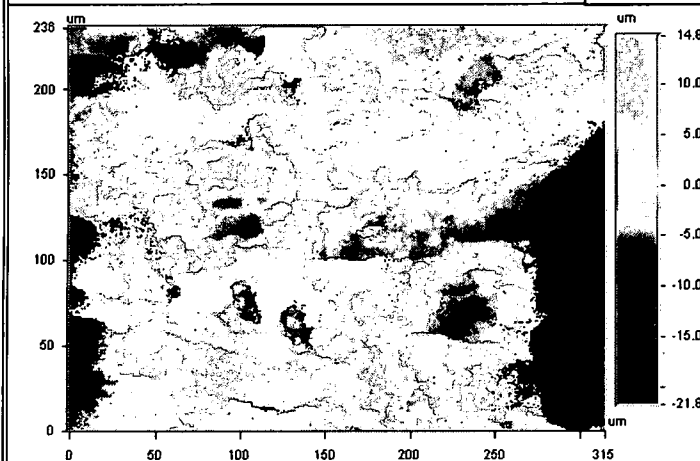




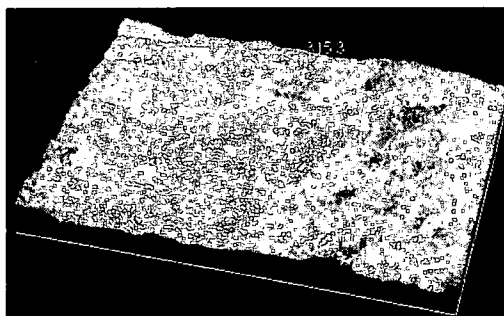
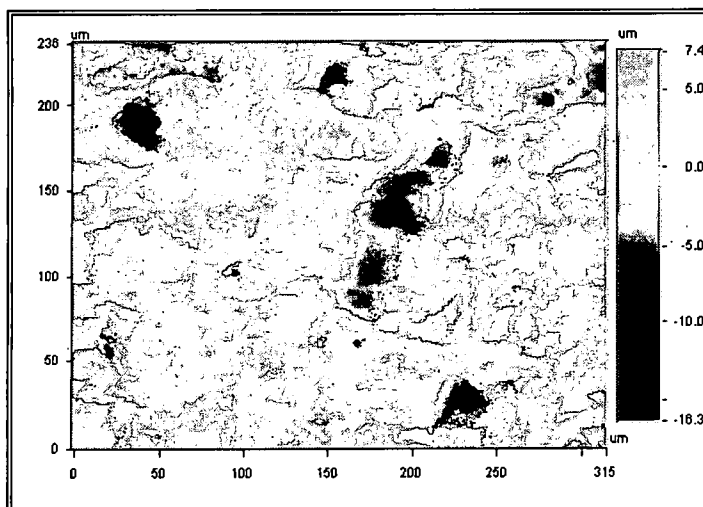
Position No. 4



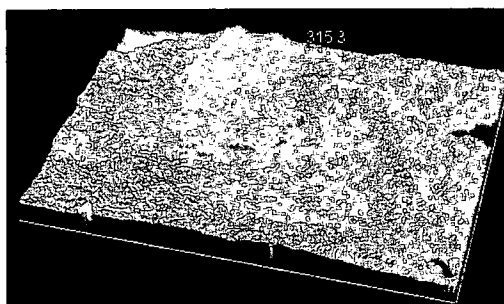
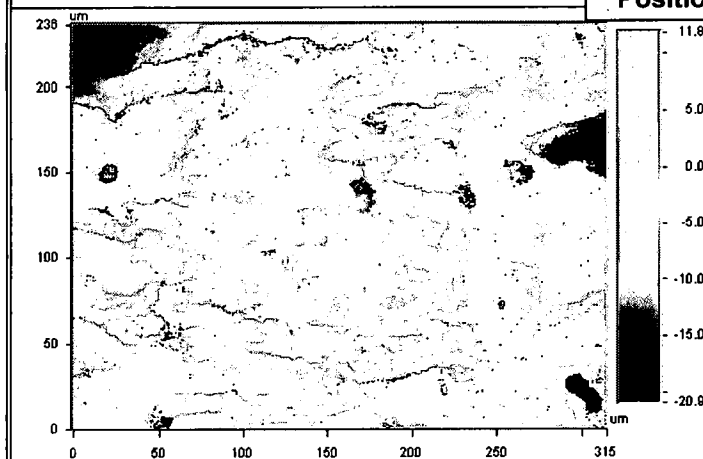
Position No. 5



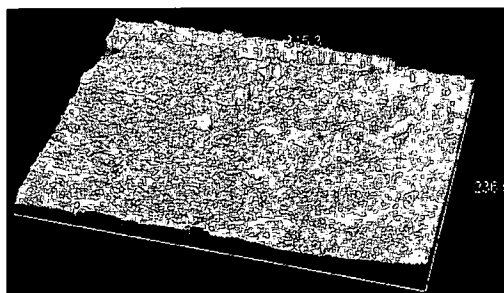
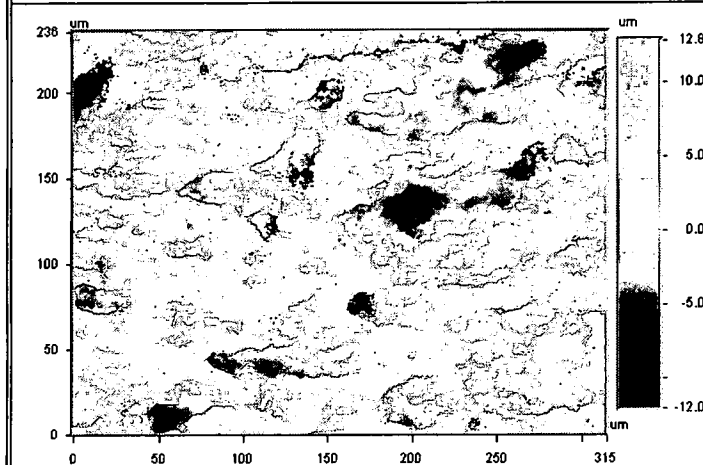
Position No. 6



Position No. 7



Position No. 8



Position No. 9

Table 4.10: Surface Roughness measurements with respect to crack length

Distance(mm)	0.63	1.26	1.89	2.52	3.15	3.78	4.41	5.04	5.67
$R_q(\mu\text{m})$	3.19	3.65	1.76	2.32	5.19	3.23	2.15	4.52	2.35

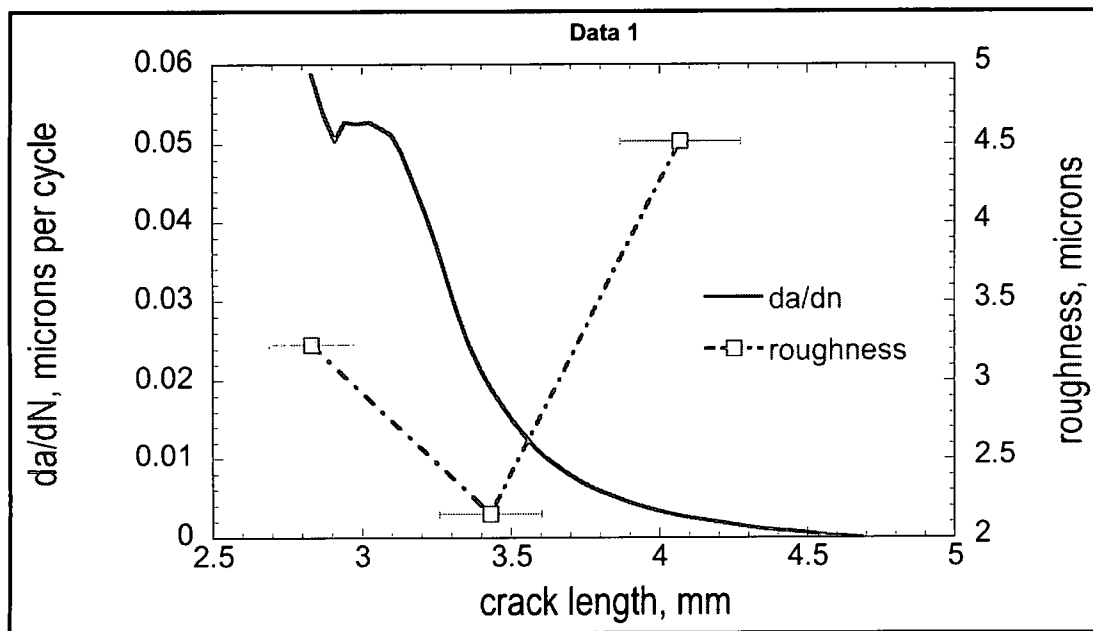


Figure 4.10: Graph plotted between crack length, crack growth rate and surface roughness

4.3) Comparison between surface roughness and crack growth rate

The crack growth rate and stress intensity factor ΔK measured during fracture testing for all the samples are shown in the Figure 4.11. Initially the crack grows faster, and then a linear growth is observed. Finally as the rate decreases a nonlinear behavior is observed. The linear behavior is most interesting region known as Paris region, which is often used for life prediction of materials. The slope in this region is linear.

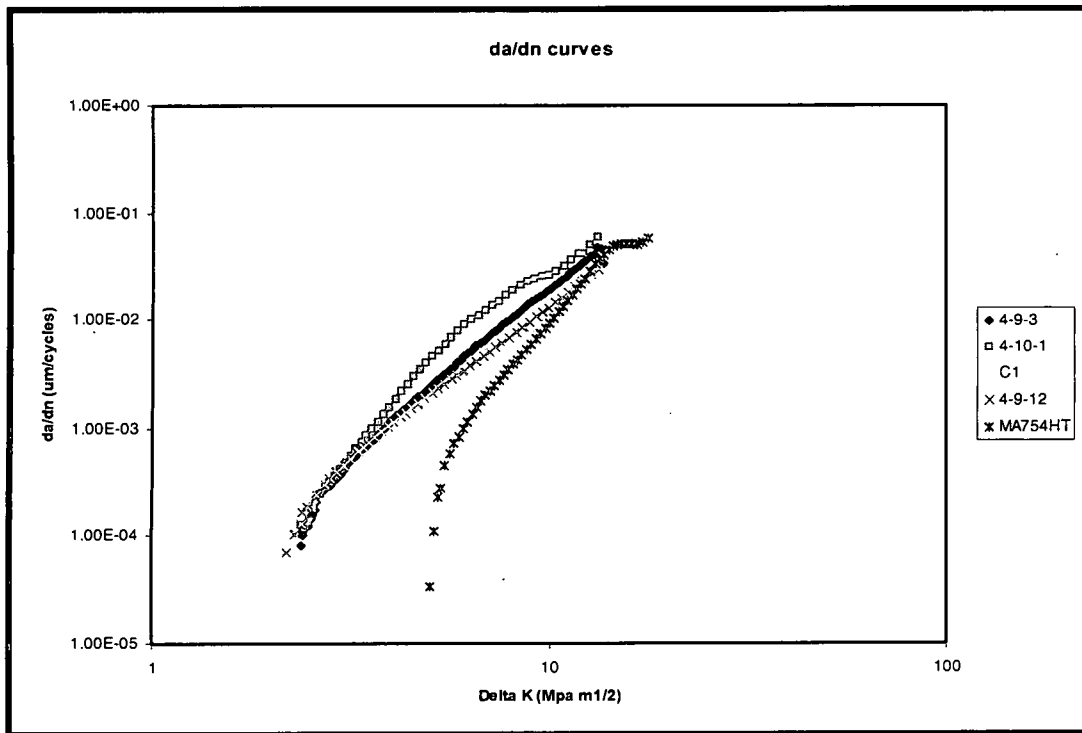


Figure 4.11: Plot between stress intensity factor and crack growth rate

In general, in the white light interference microscope measurements the surface roughness is measured as a function of distance from the notch. Each position is a length of the crack that has grown. Thus a plot of distance from the notch Vs surface roughness is similar to crack length Vs surface roughness. As *Figure 4.12* indicates the surface roughness decreases as the crack growth rate decreasing. In the case of sample MA754, no clear relationship is observed. In order to understand the relationship between crack growth and surface roughness only Paris region is examined. *Figure 4.13* shows a plot of surface roughness verses ΔK for all the samples. For the cryogenically milled and multiaxis forged samples, a linear relation between surface roughness and crack growth rate da/dn is observed. For sample MA754HT no such clear relationship is observed. The reason behind the decreasing of surface roughness values as the crack growth decreases is that the surface is the easiest to accommodate any amount of instability, most of the dislocations shoot to the surface and hence create

individual, discrete steps which are visioned as surface roughness. When strain energy applied on the material is decreasing relatively, and then the crack growth rate also decreases as shown in the *Figure 4.11*. As the crack growth rate decreases, the surface roughness decreases because the material has enough time to accommodate the strain energy created by the crack. So, the dislocations gets created and annihilated with the material. Thus the surface roughness of material becomes smoother

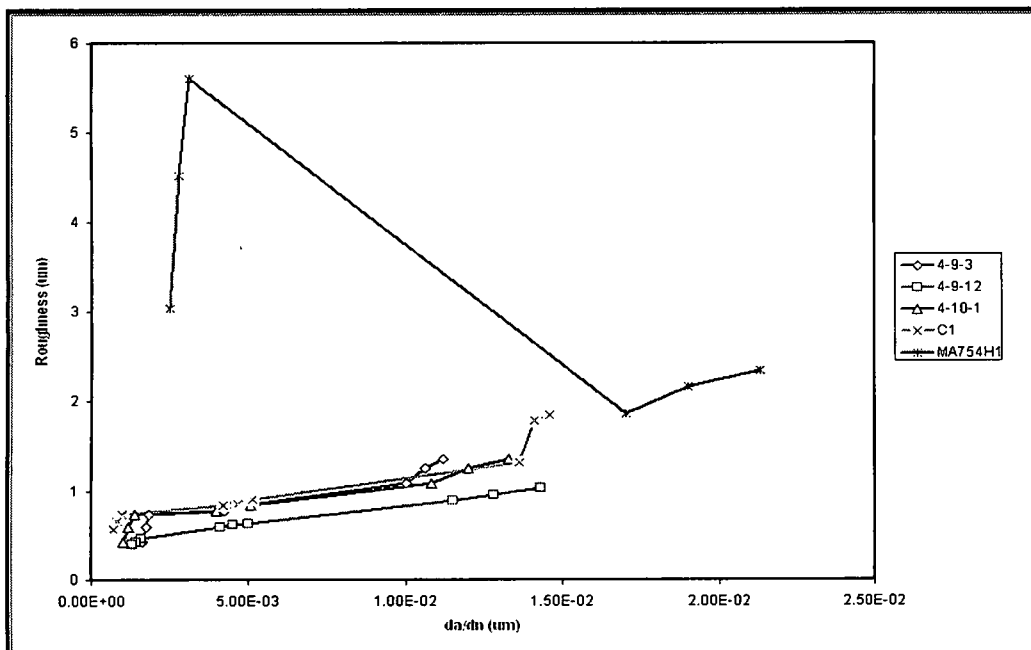


Figure 4.12: Graph between crack growth rate and surface roughness

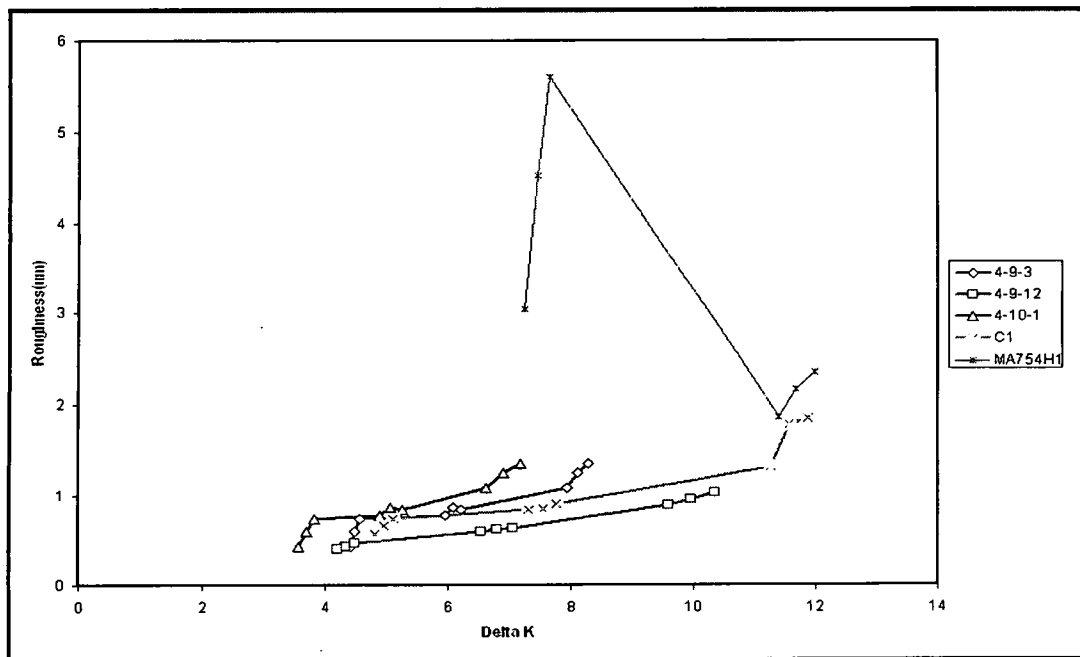


Figure 4.13: Graph between stress intensity factor and surface roughness

In the cryogenically milled and multiaxis forges samples, the grain size is in the range of 100nm-800nm, while in the case of MA754, it is large. Thus it appears that grain size plays a role in generating rough surfaces and affects the crack growth rate.

CHAPTER 5

MICROSTRUCTURAL ANALYSIS

5.1) Importance of Fractography

Fractography is defined as interpretation of characteristics of fracture surface. Fracture surface micrographs reveal a number of patterns and well defined features in the image. These patterns are dependent on many factors such as the chemical composition, deformation behavior of the material, the testing methods and its conditions and the sequence of micro deformation processes that resulted in the nucleation and propagation of a crack. Fractography not only reveals the features of surface images but also the relation of crack propagation with fracture surface topography. Thus, the analysis of fractography is a diagnostic tool for failure analysis. In this study, the crack propagation micrographs are obtained by atomic force microscopy, ultrasonic force microscopy and scanning electron microscopy. Features on the fractured surfaces can be related to information regarding the load, severity of environment and quality of material.

Macroscopically, fractured surfaces appear as flat, shiny and smooth as shown in the *Figure 5.1*. They contain beach markings and clamshell on the surface which are produced by the variation of load amplitude during each cycle at uniform intervals. These beach marks are also called “striation” marks, which represent the position of crack propagation per load cycle. In order to observe these features and patterns of a fracture surface, high-resolution micrographs are essential. These micrographs are obtained using microscopes,

generally optical, and SEM techniques are used for fractured surfaces, but in this study an innovative technique is introduced for studying fracture surface topography at nanoscale by atomic force microscope and ultrasonic force microscope.

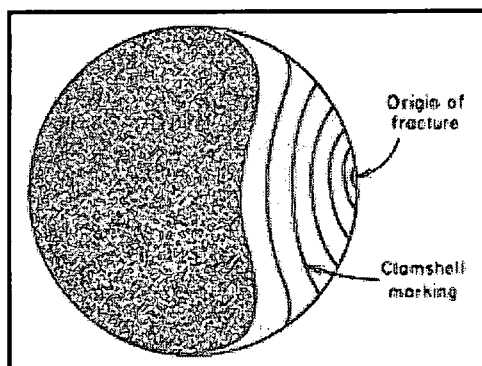


Figure 5.1: Schematic of macroscopic fracture surface[8]

5.2) Advantage of AFM-UFM in Fractography

The technique of AFM has been used previously to study the behavior of slip deformation at crack tip at one fatigue cycle loading [1]. A very little amount of study is carried out using UFM on the fatigue fracture surface analysis. These instruments play a major role in analyzing the surface topography of fractured surfaces at nanoscale range. AFM was used for observing the fracture processes and dislocation movements with very high magnifications. The vertical resolution is greater than 1/10 nm and its lateral resolution is in a range of 20-50nm depending on the tip radius. It consists of maximum scan range of 100 μ m in lateral directions. As the fracture surfaces are rough, its roughness index may be around 0.8 as that of universal value which is independent of material and fracture mode. Even SEM which is considered to be standard instrument for analysis of fractured surfaces could not appreciatingly performs this task as it is limited to small length scale roughness index between 0.4 and 0.5 whereas AFM precisely evaluate

these factor . A quantitative analyzes of fractured surfaces are produced using AFM which was cited by Pascal Daguer [23]. A major advantage of using AFM for fracture surfaces is it doesn't require any sample preparation or chemical etching of surface to be imaged so that we don't loose any information of fracture features in the material.

Ultrasonic force microscope is used to map low frequency elastic properties of a material. This is the major feature which cannot be performed by the any of the conventional techniques. By adapting this, the contrasts of the images produced by AFM are greatly increased and it also measures the elastic properties of material. Hence by these two techniques AFM combined with UFM will provide both surface topography at nanoscale and an image with very good contrast and resolution. This instrument plays an important role in characterizing the fractured surfaces and its deformation behavior at nanoscale particles which are practically not possible using SEM techniques.

5.3) Results

In this section, results obtained from microstructural analysis on Ni-20wt. %Cr sample are discussed. Ni-20wt. %Cr sample are numbered from 1 through 5. On each of the sample, AFM-UFM and SEM was used to image the microstructure at different place on the sample.

Sample # 1 Ni- 20wt.%Cr, GE sample number 4-9-3

A macrograph of the fracture surface is shown in *Figure 5.2*. With reference to *Figure 5.2*, the fatigue precrack is the split, slightly lighter regions in regions 1 and 2. The measured fatigue crack growth took place in regions 1 through 9. Post-test fatigue to break apart the sample is the bright smooth region to the right of region 9; tensile rupture is the rough right-most region of the sample

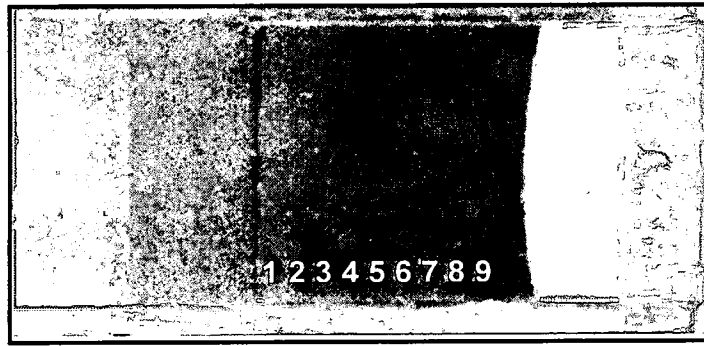


Figure 5.2: Optical image of Ni- 20wt.%Cr

Image is taken at position 1-3 on the sample as shown in the *Figure5.2*. At this position the crack growth rate and roughness values are high. AFM-UFM images as shown in *Figure 5.3* are taken at the scan size of $4.88\ \mu\text{m}$ with an ultrasonic frequency of 420 KHz. The height scale in this image was $0\text{-}3\ \mu\text{m}$. The grains are clearly seen in this image while the left image show AFM image and right image is an UFM image. The contrast of UFM is more than the AFM image. The grains at this position are projecting in one direction.

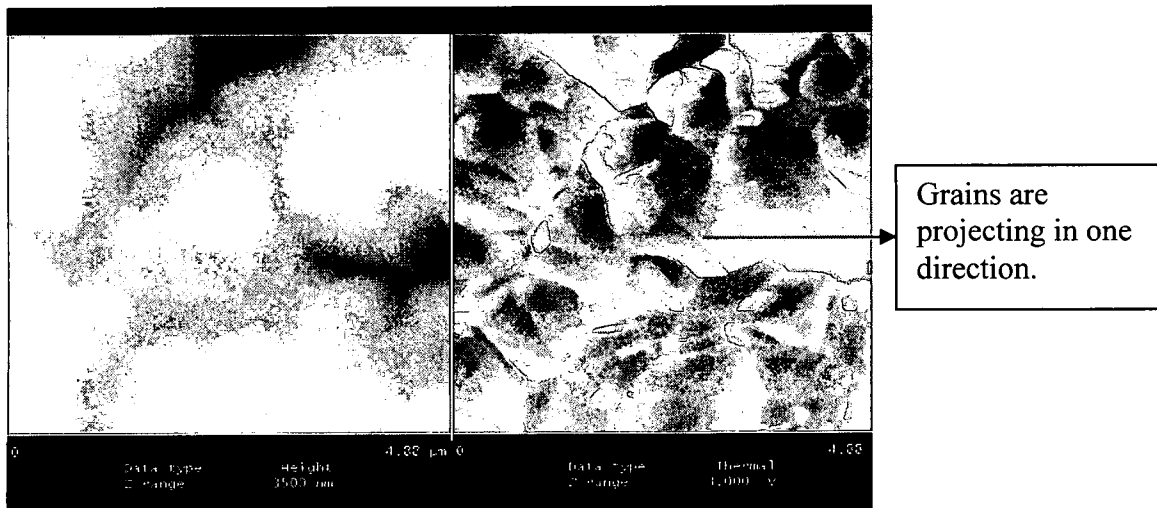


Figure 5.3: AFM-UFM image of Ni-20wt. %Cr sample at position 2-4

The image in *Figure5.4* is taken at position 5-6 where crack growth rate is decreasing gradually. Images are taken at the scan size of $10\ \mu\text{m}$ with an ultrasonic frequency of 570

KHz. In this image the grains appear to be oriented. Large area of images show pattern of striations. The deformation appears to be taking place through striations.

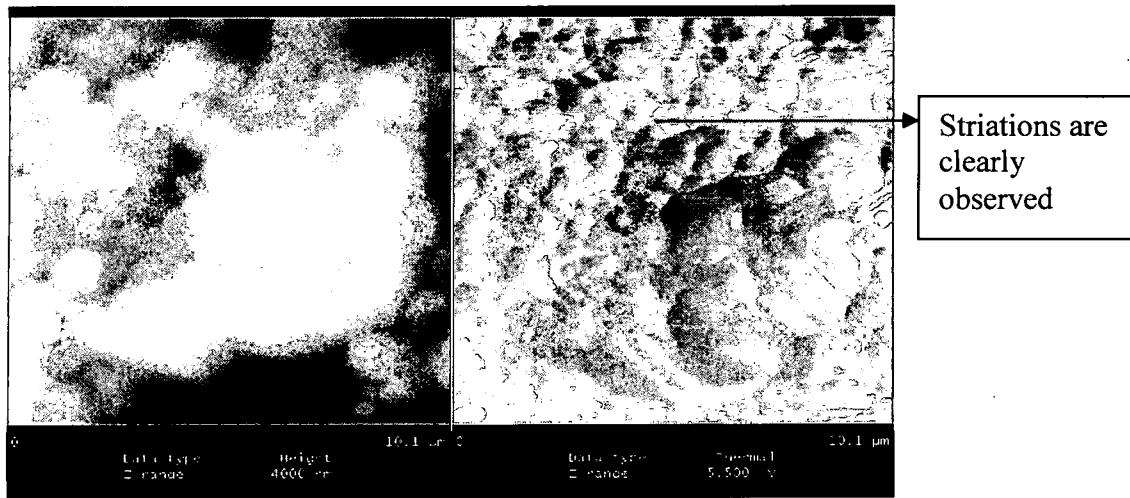


Figure 5.4: AFM-UFM image of Ni- 20wt.%Cr sample at position 5-6

Image in *Figure 5.5* is taken at region of low roughness and decreasing crack growth rate. It is taken at position 7-9 on the sample as indicated in the *Figure 5.2*. This image is taken at scan size of $3.31\text{ }\mu\text{m}$ at ultrasonic frequency of 380 KHz. The average grain size of Ni-20Cr sample as calculated from this method is 500nm. The transgranular deformation is observed in this material. The number striation has decreased when post fatigue region is approached where the crack growth rate decreases. The slip deformation is not observed in this material.

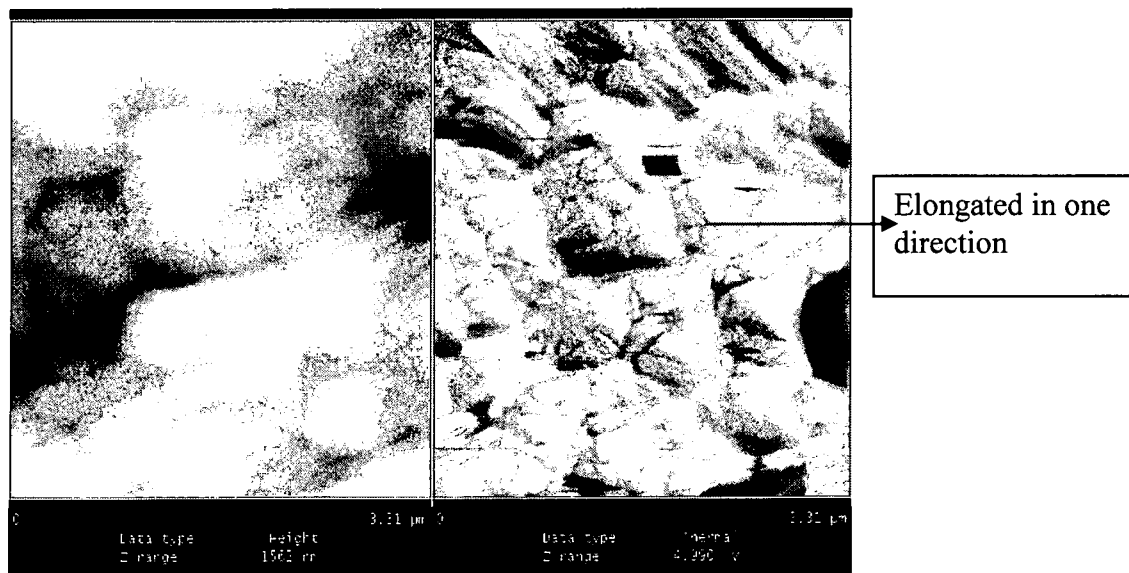


Figure 5.5: AFM-UFM image of Ni- 20wt.%Cr sample at position 7-9

Sample # 2 Cryogenically milled Ni- 20wt.%Cr , GE sample number 4-9-12

A macrograph of the fracture surface is shown in *Figure 5.6*. With reference to *Figure 5.6*, the fatigue precrack is the split, slightly darker regions in regions 1 and 2. The measured fatigue crack growth took place in regions 1 through 6. Post-test fatigue to break apart the sample is the bright smooth region to the right of region 6; tensile rupture is the rough right-most region of the sample.

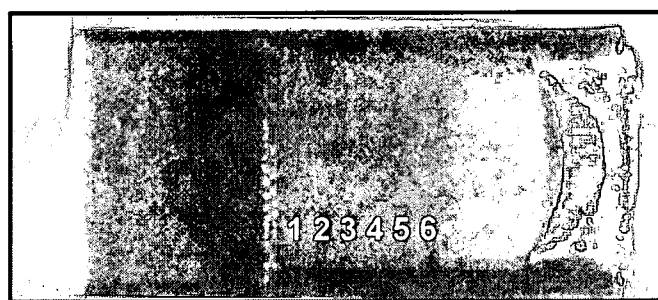


Figure 5. 6: Optical image of Cryogenically milled Ni- 20wt.%Cr

Images in *Figure 5.7* are taken at position 1-2 on the sample as shown in the *Figure 5.6* at high crack growth rate and high roughness values. These images are taken at scan size of 814nm at ultrasonic frequency of 108 KHz. In AFM image grains at nanoscale are observed. In UFM contrast of image is increased and grains with there grain boundaries are clearly observed. As observed from the images all grains are oriented in one direction.

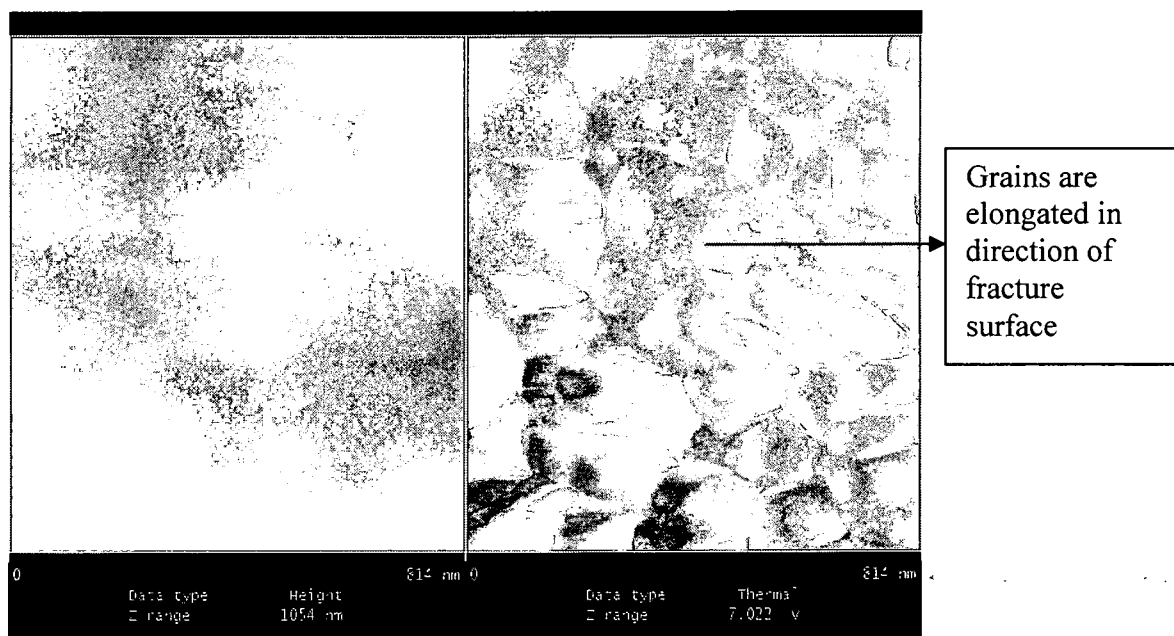


Figure 5.7: AFM-UFM image of cryogenically milled Ni- 20wt.%Cr sample at position 1-2

Image in *Figure 5.8* is taken at position 4-5 on the sample as shown in above *Figure 5.6* at decreasing crack growth rate. The image is taken at scan size of 1.3 μ m at ultrasonic frequency of 430 KHz. In UFM nanoscale grains are clearly observed with high contrast as compared with that of AFM images. From this image it assumed the crack is passing through the grain boundaries with disturbing the grains in the material.

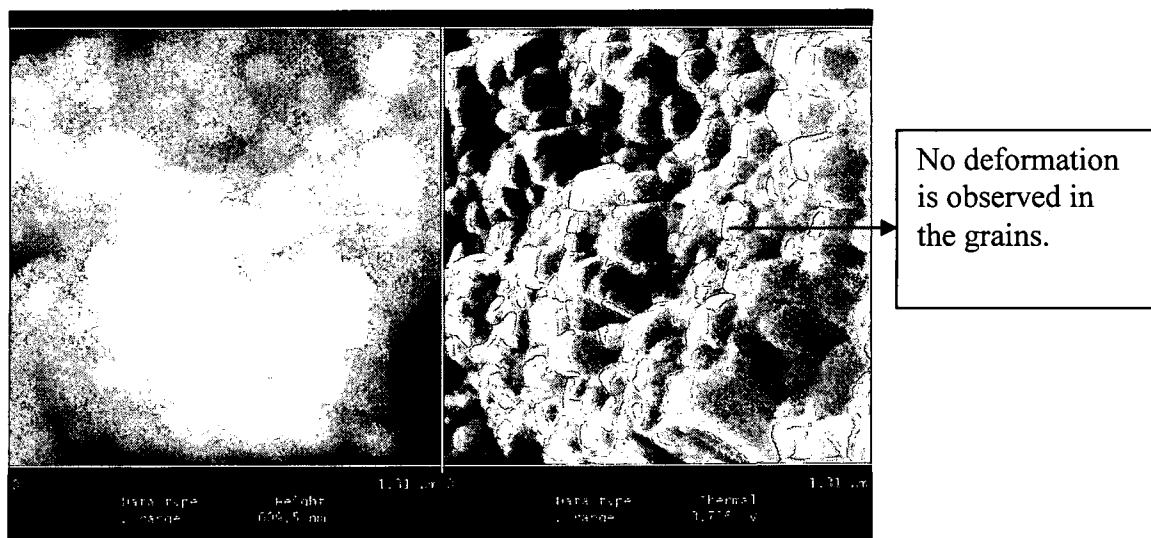
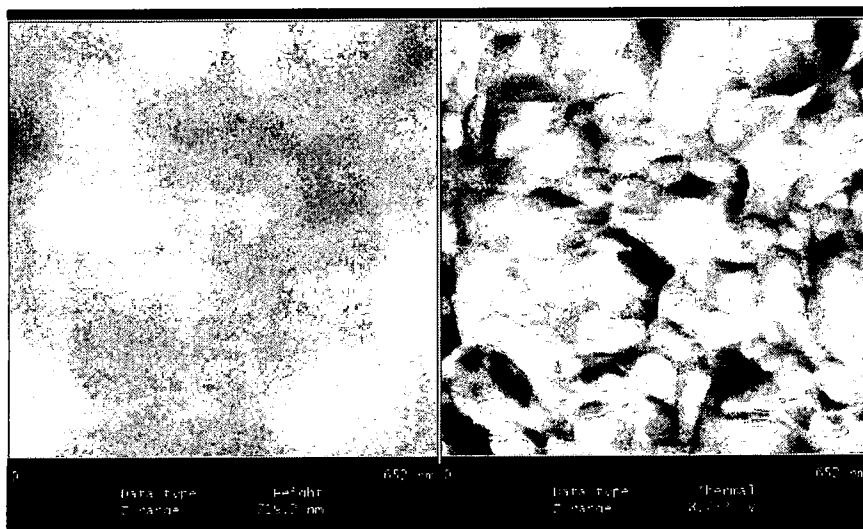


Figure 5.8: AFM-UFM image of cryogenically milled Ni- 20wt.%Cr sample at position 4-5

Images in *Figure 5.9* are taken at position 5-6 on the sample as shown in above *Figure 5.6*. At this position the crack growth rate and roughness of the material is very low. The image is taken at scan size of 652nm and at ultrasonic frequency of 470 KHz. In this image the surface topography is almost flat, grains are not projecting. Nano scale grains are clearly observed in UFM images. The average grain size of cryomilled Ni-20 wt. %Cr is 100nm. The deformation occurs through grain boundaries in this material as grain size.



Grains are
almost
symmetric.

Figure 5.9: AFM-UFM image of cryogenically milled Ni- 20wt.%Cr sample at position 5-6

Sample # 3 GE sample number 4-10-1Ni- 20wt.%Cr +Al₂O₃, GE sample number 4-10-1

A macrograph of the fracture surface is shown in *Figure 5.10*. With reference to *Figure 5.10*, the fatigue precrack is the dark triangle in regions 1 and 2. The measured fatigue crack growth took place in regions 3 through 8. Post-test fatigue to break apart the sample is the light-colored region to the right of the micrograph.

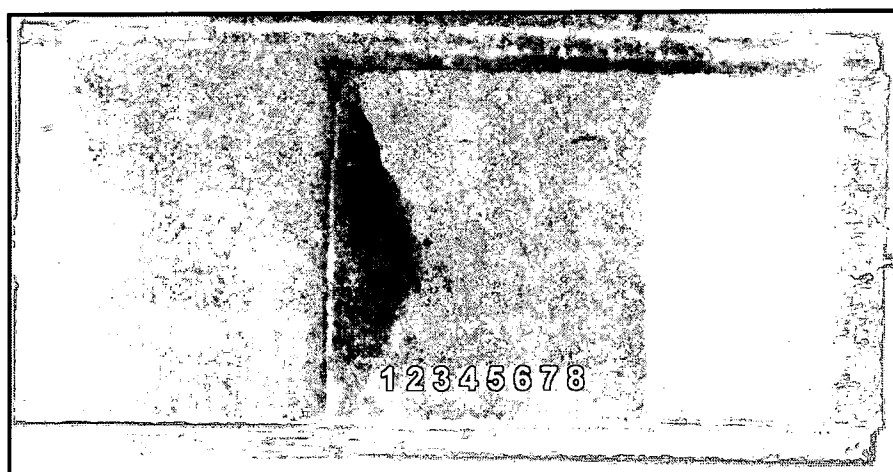


Figure 5.10: Optical image of Ni- 20wt.%Cr+Al₂O₃

AFM-UFM images are taken at position 2-4 on the sample as shown in the *Figure 5.10*. These images as shown in *Figure 5.11* are taken at a scan size of $1.23\mu\text{m}$ and at ultrasonic frequency of 370 KHz. In UFM image steps and slips in the grains are clearly observed. Deformation is taking place through the slips in a direction of crack growth rate. The slips observed in this material might be due to the presence of Al_2O_3 particles. These particles are large grains whose average grain size is approximately $1\mu\text{m}$. The step heights are calculated using AFM image.

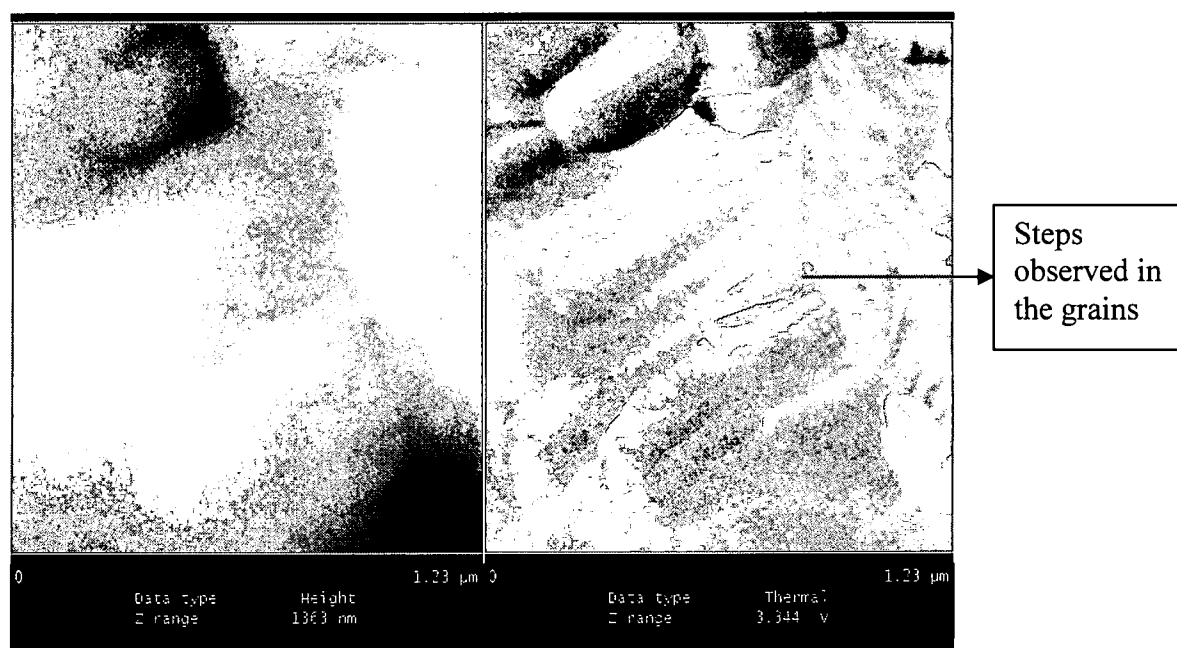


Figure 5.11: AFM-UFM image of Ni- 20wt.%Cr+ Al_2O_3 sample at position 2-4

Images in *Figure 5.12* are taken at position 5-7 on the sample, where the crack growth rate is decreasing and the surface roughness values are also decreasing. The images are taken at scan size of 982nm and at frequency of 370 KHz. In these images steps are observed clearly but there are not slips in the grains. The deformation is taking place through the grains which might be a transgranular deformation.

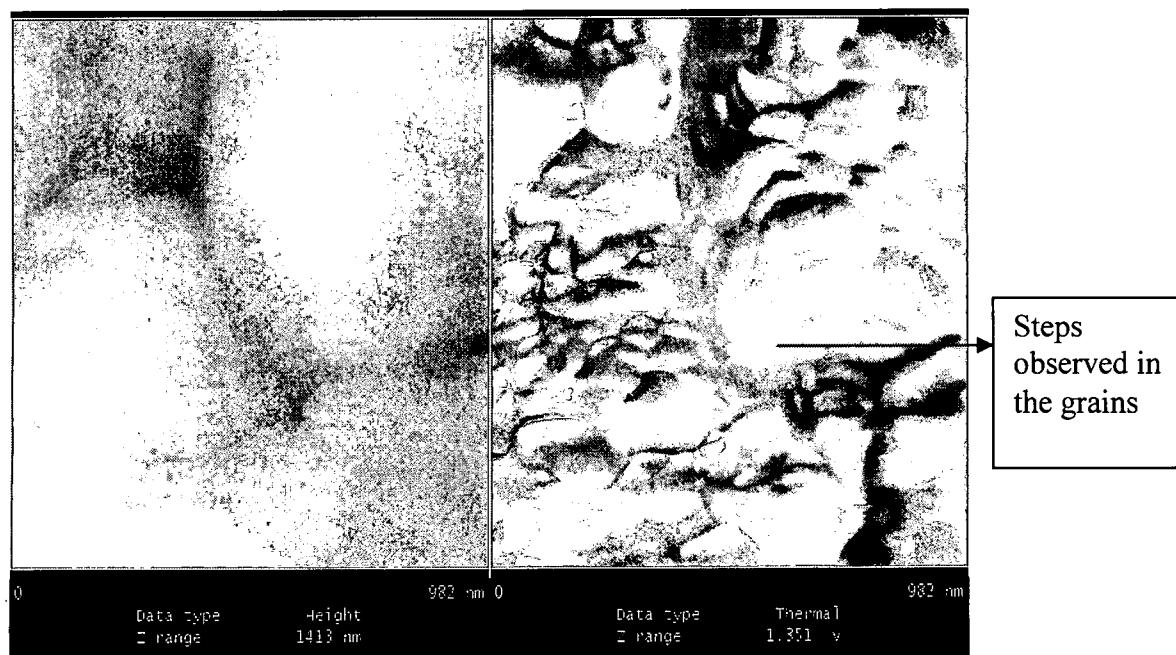


Figure 5.12: AFM-UFM image of Ni- 20wt.%Cr+Al₂O₃ sample at position 5-7

Images in *Figure 5.13* are taken at position 7-8 on the sample as shown in the above image. At this position the crack growth rate and surface roughness values are very low. These images are taken at the scan size of 831nm and at the frequency of 370 KHz. In these images slips and steps are not observed the topography appears to be smooth as if there is no deformation taking place at this position on the sample surface. Nano sized particles are observed in AFM-UFM images. As observed from the above images, it is clearly observed that as the crack growth rate decreases surface deformation on the material also decreases.

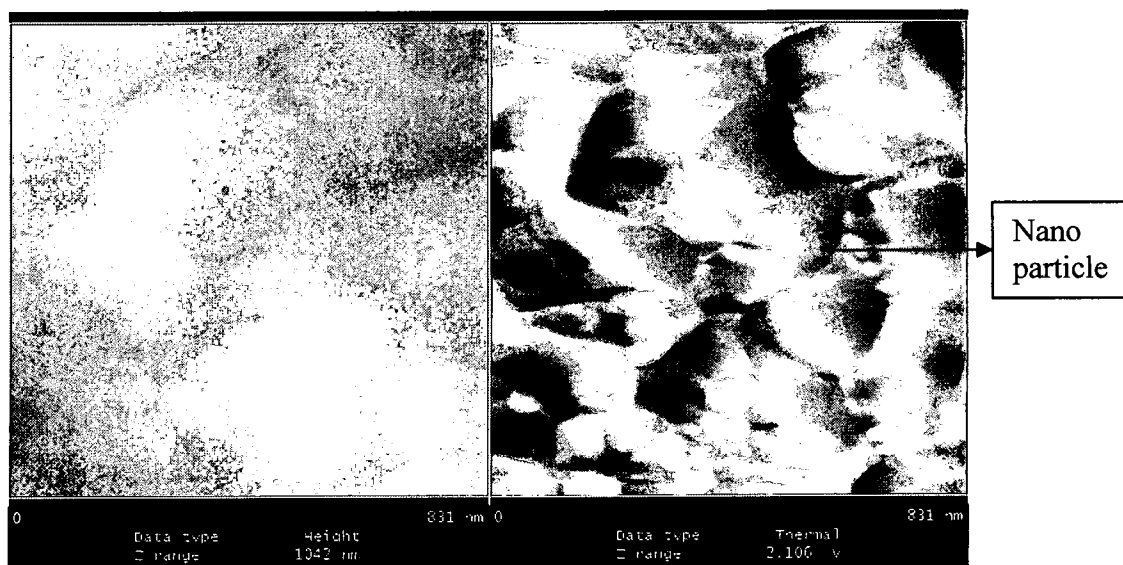


Figure 5.13: AFM-UFM image of Ni- 20wt.%Cr+Al₂O₃ sample at position 7-8

Sample # 4 C1 Forged

A macrograph of the fracture surface is shown in *Figure 5.14*. With reference to *Figure 5.14*, the fatigue precrack is the split, slightly dark regions in regions 1 through 3. The measured fatigue crack growth took place in regions 2 through 5. Post-test fatigue to break apart the sample is regions beyond 5.



Figure 5.14: Optical image of C1 forged Ni- 20wt.%Cr

Image is taken at the center of position 1-2 on the sample as shown in the *Figure 5.14*. AFM-UFM images shown in *Figure 5.15* are taken at a scan size of 2.86 μm and at ultrasonic frequency of 460 KHz. The contrast of UFM images is more than an AFM

image. Slip deformation is observed in the grains as the images are taken at high roughness and da/dn values. As inferred from the images each and every grain is participating in the deformation mechanism. The average grain size of C1 forged sample is $1.2\mu\text{m}$.

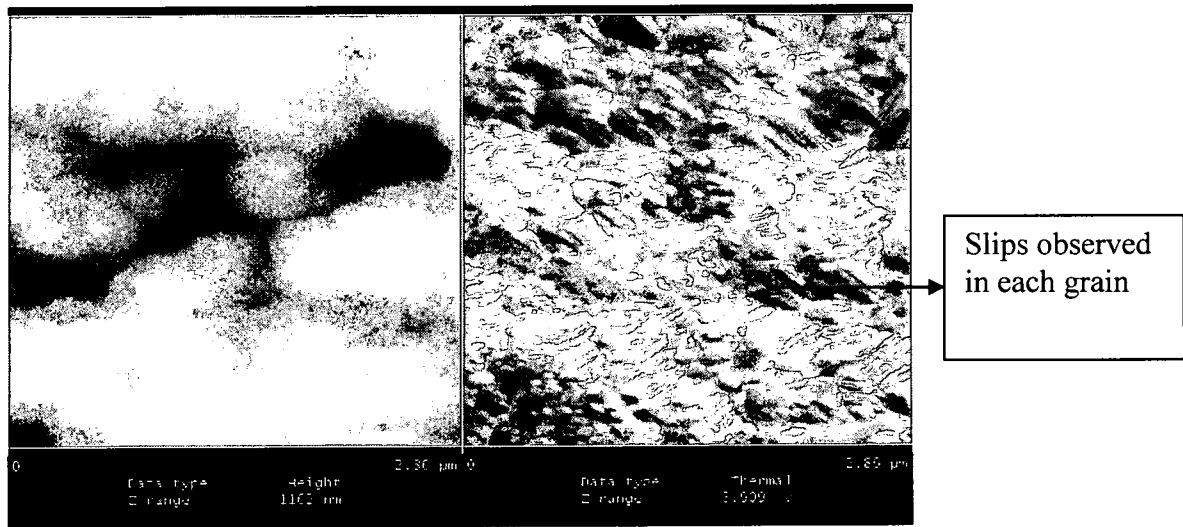


Figure 5.15: AFM-UFM image of C1 forged sample at position 1-2

Images in *Figure 16* are taken at position 3-4 on the sample as shown in the above *Figure 5.14*. Image is taken at scan size of $1.92\mu\text{m}$ and at frequency of 460 KHz. Only on few grains slip deformation is observed and a grain boundary is clearly seen in the AFM & UFM images. At this position da/dn value is decreasing, so number grains participating in the slip deformation is decreasing gradually.

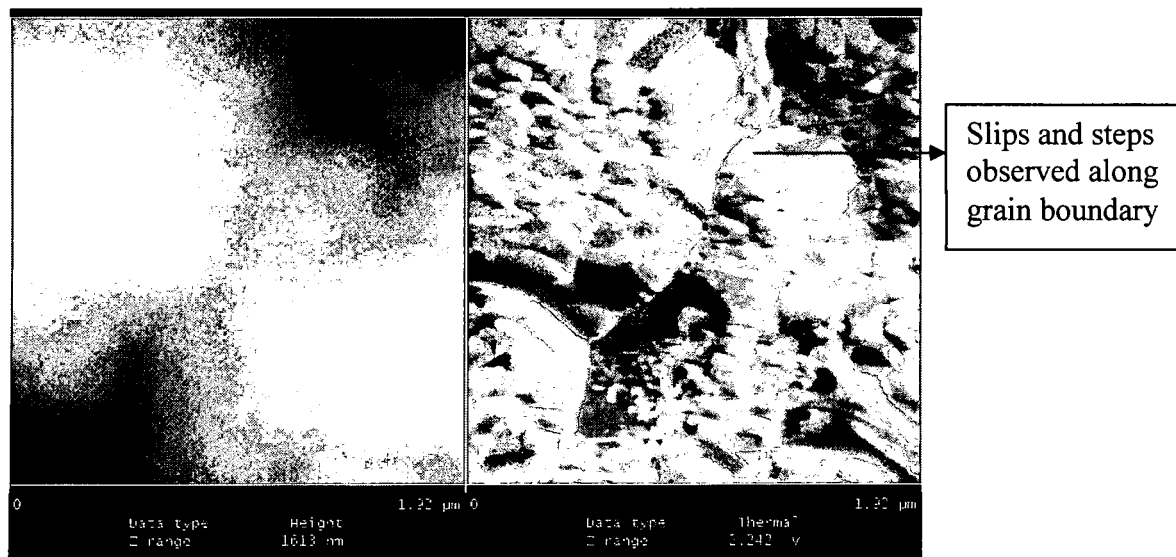


Figure 5.16: AFM-UFM image of C1 forged sample at position 3-4

Images in *Figure 5.17* are taken at position 6 (post-test high cycle fatigue) on the sample. Images are taken at scan size of 487nm and at frequency of 460 KHz. All grains at nano scale are observed. There is no slip deformation taking place at this position. Surface roughness value is very low at this position.

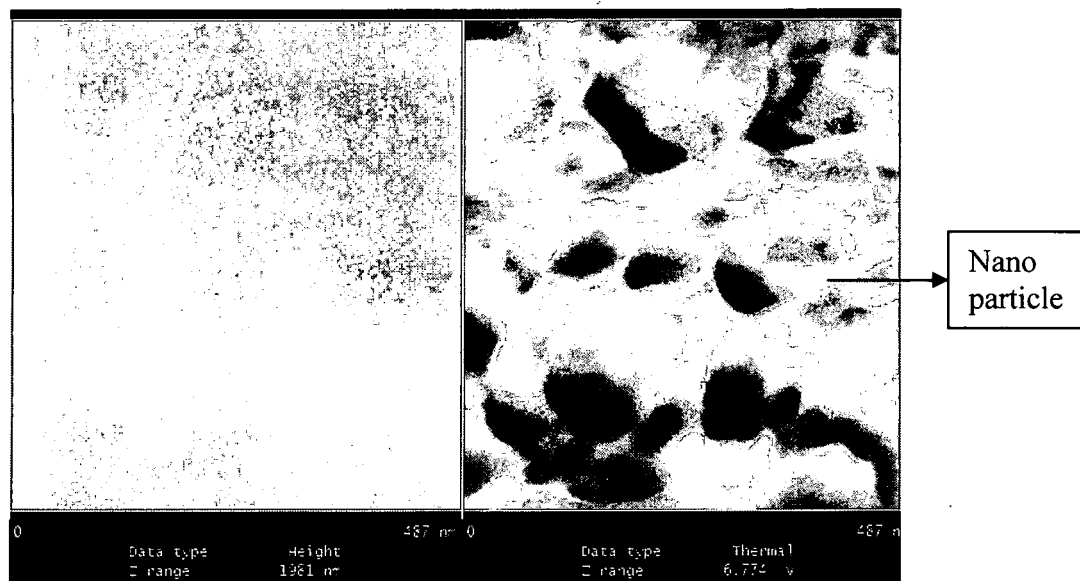


Figure 5.17: AFM-UFM image of C1 forged sample at position 6

Sample # 5 MA754HT, GE Sample number MA754-HT1

A macrograph of the fracture surface is shown in *Figure 5.18*. With reference to *Figure 5.18*, the fatigue precrack is the split, slightly dark regions in regions 1 and 2. The measured fatigue crack growth took place in regions 3 through 6. Post-test fatigue to break apart the sample is regions 7-9; tensile rupture is the bright region to the right of 9.

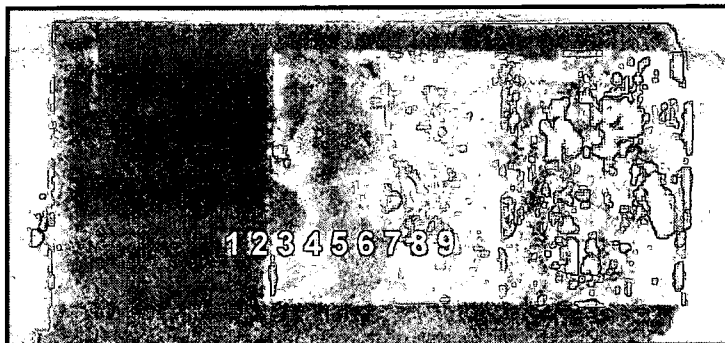


Figure 18: Optical image of MA754HT

Images are taken at position 3-4 on the sample as shown in the *Figure 5.18*. The AFM-UFM images as in *Figure 5.19* are taken at scan size of $3.26\mu\text{m}$ and at frequency of 520 KHz. These images clearly show the slips and steps taking place in the grains. In MA754 each and every grain participates in slip deformation. MA754 consists of elongated grains. Transgranular deformation is observed in this material. The distance between the slips are calculated using AFM image and average slip distance is 200nm. The average grain size as calculated from AFM images is $2\mu\text{m}$.

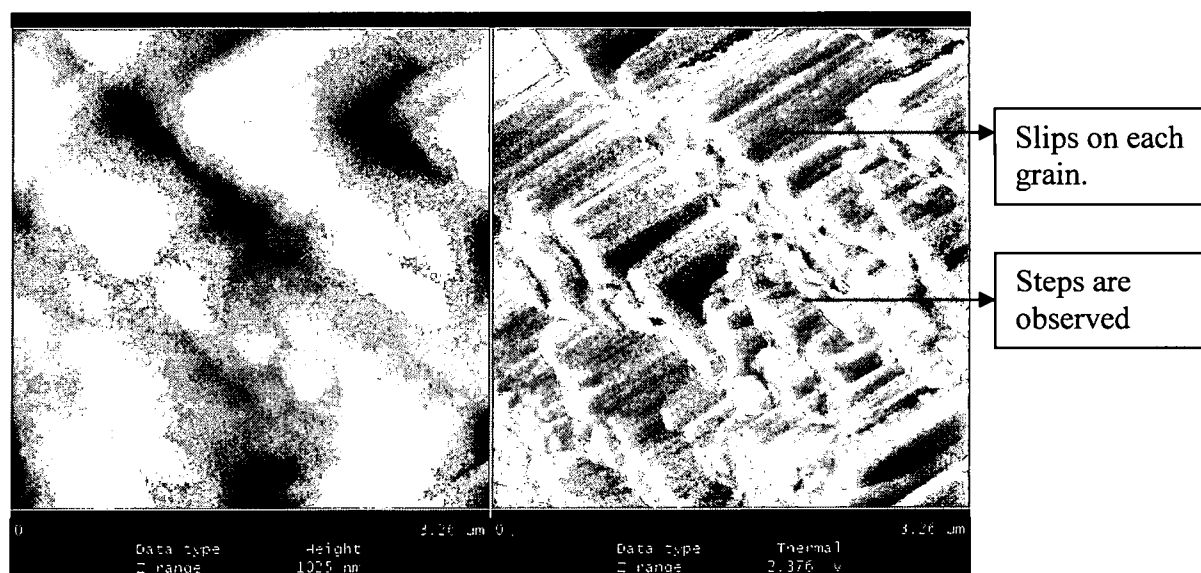


Figure 5.19: AFM-UFM image of MA754 HT sample at position 3-4

Images in Figure 5.20 are taken at position 5-7 on the sample at scan size of 2.60 μm and at frequency of 515 KHz. Slips are observed in the grains. In UFM images Y_2O_3 particles are clearly observed whereas in AFM image these particles are not dominantly visible.

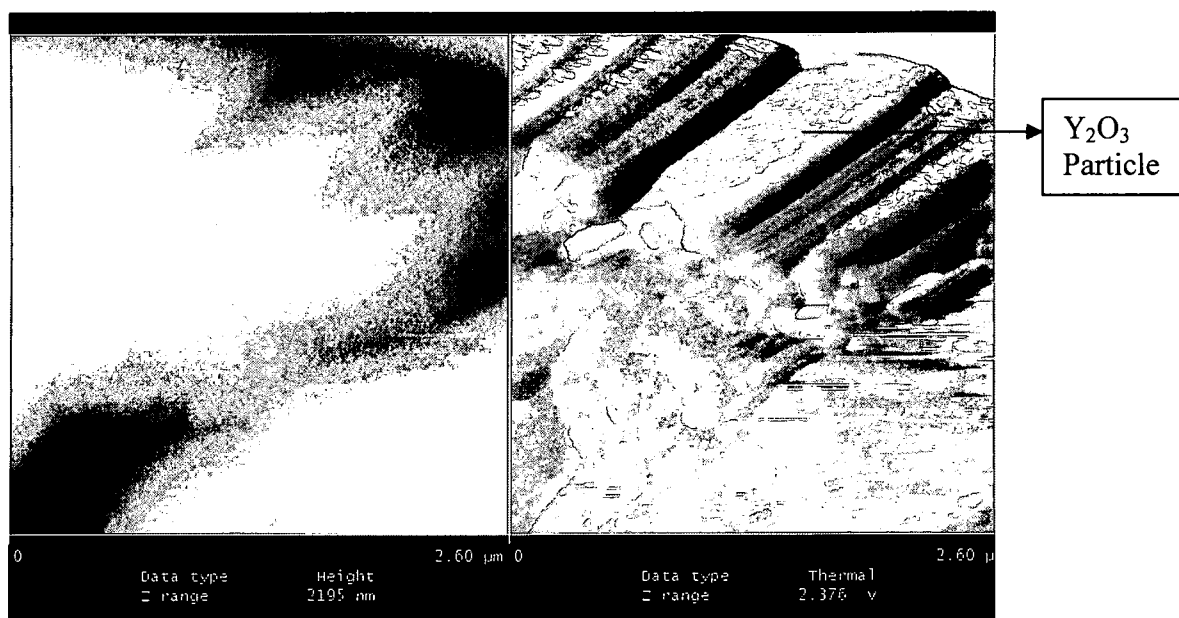


Figure 5.20: AFM-UFM image of MA754HT at position 5-6

Images in *Figure 5.21* are taken at position 6-7 on the sample where the roughness value is high and are taken at scan size of $4.26\mu\text{m}$ at frequency of 514 KHz. This represents the post-test region, where a high-cycle fatigue crack was grown in order to break apart the sample. In AFM-UFM images steps are clearly observed. It might be a one grain in which the steps are observed. The step height is calculated in AFM image. These images can be compared with AFM-UFM images of CaF_2 sample.

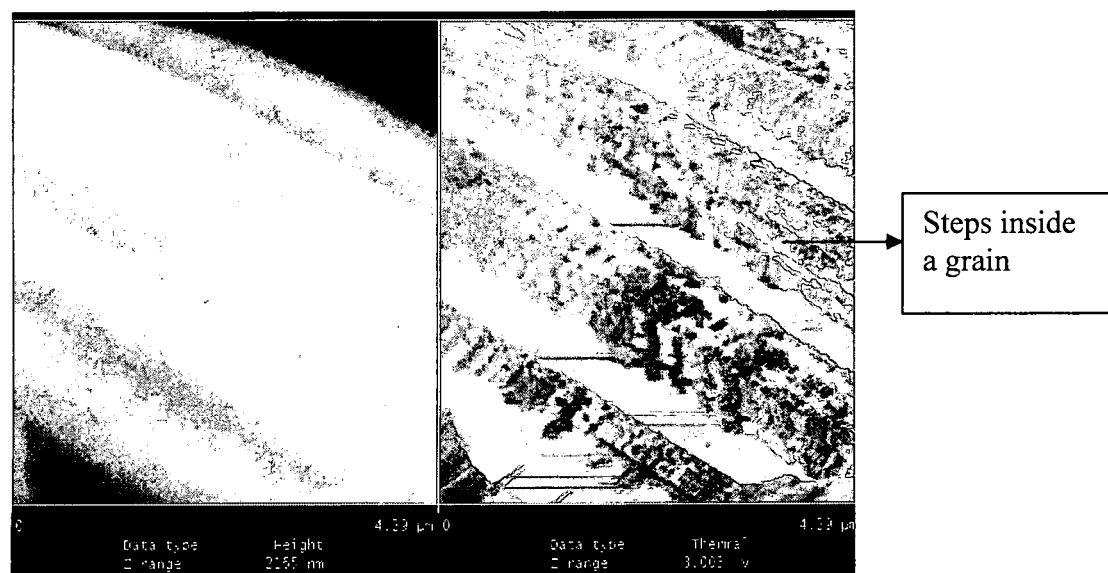


Figure 5.21: AFM-UFM image of MA754 HT sample at position 6-7

Images in *Figure 5.22* are taken at position 8-9 on the sample where the crack growth rate is governed by post-test high cycle fatigue. No slips are observed in AFM-UFM images. Deformation is taking place in a striation pattern as the number of cycles is decreasing. Elongated grains are clearly observed in the UFM image with a better contrast.

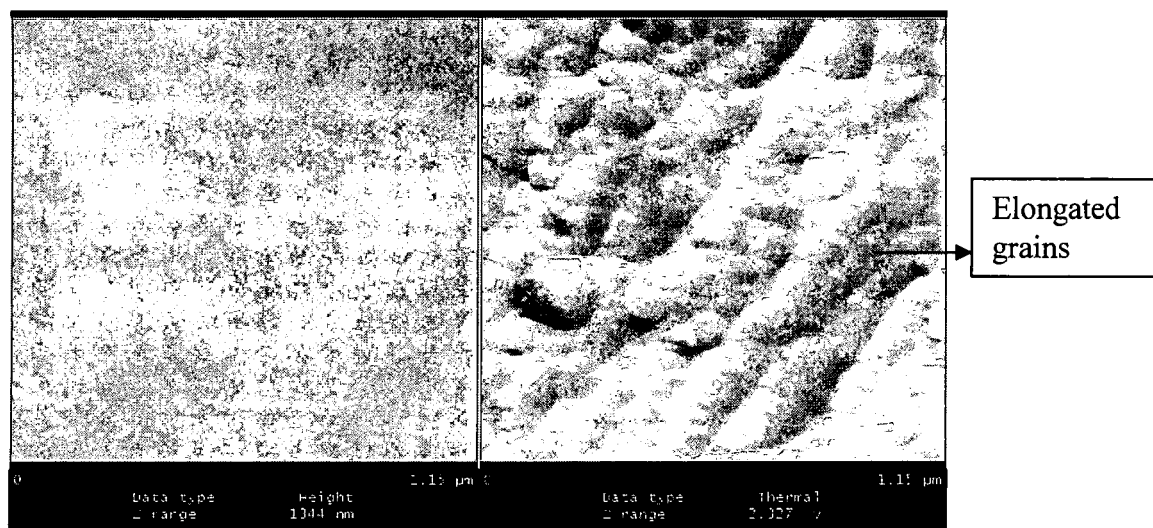


Figure 5.22: AFM-UFM image of MA754 HT sample at position 8-9

5.4) Comparison of AFM-UFM Images with SEM

Scanning electron microscope is used for imaging Ni- 20wt.%Cr samples. In this section SEM images are compared with that of AFM-UFM images. Difference in the surface features as observed from the SEM, AFM & UFM images in each sample is discussed. Images are taken at different positions on the sample surface. AFM-UFM images shown in this section are taken approximately in the region where the SEM images are taken. All the images are taken in the direction of crack growth.

Sample #1 Ni- 20wt.%Cr GE sample number 4-9-3

The images shown in *Figure 5.23* are taken on Ni- 20wt.%Cr sample. These two images are taken at the scan size of $8\mu\text{m}$. SEM images show the grains and other foreign particles but the contrast of images is not good enough. Grains are not clearly observed. AFM-UFM images perform a great contrast difference as compared to SEM images and the grains are clearly visible in these images.

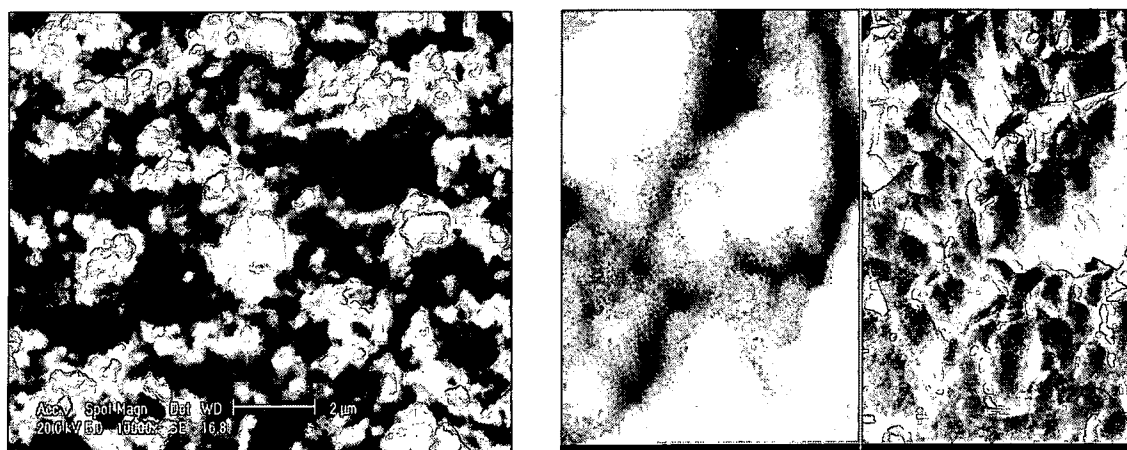


Figure 5.23: SEM and AFM-UFM images of Ni- 20wt.%Cr

Sample # 2 Cryomilled Ni-20Cr GE sample number 4-9-12

Figure 5.24 shows the SEM, AFM & UFM images taken on the cryomilled sample. SEM image is taken at scan size of $8\mu\text{m}$ at magnification of 10,000X. Large numbers of grains are observed in the image. Due to the limitation on the magnification in the SEM instrument, AFM-UFM images are taken. These images are the magnified image of SEM taken at scan size of $1.31\mu\text{m}$ and at frequency of 430 KHz. In AFM-UFM images nano size grains are clearly seen. The contrast of UFM image more dominant than AFM & SEM images.

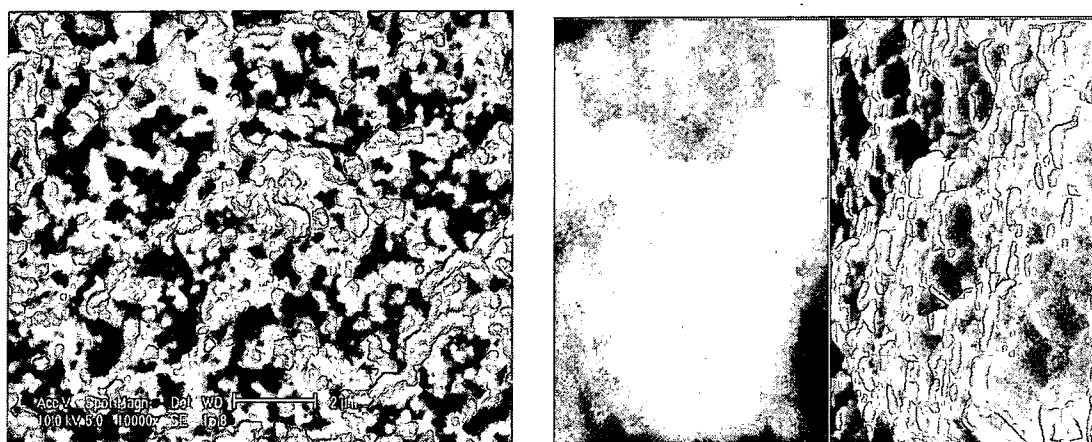


Figure 5. 24: SEM and AFM-UFM images of cryogenically milled Ni- 20wt.%Cr

Sample #3 Ni-20 wt. %Cr+ Al₂O₃ GE sample number 4-10-1

Figure 5.25 shows the SEM, AFM & UFM images of Ni-20Cr+ Al₂O₃ sample. SEM image is taken at the scan size of 8μm and at magnification of 10,000X. Al₂O₃ particles are clearly observed in the SEM images. This image is taken at 10° angle. In UFM image each and every grain is clearly seen. AFM-UFM image is taken at a scan size of 841nm and at a frequency of 370 KHz. Though these images are not tilted, the grains are clearly observed at nanoscale.

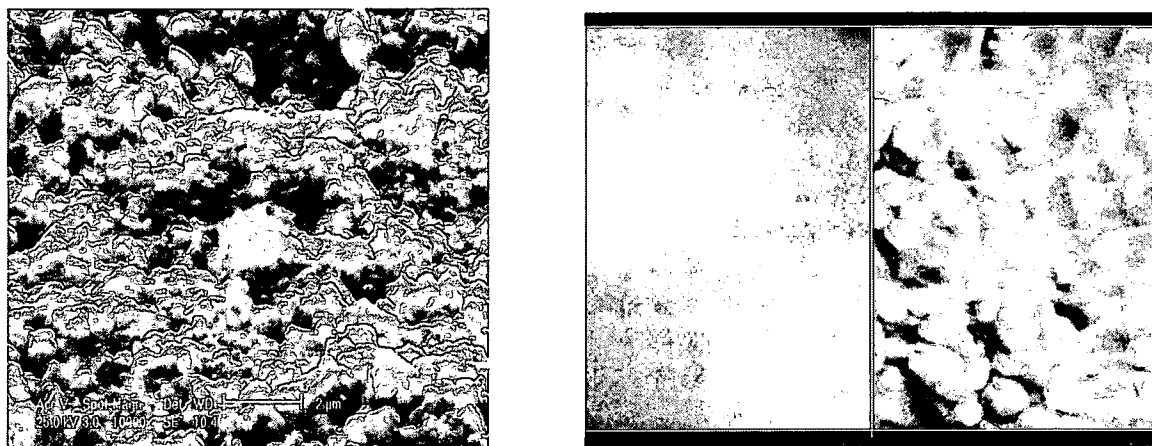


Figure 5.25: SEM and AFM-UFM images of Ni- 20wt.%Cr+Al₂O₃

Sample # 4 C1 Forged

Figure 5.26 shows SEM, AFM and UFM images. SEM image is taken at scan size of 4μm and at a magnification of 10,000X. In SEM image the slips observed in one grain taking place in one direction. The deformation in this material is taking through grains as there is uniformity in the surface topography. AFM-UFM images are taken at scan size of 1.70μm and at frequency of 460 KHz. In AFM-UFM images slips are observed in the direction of the crack growth and are uniform.

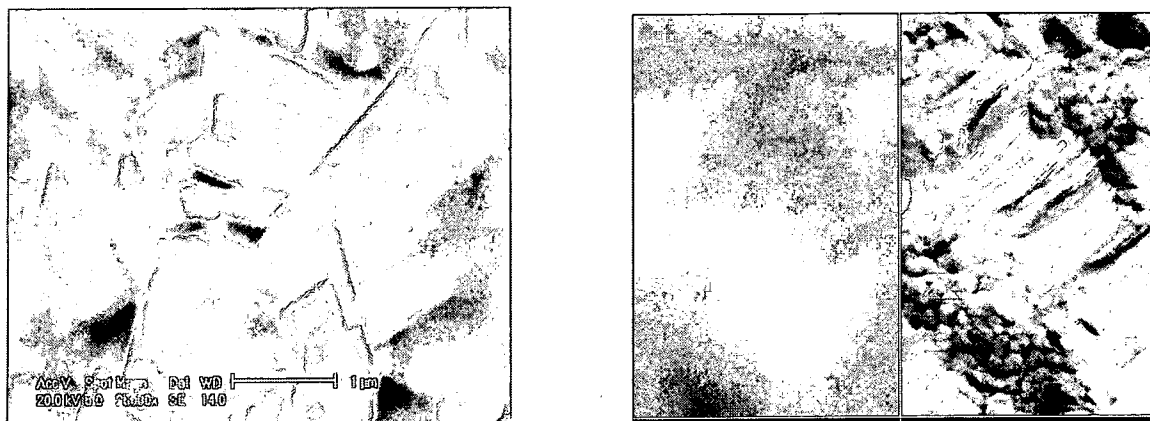


Figure 5.26: SEM and AFM-UFM images of C1 forged Ni- 20wt.%Cr

Sample # 5 MA754 HT

Figure 5.27 shows SEM, AFM & UFM images on MA754HT sample. SEM image is taken at the scan size of $8\mu\text{m}$ and at magnification of 10,000X. Slip bands are observed in SEM and AFM-UFM images. The contrast of SEM image is very low so the surface features are not clearly seen. In UFM images the slip bands and slips on the grains are clearly visible. AFM-UFM images are taken at scan size of $3.26\mu\text{m}$ and at frequency of 515 KHz. In AFM image also slips are observed. The surface features of these images are similar but the only difference is there contrast and the limitation on the magnification. thus, the study of fractography using AFM-UFM plays an important role in determining the deformation behavior of the material.

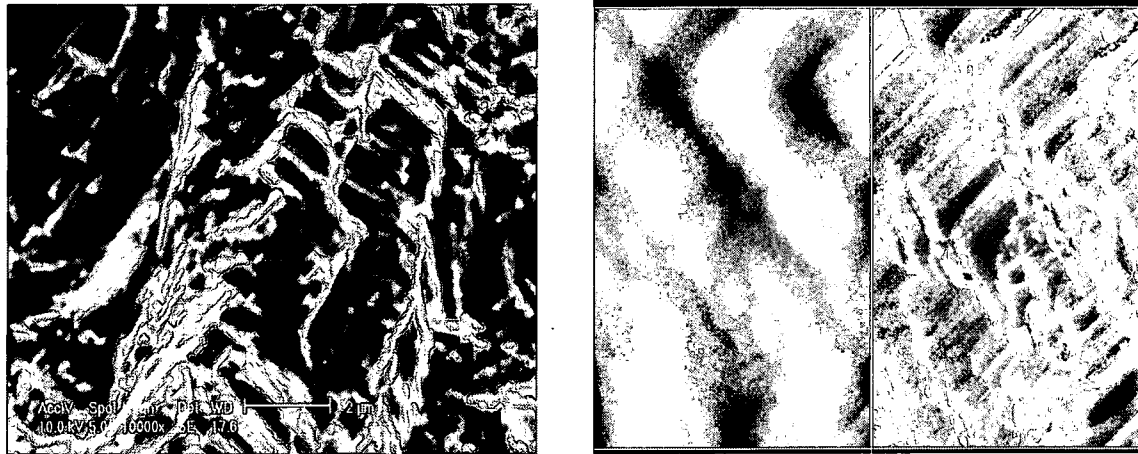


Figure 5.27: SEM and AFM-UFM images of MA754HT

5.5) Discussion

AFM-UFM and SEM analysis of fractured surfaces of Ni-20wt.%Cr with varying grain sizes can be used to obtain information about the deformation and crack growth behavior. High magnification SEM images show features of grains. In samples # 4 and 5, when the grain sizes are large. It also shows presence foreign particles, deformation slips. On the other hand in samples with grain sizes smaller than micron meters, it is difficult to observe grains clearly.

In AFM-UFM images of rough surfaces need a careful analysis. There are always possibilities of tip dominated artifacts. When features have sharper edges and have dimensions comparable to that of tip size. In UFM images, the edge contrast is further increased and one needs to be cautious in interpretation. Inspite of these difficulties, observations of images where the surface topography is in the range of μm , can provide useful information. In samples with larger grain size MA754 both slips as well as steps is observed. The slips have 200nm, where step heights are 10nm. In the case of sample #4 large grains ($>1\mu\text{m}$) slips can be observed. On the other hand in all samples where grain sizes are few hundred nm, no slips like features are evident. The grain features are quite

clear and appear to be intact. This indicates the crack growth occurs through grain boundaries.

It is well known from the Hall-Petch relationship that the yield strength is related to the grain size [24-25]. As the grain size is reduced crack is passing through the grain boundaries without disturbing the grains. At nanoscale, material consists of high volume fraction of grain boundaries as the grain size of material is very small. Thus the crack nucleation and growth can be facilitated at the grain boundaries, which are the regions of stress concentration as it consists of high density of grains. And as the fracture energy is more than the grain size, the crack propagates through the grain boundaries which are the easiest paths. Thus in these samples we observe intercrystalline fracture.

Thus the following features are concluded from the observations. In sample # 1 and sample # 2 whose grain size is at nanometer scale, the slip deformation is not observed. In sample #3 crack propagates through the grains and it performs the slip deformation. Initially when the crack growth rate values are high the slip deformation in the grains are observed, as crack growth rate decreases the slips are not observed which is also similarly in the case of sample # 4 which is a C1 forged specimen deformation takes place through the grains and slips are clearly observed in a grain. Sample # 5 which is MA754HT, each and every grain participates in the slip deformation. The average grain size of this material is $2\mu\text{m}$ which is much higher than other samples. The most interesting observation that is noticed in this study is that when the material consists of smaller grain size the deformation is taking place through the grain boundaries whereas when the materials whose grain size is large, than the slip deformations are observed. Other point of interest is that, in materials such as sample # 3, 4, 5 whose grain sizes are from

nanometer scale to microns, the slip deformation is observed at higher crack growth rate and as crack growth rate decreases deformation is observed as the striations that is there is no slip deformation.

CHAPTER 6

CONCLUSIONS

A white light interference microscope has been used to measure the topography of the fatigue fracture surfaces in Ni-20wt %Cr samples along the direction of loading and the crack growth. The surface roughness was measured as a function of distance from the precrack region through the post fatigue region on five Ni-20wt %Cr samples. The distance on the sample was along the length of the grown crack. Thus, the surface roughness was related directly to the crack length and the crack growth rate in this experiment. Hence, a relation between the surface roughness and crack growth rate was established on all the samples. It was observed that for samples #1, 2, 3 and 4, whose grain size was in the range of 100nm-1.2 μ m, the surface roughness of these samples gradually decreased with respect to the crack growth rate; whereas in the sample # 5, which is MA754HT, the surface roughness did not vary proportionally with crack growth rate. The behavior of sample #5 was due the large grain size of the sample, which was in the range of 2 μ m. Thus, the surface roughness of samples with smaller grain size decreased gradually with respect to crack growth rate; whereas in the sample with the largest grain size, roughness did not vary proportionally with respect to crack growth rate.

A combination of AFM-UFM has been used for the microstructural analysis of fracture surfaces of Ni-20wt %Cr samples. The following features are concluded from the

observations. In sample # 1 and sample # 2, whose grain size is at a nanometer scale, the slip deformation was not observed. In sample #3, the crack propagated through the grains, and it exhibited slip deformation. Initially, when the crack growth rate values were high, the slip deformation in the grains was observed; as crack growth rate decreased, the slips were not observed. This was also the case for sample # 4, which was a multi-axis forged specimen, in which deformation took place through the grains and, slips were clearly observed in the grains. Sample # 5, which was MA754HT, each and every grain participated in the slip deformation. The average grain size of this material is $2\mu\text{m}$, which is much higher than other samples. The most interesting observation that was noticed in this study, was that when the material consisted of smaller grain size, the deformation took place through the grain boundaries, whereas in the materials with large grain size, slip deformations were observed.

Hence, high resolution microscopes - such the white light interference microscope, the atomic force microscope, and the ultrasonic force microscope - were effective tools for characterizing the fatigue fracture surface of Ni-20wt %Cr samples with various grain sizes.

REFERENCES

- 1) Y.Murakami, T.Nomoto, T.Ueda and Y.Murkami "On the mechanism of fatigue failure in the superlong life regime ($N > 10^7$ cycles). Part II: a fractrographic investigation." Fatigue fracture engineering material structure, vol 23, pp 903-910, 2000.
- 2) M.H Swain, "Mointoring small crack growth by replica method", small-crack test methods, ASTM STP 1149, American society for testing and materials, 1992, pp 34-56.
- 3) J.M Larsen, J.R Jira and K.S Ravi chandran, "Measurement of small crack by photomicroscopy: Experiments and analysis", small-crack test methods, ASTM STP 1149, American society for testing and materials, 1992, pp 57-80.
- 4) W.N Sharpe, J.R Jira, J.M Larsen, " Real -time measurement of small crack opening behavior using an interferometric strain/ displacement gage", ASTM STP 1149, American society for testing and materials, 1992, pp 92-115.
- 5) R.P Gang loff, D.C Slavik, R.S. Piascik, R.H Vanstone, " Direct current electrical potential measurement of the growth of small cracks", ASTM STP 1149, American society for testing and materials, 1992, pp 116-168.
- 6) S.A.C Gould, B. Darke, C.B prater etal, " Atomic force microscope : A tool for science and industry", Ultramicroscopy, Vol 33, 1990, pp 93-98.

- 7) Metrics-2000 “ Atomic force microscope”, operating manual (Reve), Bureleigh instruments, Inc Burleigh park, Fishers, NY 14453-0755, 1997.
- 8) S.Suresh “Fatigue of materials”, second edition, Cambridge university press, 1998.
- 9) Marc Taub, Brian Menzel, Gaurav Khanna and Erica Lilleodden_“ SPM training manual version 2.0” laboratory for advanced materials ,Stanford University, july 2003.
- 10) Digital Instruments, Inc. Santa Barbara, CA. “Dimensions™ 3000 Scanning Probe Microscope, Instruction Manual,”1986.
- 11) Bushan,B. Handbook of Nano technology, Springer-Verlag, New York,2004.
- 12) Sriram Sundararajan, Bharat Bhushan “Development of AFM-based techniques to measure mechanical properties of nanoscale structures,” Sensors and Actuators A,Vol 101,pp338-351,2002.
- 13) N.A. Burnham, G.Gremaud, A.J. Kulik, P.J. Gallo and F. Oulevey, “Scanning local – acceleration microscopy”, J.Vac.Sci. Technol. B14(2), 1308-1312(1996).
- 14) U.Rabe and W.Arnold “Acoustic microscopy by atomic force microscopy,” Applied physics letter, Vol 64, 1994.
- 15) S.Lippold and J.Podlensny, surface profiler : Technical reference manual, WKYO corporation, Tuscon AZ, 1996.
- 16) J.R.Davis “ASM specialty handbook Nickel, Cobalt and their alloys” ASM international handbook committee, 2000.
- 17) R.Rodriguez, R.W.Hayes, P.B.Berbon, E.J.Lavernia “Tensile and creep behavior of cryomilled Inco 625” Acta materialia, vol 51, pp 911-929, 2003.

- 18) B.Huang, R.J.Perez, E.J.Laveria "Grain growth of nanocrystalline Fe-Al alloys produced by cryomilling in liquid argon and nitrogen" *Material science and engineering A*, vol 225, pp 124-132, 1998.
- 19) M.J.Luton, C.S.Jayanth, M.M.Disko, S.Matras, J.Vallone "Multi compositional ultrafine microstructure in L.E. MC Candish, D.E.Polk, R.W.Siegel, B.H.Kear (Eds)" *Material research society symposium proceedings*, Pittsburgh, pp 79,1989.
- 20) J.Lee, F.Zhou, K.H. Chung, N.J.kim and E.J. Lavernia "Grain growth of nanocrystalline Ni powders prepared by cryomilling" *Metallurgical and materials transactions A*, Vol 32, pp 3109, Dec 2001.
- 21) Terry C., Totemeier and Thomas M. Lillo "Effect of orientation on the tensile and creep properties of coarse grained Inconel MA754" *Metallurgical and materials transactions A*, vol 36A, PP 785, March 2005.
- 22) M.A. Miodownik, A.J.Wilkinson and J.W.Martin "On the secondary recrystallization of MA754" *Acta materialia*, vol 46 no.8, pp 2809-2821, 1998.
- 23) Pascal Daguiet, Stephane Henaux, Elisabeth Bouchaud, Francois Creuzet "Quantitative analysis of fracture surface by atomic force microscopy" *surface du verre et interfaces*, Vol 39, 1995.
- 24) T.Hanlon, E.D. Tabachnikova, S.Suresh "Fatigue behavior of nanocrystalline metals and alloys", *International journal of fatigue*, Vol 27, pp 1147-1158, 2005.
- 25) Y.Oda, Y.Furuya, H. Noguchi and K. Higashida "AFM and SEM observation on mechanism of fatigue crack growth in an Fe-Si single crystal", *International journal of fracture*, Vol 113, pp 213-231, 2002.

R002588671

The HF Group

Indiana Plant

T 052545 F 1 00



6/8/2006